

AD-A093 794

SYSTEMS SCIENCE AND SOFTWARE LA JOLLA CA  
ANALYSIS OF THE LOW FREQUENCY GROUND MOTION ENVIRONMENT FOR MX,--ETC(U)  
JAN 80 J R MURPHY, T J BENNETT

DNA001-79-C-0114

NL

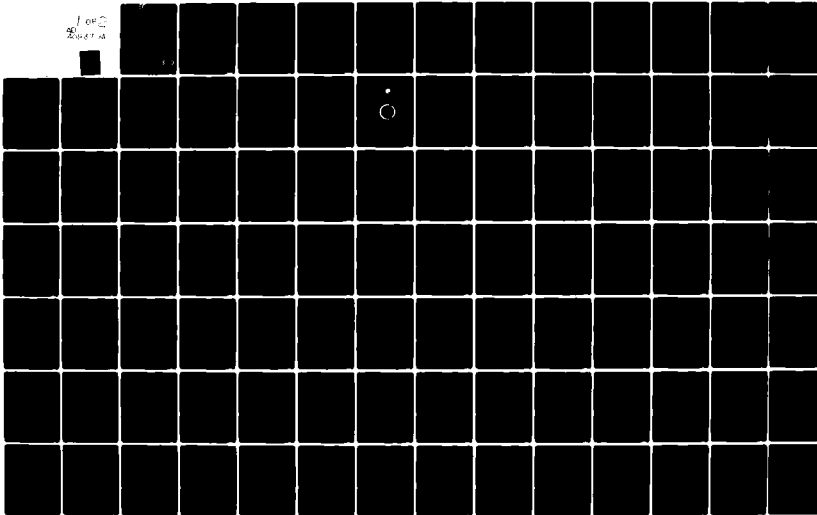
UNCLASSIFIED

SSS-R-80-4298

DNA-5219F

F/6 8/11

100  
200



AD A093794

LEVEL II

12  
DNA 5219F

# ANALYSIS OF THE LOW FREQUENCY GROUND MOTION ENVIRONMENT FOR MX

## Surface Waves and Valley Reverberation

J.R. Murphy  
T.J. Bennett  
Systems, Science and Software  
P.O. Box 1620  
La Jolla, California 92038

2 January 1980

Final Report for Period 5 December 1978–31 December 1979

CONTRACT No. DNA 001-79-C-0114

APPROVED FOR PUBLIC RELEASE;  
DISTRIBUTION UNLIMITED.

THIS WORK SPONSORED BY THE DEFENSE NUCLEAR AGENCY  
UNDER RDT&E RMSS CODE B344079464 Y99QAXSB27701 H2590D.

DDC FILE COPY

Prepared for  
Director  
DEFENSE NUCLEAR AGENCY  
Washington, D. C. 20305

DTIC  
ELECTED  
JAN 13 1981  
S C D

Destroy this report when it is no longer  
needed. Do not return to sender.

PLEASE NOTIFY THE DEFENSE NUCLEAR AGENCY,  
ATTN: STI, WASHINGTON, D.C. 20305, IF  
YOUR ADDRESS IS INCORRECT, IF YOU WISH TO  
BE DELETED FROM THE DISTRIBUTION LIST, OR  
IF THE ADDRESSEE IS NO LONGER EMPLOYED BY  
YOUR ORGANIZATION.



## UNCLASSIFIED

SECURITY CLASSIFICATION OF THIS PAGE (When Data Entered)

19. REPORT DOCUMENTATION PAGE		READ INSTRUCTIONS BEFORE COMPLETING FORM
1. REPORT NUMBER DNA 5219F	2. GOVT ACCESSION NO. AD-A093794	3. RECIPIENT'S CATALOG NUMBER
4. TITLE (and Subtitle) ANALYSIS OF THE LOW FREQUENCY GROUND MOTION ENVIRONMENT FOR MX, Surface Waves and Valley Reverberation.		5. TYPE OF REPORT & PERIOD COVERED Final Report for Period 5 Dec 78—31 Dec 79
7. AUTHOR(s) J. R. Murphy T. J. Bennett		6. PERFORMING ORG. REPORT NUMBER SSS-R-80-4298
8. CONTRACT OR GRANT NUMBER(s) DNA 001-79-C-0114		9. PERFORMING ORGANIZATION NAME AND ADDRESS Systems, Science and Software P.O. Box 1620 La Jolla, California 92038
11. CONTROLLING OFFICE NAME AND ADDRESS Director Defense Nuclear Agency Washington, D.C. 20305		10. PROGRAM ELEMENT, PROJECT, TASK AREA & WORK UNIT NUMBERS Subtask Y99QAXSB277-01
14. MONITORING AGENCY NAME & ADDRESS (if different from Controlling Office)		12. REPORT DATE 2 Jan 1980
		13. NUMBER OF PAGES 146
16. DISTRIBUTION STATEMENT (of this Report)  Approved for public release; distribution unlimited.		15. SECURITY CLASS (of this report) UNCLASSIFIED
17. DISTRIBUTION STATEMENT (of the abstract entered in Block 20, if different from Report)		
18. SUPPLEMENTARY NOTES  This work sponsored by the Defense Nuclear Agency under RDT&E RMSS Code B344079464 Y99QAXSB27701 H2590D.		
19. KEY WORDS (Continue on reverse side if necessary and identify by block number)  MX Multiple Source Ground Motion Rayleigh Waves Seismic Multipathing Explosion Beam-Steering		
20. ABSTRACT (Continue on reverse side if necessary and identify by block number)  This report summarizes the results of investigations into the effects on explosion-generated ground motion of the MX system siting environment in alluvial valleys. The objective of the analyses described in the report has been to develop a better, quantitative understanding of the late-time, low-frequency ground motion expected in such environments in order to provide a firmer basis for scaling to untested geologic environments and attack conditions. The studies		

## UNCLASSIFIED

SECURITY CLASSIFICATION OF THIS PAGE (When Data Entered)

## 20. ABSTRACT (Continued)

reported have focused on two aspects of the problem of low-frequency surface waves which dominate the ground motion generated by blasts in MX valleys: (1) definition of site and yield dependence of ground motion characteristics at alluvial valley sites, and (2) possible enhancement of ground motion at sites in alluvial valleys due to surface-wave reverberation.

With regard to the first aspect, we have relied primarily on the theory of surface-wave generation by air-blast loading on an alluvial valley to determine scaling relations as a function of both explosion yield and site geology. The amplitude of the Rayleigh wave source function has been found to be directly proportional to yield at low frequencies and independent of site geology; while, at high frequencies, it behaves as yield to the one-third power and increases with near-surface shear wave velocity. These relations have been applied to several specific prototype MX sites; and it has been found that predominant Rayleigh wave frequencies at the sites depend only on thickness and shear velocity of the surficial soil layer and are independent of yield for yields greater than a few hundred kilotons. An anomalous arrival observed in the Misers Bluff II-2 experiment (the "800 millisecond anomaly") has been found to be inconsistent with simple linear superposition of single burst ground motions and may correspond to a true multiburst effect. The anomalous ground motion has been shown to match a theoretical model which considers Rayleigh waves converging on the center of the source array from an axisymmetric, impulsive surface source, acting at a radius-coincident with that of the charge locations.

In the valley reverberation element of the study, emphasis has been on analysis of observational data, primarily the ground motions recorded during the Misers Bluff II experiment at Planet Ranch in Arizona in 1978. Observations from Misers Bluff II were found to be consistent with previous experimental results as well as theoretical calculations which indicate that late-time, low-frequency ground motion in alluvial valley environments are modified by the presence of valley boundaries. In particular, it has been found that duration of ground motion in such environments may be significantly prolonged. Differences between the late time ground motions for the MBII-1 and MBII-2 tests suggest that surface-wave reverberation has a complex dependence on source and receiver locations within the valley structure.

Accession For	
NTIS CRA&I	<input checked="" type="checkbox"/>
DTIC TAB	<input type="checkbox"/>
Unannounced	<input type="checkbox"/>
Justification	
By _____	
Distribution/ _____	
Availability Codes _____	
Avail and/or _____	
Dist	Special
A	

UNCLASSIFIED

TABLE OF CONTENTS

<u>Section</u>	<u>Page</u>
LIST OF ILLUSTRATIONS .....	2
I. INTRODUCTION.....	9
II. RAYLEIGH WAVES FROM NEAR-SURFACE EXPLOSIONS.....	11
2.1 INTRODUCTION.....	11
2.2 DESCRIPTION OF THE MODEL.....	13
2.3 SCALING LAWS FOR RAYLEIGH WAVES.....	20
2.3.1 Source Scaling.....	21
2.3.2 Site Scaling.....	28
2.3.3 Rayleigh Wave Scaling Relations.....	32
2.4 RAYLEIGH WAVE GROUND MOTION ESTIMATES FOR SOME PROTOTYPE MX SITES.....	34
2.5 MULTIBURST SURFACE WAVE EFFECTS ON MISERS BLUFF II-2.....	58
III. VALLEY REVERBERATION.....	67
3.1 INTRODUCTION.....	67
3.2 RESULTS FROM PREVIOUS STUDIES.....	70
3.3 MISERS BLUFF II REVERBERATION STUDIES.....	98
3.3.1 Data Analysis.....	98
3.3.2 Discussion of Results.....	132
IV. SUMMARY AND CONCLUSIONS.....	135
4.1 SUMMARY.....	135
4.2 CONCLUSIONS.....	136
REFERENCES.....	139

LIST OF ILLUSTRATIONS

<u>Figure</u>		<u>Page</u>
1	Comparison of observed and calculated Rayleigh wave motion, Pre-Mine Throw, vertical component, $r = 355$ m.....	12
2	Multilayered elastic halfspace loaded by an axisymmetric surface overpressure.....	14
3	Comparison of diverging and converging Rayleigh wave geometry for axisymmetric loads acting on the surface of a multilayered halfspace.....	16
4	Path of integration for determination of Rayleigh wave contributions produced by axisymmetric surface loads.....	18
5	Schematic diagram illustrating the yield dependence of the Rayleigh wave source function at a fixed site.....	26
6	Schematic diagram illustrating the site dependence of the Rayleigh wave source function at a fixed yield.....	27
7	Geologic model for the parametric study of the Rayleigh wave site response function.....	29
8	Variation of $A_R$ spectral response as a function of $H$ for a fixed value of $\beta_1$ .....	30
9	Variation of $A_R$ spectral response as a function of $\beta_1$ for a fixed value of $H$ .....	31
10	Schematic representation of the $A_R$ spectral response at two hypothetical sites.....	33
11	Schematic diagram illustrating the Rayleigh wave yield scaling relations for site $A_R^{(2)}$ .....	35
12	Schematic diagram illustrating the Rayleigh wave yield scaling relations for site $A_R^{(1)}$ .....	36
13	Subsurface geologic profiles for MX prototype cases 1 through 3.....	38
14	Subsurface geologic profiles for MX prototype cases 4 and 5.....	39
15	Fundamental mode Rayleigh wave site response functions for cases 1 and 2.....	41
16	Fundamental mode Rayleigh wave site response functions for cases 3 and 4.....	42

LIST OF ILLUSTRATIONS (CONT'D)

<u>Figure</u>	<u>Page</u>
17      Fundamental mode Rayleigh wave site response function for case 5.....	43
18      Comparison of analytical Rayleigh wave and finite difference displacement time histories, case 1, vertical component, $W = 1 \text{ Mt}$ , $R = 1800 \text{ m}$ .....	47
19      Comparison of analytical Rayleigh wave and finite difference displacement time histories, case 1, radial component, $W = 1 \text{ Mt}$ , $R = 1800 \text{ m}$ .....	48
20      Comparison of analytical Rayleigh wave and finite difference displacement time histories, case 2, vertical component, $W = 1 \text{ Mt}$ , $R = 1800 \text{ m}$ .....	49
21      Comparison of analytical Rayleigh wave and finite difference displacement time histories, case 2, radial component, $W = 1 \text{ Mt}$ , $R = 1800 \text{ m}$ .....	50
22      Comparison of analytical Rayleigh wave and finite difference displacement time histories, case 3, vertical component, $W = 1 \text{ Mt}$ , $R = 1800 \text{ m}$ .....	51
23      Comparison of analytical Rayleigh wave and finite difference displacement time histories, case 3, radial component, $W = 1 \text{ Mt}$ , $R = 1800 \text{ m}$ .....	52
24      Comparison of analytical Rayleigh wave and finite difference displacement time histories, case 4, vertical component, $W = 1 \text{ Mt}$ , $R = 1800 \text{ m}$ .....	53
25      Comparison of analytical Rayleigh wave and finite difference displacement time histories, case 4, radial component, $W = 1 \text{ Mt}$ , $R = 1800 \text{ m}$ .....	54
26      Analytical Rayleigh wave displacement time histories, case 5, $W = 1 \text{ Mt}$ , $R = 1800 \text{ m}$ .....	55
27      Comparison of vertical component Rayleigh wave displacement time histories for yields of 1 and 30 Mt, case 2, $R = 1800 \text{ m}$ .....	57
28      Source/receiver pattern and subsurface geologic profile for the Misers Bluff II-2 experiment....	59
29      Observed vertical displacement inside source array, MBII-2.....	61
30      Comparison of observed MBII-2 vertical displacement data with theoretical converging Rayleigh wave solution; distance measured from center of source array ( $t_0 = 0$ , $r_1 = 50 \text{ m}$ , $r_2 = 150 \text{ m}$ )....	63

LIST OF ILLUSTRATIONS (CONT'D)

<u>Figure</u>		<u>Page</u>
31	Comparison of observed MBII-2 vertical displacement data with theoretical converging Rayleigh wave solution; distance measured from center of source array ( $t_0 = 0.4$ seconds, $r_1 = 75$ m, $r_2 = 125$ m).....	64
32	Comparison of observed MBII-2 vertical displacement data with theoretical converging Rayleigh wave solution; distance measured from center of source array ( $t_0 = 0.4$ seconds, $r_1 = 90$ m, $r_2 = 110$ m).....	65
33	Schematic geologic cross section for a Basin and Range valley structure.....	68
34	Comparison of seismograms recorded at about the same epicentral distance inside (SE-6) and outside (PAH) the Las Vegas Valley.....	69
35	Station location map for Las Vegas.....	72
36	Radial component record section for the Carpetbag event.....	73
37	Beam steer analysis of the Carpetbag Rayleigh waves recorded in Las Vegas.....	76
38	Las Vegas valley map showing approximate travel paths of secondary surface wave arrivals in Las Vegas.....	77
39	Calabash station location map.....	79
40	Vertical geologic section for the Calabash event	80
41	Comparison of ground motion records recorded at about the same distance inside (752) and outside (755) Yucca Valley, Calabash event.....	81
42	Block diagram of the bandpass filter envelope circuit.....	83
43	Comparison of the one Hertz envelope for stations inside (752) and outside (755) Yucca Valley.....	84
44	Comparison of the one Hertz envelope for stations inside (746) and outside (756) Yucca Valley.....	85
45	Geometry and loading conditions for elliptical valley approximation.....	87

LIST OF ILLUSTRATIONS (CONT'D)

<u>Figure</u>		<u>Page</u>
46	Computed horizontal particle velocity seismograms as a function of distance from the valley center.	88
47	Comparison of particle velocity profiles across the valley at selected times.....	89
48	Plane layered approximation to a Basin and Range valley structure.....	91
49	Comparison of free surface horizontal velocity computed without (top) and with (bottom) a valley boundary, $r = 0.9$ km.....	92
50	Comparison of free surface vertical velocity computed without (top) and with (bottom) a valley boundary, $r = 0.9$ km.....	93
51	Comparison of free surface horizontal velocity computed without (top) and with (bottom) a valley boundary, $r = 2.03$ km.....	94
52	Comparison of free surface vertical velocity computed without (top) and with (bottom) a valley boundary, $r = 2.03$ km.....	95
53	Comparison of free surface horizontal velocity computed without (top) and with (bottom) a valley boundary, $r = 2.96$ km.....	96
54	Comparison of free surface vertical velocity computed without (top) and with (bottom) a valley boundary, $r = 2.96$ km.....	97
55	Bedrock contour map for Misers Bluff II site with locations for individual explosions (+) and recording stations (●) for the MBII-1 single burst event and (○) for the MBII-2 multiple burst event. Contour lines give bedrock elevations in feet; local average surface elevation is 670 feet.....	99
56	Comparison of ground motion time histories recorded at comparable ranges from the 100 ton HE events, Misers Bluff II-1 (MBII-1) and Pre-Mine Throw IV (PMT IV).....	101
57	Comparison of eighth order bandpass filtered displacements at 4.0 and 2.0 Hz; MBII-1, $R = 305$ m..	103
58	Fundamental mode Rayleigh wave site response functions for Misers Bluff II site.....	104

LIST OF ILLUSTRATIONS (CONT'D)

<u>Figure</u>	<u>Page</u>
59 Schematic describing the behavior of a linear, uniformly-spaced array receiving plane seismic wave signals.....	105
60 Response of the MBII-1 array to 4 Hz signals with phase velocity $c = 600$ m/sec. Solid line shows theoretical response to harmonic waves arriving from $\theta = 0^\circ$ . Circles indicate observed response of the filter, beam-steering process with observations normalized to the maximum predicted response.....	110
61 MBII-1 filtered beam $c = 600$ m/sec, $f_c = 4.0$ Hz.....	111
62 MBII-1 filtered beam, $c = 600$ m/sec, $f_c = 4.0$ Hz.....	112
63 Response of the MBII-1 array to 4 Hz signals with phase velocity $c = 600$ m/sec. Solid line shows theoretical response to harmonic waves arriving from $\theta = 30^\circ$ . Circles indicate observed response to the filter, beam-steering process with observations normalized to the maximum predicted response.....	113
64 Ground motion hodograph for a frequency of 4 Hz during the 1-second time window surrounding the peak displacement; MBII-1, $R = 280$ m. Motion in R-Z plane, at top, and in R-T plane, at bottom, for different orientations, $\theta_0$ , of the R-Z plane.....	115
65 Comparison of theoretical and observed displacements; MBII-1, $R = 300$ m.....	117
66 MBII-1 filtered beam, $c = 1000$ m/sec, $f_c = 2.0$ Hz.....	118
67 Comparison of eighth-order band-pass filtered radial displacements at center frequencies, $f_c$ , of 1.0, 2.0, 2.5, 3.0, 4.0 and 5.0 Hz; MBII-2, $R = 420$ m.....	120
68 Comparison of eighth-order band-pass filtered tangential displacements at center frequencies, $f_c$ , of 1.0, 2.0, 2.5, 3.0, 4.0 and 5.0 Hz; MBII-2, $R = 420$ m.....	121

LIST OF ILLUSTRATIONS (CONT'D)

<u>Figure</u>	<u>Page</u>
69 Comparison of eighth-order band-pass filtered vertical displacements at center frequencies, $f_c$ , of 1.0, 2.0, 2.5, 3.0, 4.0 and 5.0 Hz; MBII-2, $R = 420$ m.....	122
70 MBII-2 filtered beam, $c = 600$ m/sec, $f_c = 4$ Hz...	123
71 MBII-2 filtered beam, $c = 600$ m/sec, $f_c = 4$ Hz...	124
72 Response of the MBII-2 array to 4 Hz signals with phase velocity $c = 600$ m/sec. Solid line shows theoretical response to harmonic waves arriving from $\theta = 0^\circ$ . Circles indicate observed response to the filter, beam-steered process with observations normalized to the maximum predicted response.....	126
73 MBII-2 filtered beam, $c = 600$ m/sec, $f_c = 2$ Hz...	127
74 MBII-2 filtered beam, $c = 1000$ m/sec, $f_c = 2$ Hz..	128
75 Comparison of eighth-order band-pass filtered radial displacements at center frequencies, $f_c$ , of 1.0, 2.0, 2.5, 3.0, 4.0 and 5.0 Hz; MBII-2, $R = 650$ m.....	130
76 Comparison of eighth-order band-pass filtered vertical displacements at center frequencies, $f_c$ , of 1.0, 2.0, 2.5, 3.0, 4.0 and 5.0 Hz; MBII-2, $R = 650$ m.....	131

## I. INTRODUCTION

Both experimental and theoretical studies that have been conducted during the past several years have confirmed that the potential ground motion environment for the MX system may be considerably different than that for which previous strategic systems have been designed. In particular, the Multiple Protective Structure concept together with the site requirements have combined to increase the relative importance of the late-time, longer-period ground motions associated with elastic, surface wave propagation at the site. That is, the system will be sited in a valley and, under a multiple attack scenario, untargeted points can be expected to experience a significant ground motion environment as the result of the combination of effects originating from attacks on surrounding aimpoints. Furthermore, reflections of outgoing energy from the valley boundaries can be expected to complicate the ground motion environment within the valley, particularly at late times.

The objective of the analyses described in this report has been to develop a better, quantitative understanding of these late-time, long-period ground motions in order to provide a firmer basis for scaling to untested geologic environments and attack conditions. Two specific problem areas have been addressed during the past year. The first concerns the definition of the site and yield dependence of the characteristics of the low-frequency ground motion at a variety of prototype MX sites. Progress in this study area is summarized in Section II which includes a detailed discussion of scaling relations for airblast-induced Rayleigh waves with applications to five specific sites of potential interest, as well as preliminary analysis of a new, multiburst surface wave phenomenon observed on the Misers Bluff II-2 experiment.

The second problem area treated in this report concerns an assessment of the possibility that the MX ground motion environment may be significantly altered, and in particular enhanced, as a result of siting the system in a valley. During the past several years a number of specific experimental and theoretical investigations have been conducted in an attempt to define the effects of valley boundaries on the ground motion environment to be expected at target points inside the valley. A brief summary of the results of these earlier studies is presented in Section III together with a detailed analysis of the valley reverberation data recorded from the Misers Bluff II experiments. This is followed in Section IV by a summary, together with a statement of conclusions summarizing our current state of knowledge with regard to these issues.

## II. RAYLEIGH WAVES FROM NEAR-SURFACE EXPLOSIONS

### 2.1 INTRODUCTION

As a result of research conducted during the past several years, much progress has been made in defining the characteristics of the ground roll component of the motion produced by near-surface explosions. In particular, it has been demonstrated (Murphy, 1978; Auld and Murphy, 1979) that these low-frequency arrivals are predominantly elastic Rayleigh waves driven by the airblast loading acting on the surface outside the region of strong nonlinear interaction (i.e., the crater). Moreover, it has been shown that these Rayleigh waves can be a very significant component of the ground motion, particularly at ranges where the peak airblast overpressure is less than a few hundred psi (pounds per square inch). For example, Figure 1 shows a comparison between the vertical particle velocity waveform measured at a range of 355 m from the Pre-Mine Throw 100 ton surface HE experiment and the theoretically predicted Rayleigh wave motion (Murphy, 1978). It can be seen that the surface wave component dominates the motion at this range and, furthermore, that it can be simulated with remarkably good accuracy using the selected theoretical model. A similar capability has also been demonstrated for the HE explosions at other sites (e.g., Pre-Dice Throw, Murphy, 1978; Misers Bluff II, Murphy and Bennett, 1979) indicating that the dependence of the surface wave characteristics on site geology can be accounted for within the framework of a quantitative model.

The significance of these findings with regard to the present investigation lies in the fact that the theory governing the generation and propagation of elastic Rayleigh waves is well developed and thus can be used to help define scaling laws for the low-frequency components of the ground

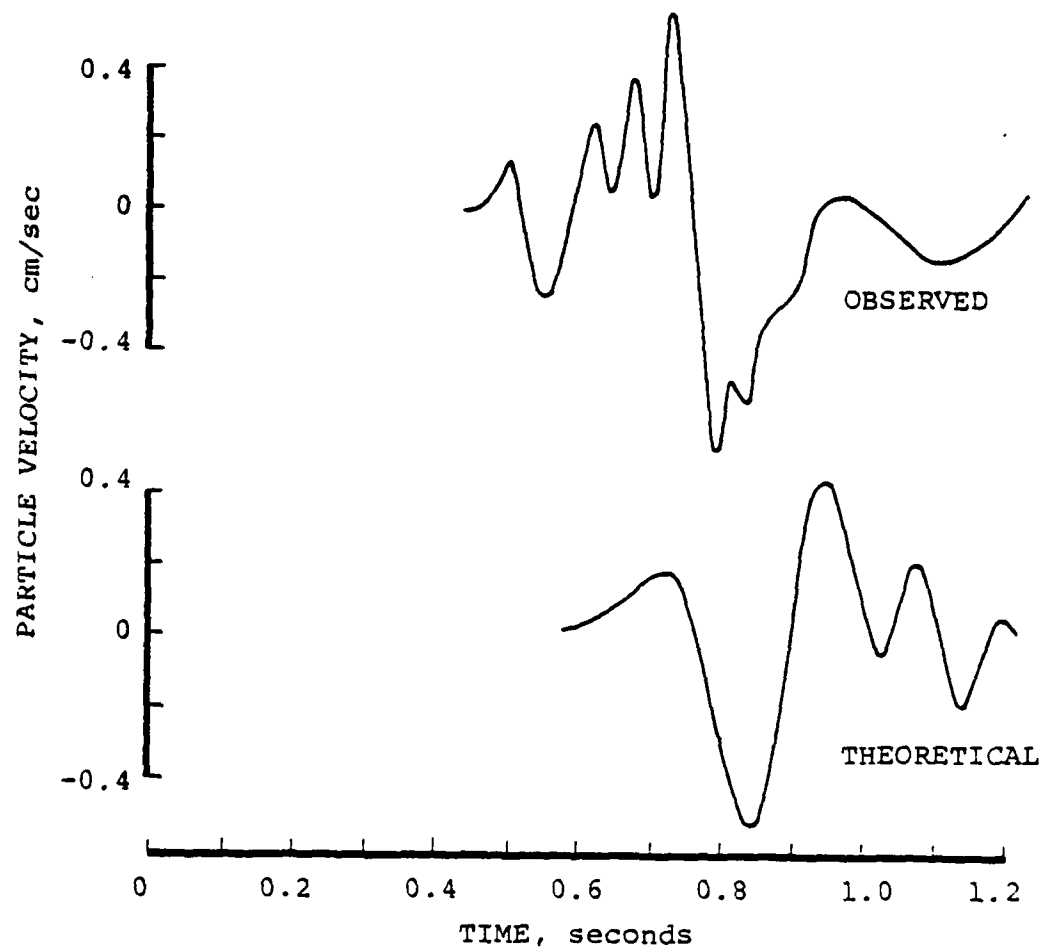


Figure 1. Comparison of observed and calculated Rayleigh wave motion, Pre-Mine Throw, vertical component,  $r = 355$  m.

motion environment. In particular, the results of studies conducted to date suggest that it should be possible to estimate the dominant frequency and relative duration and amplitude level of the low-frequency ground motion to be expected at different MX prototype sites as a function of site geology and explosion yield. In the following sections, the theoretical basis for the surface wave model will be reviewed and applied to a preliminary assessment of some of the problems associated with the definition of the low-frequency ground motion environment for the MX system.

## 2.2 DESCRIPTION OF THE MODEL

The problem of interest here concerns the elastic response of a multilayered halfspace to a propagating, axi-symmetric normal load acting on the surface (i.e., an approximation to an airblast). The geometry of the problem is illustrated in Figure 2 which shows a sequence of constant thickness ( $d_i$ ) layers overlying a semi-infinite halfspace being acted on by a surface source centered on the origin. As a first approximation, the layers are taken to be perfectly elastic and are characterized by their Lamé constants ( $\lambda, \mu$ ) and density ( $\rho$ ). The complete analytic solution to this boundary value problem, representing the total response of the multilayered halfspace, is very complicated and not yet fully developed. However, the surface wave portion of the solution is simple enough that the exact result can be written down in compact form using the matrix formulation of the problem pioneered by Haskell (1953) and Harkrider (1964). In fact, for the airblast loading condition being considered here, it can be shown (Harkrider, et al., 1974; Bache, et al., 1977) that the vertical (W) and radial (U) components of the Rayleigh wave contribution to the motion at horizontal range  $r$  outside the source region can be written in the form:

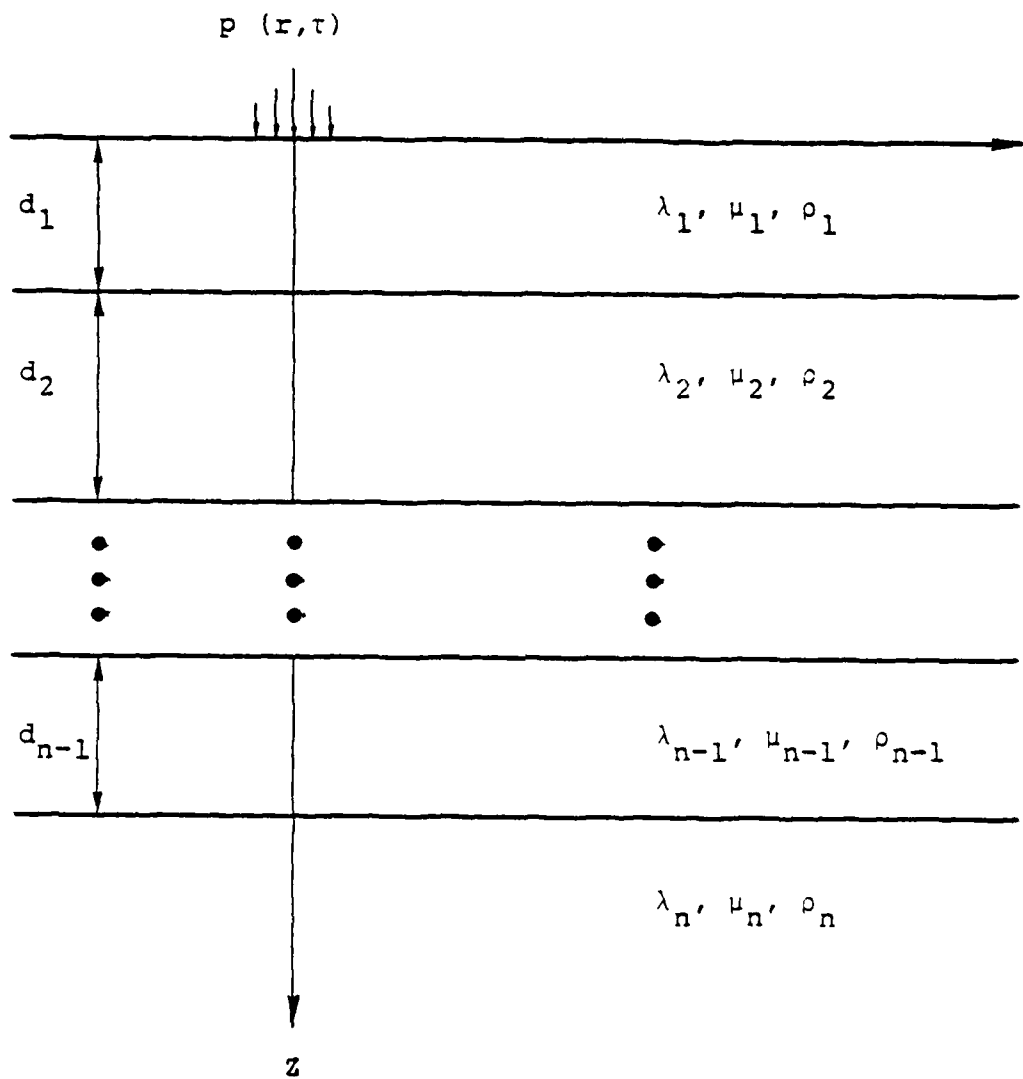


Figure 2. Multilayered elastic halfspace loaded by an axisymmetric surface overpressure.

$$W_j(\omega, r) = -i\pi A_{Rj}(\omega) H_0^{(2)}(k_j r) S_j(\omega)$$

$$U_j(\omega, r) = \epsilon_j(\omega) \frac{H_1^{(2)}(k_j r)}{H_0^{(2)}(k_j r)} W_j(\omega, r) \quad (2-1)$$

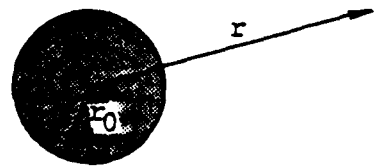
where subscript  $j$  denotes the mode number,  $A_{Rj}(\omega)$  is the Rayleigh wave site response function,  $H_i^{(2)}(k_j r)$  is the Hankel function propagation term for wavenumber  $k$ , ( $i = 0, 1$ ),  $\epsilon_j(\omega)$  is the ellipticity function and  $S_j(\omega)$  is the Rayleigh wave source function given by:

$$S_j(\omega) = \int_{r_1}^{r_2} p(r', \omega) J_0(k_j r') r' dr' \quad (2-2)$$

where  $p(r, \omega)$  is the Fourier transform of the airblast load acting over a surface disk extending from  $r_1$  to  $r_2$  ( $0 \leq r_1 \leq r_2 \leq r$ ) and  $J_0(k_j r)$  is the Bessel function kernel.

Equations (2-1) and (2-2) define the solution for the Fourier transform of the displacement at distance  $r$  due to Rayleigh waves diverging from a central source region, and thus represents the complete solution for far-field observation points. However, in the current application, the situation is complicated by the fact that the observation points are at near-field distances and may, in fact, lie inside the loaded region. In such cases, it is necessary to also consider the contributions to the motion arising from Rayleigh waves converging on the origin from the exterior source region. The source/receiver geometries for these diverging and converging cases are compared in Figure 3. The solution for the Rayleigh wave component of the displacement in the converging wave case can be deduced from an analysis of the simpler halfspace problem (Bache, 1979; Murphy and Bache, 1979). Consider the case in which an axisymmetric impulsive

DIVERGING  $r > r_0$



CONVERGING  $r < r_1$

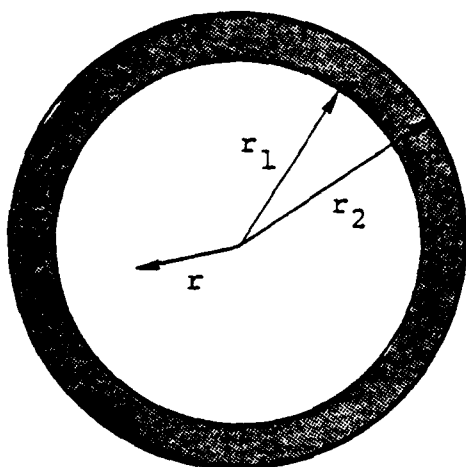


Figure 3. Comparison of diverging and converging Rayleigh wave geometry for axisymmetric loads acting on the surface of a multilayered halfspace.

surface load is applied at  $r'$  and the solution is sought at a surface observation point at range  $r$ . Then, it can be shown (Ewing, Jardetsky and Press, 1957, p.40) that the integral expression for the vertical component of displacement at  $r$  has the form:

$$w(\omega, r, r') = - \frac{1}{2\pi\mu} \int_0^\infty \frac{G(k)}{F(k)} J_0(kr) J_0(kr') dk \quad (2-3)$$

where

$$G(k) = \frac{\omega k}{\beta^2} \sqrt{k^2 - \frac{\omega^2}{\alpha^2}}$$

$$F(k) = \left(2k^2 - \frac{\omega^2}{\beta^2}\right)^2 - 4k^2 \sqrt{k^2 - \frac{\omega^2}{\alpha^2}} \sqrt{k^2 - \frac{\omega^2}{\beta^2}} \quad (2-4)$$

and  $\alpha, \beta$  are the compressional and shear wave velocities respectively. Using the identity

$$J_0(z) = \frac{H_0^{(1)}(z) + H_0^{(2)}(z)}{2} \quad (2-5)$$

Equation (2-3) can be expanded into a sum of four integrals of the form:

$$w(\omega, r, r') = - \frac{1}{8\pi\mu} \left[ \int_0^\infty \frac{G(k)}{F(k)} H_0^{(1)}(kr) H_0^{(1)}(kr') dk \right. \\ + \int_0^\infty \frac{G(k)}{F(k)} H_0^{(2)}(kr) H_0^{(2)}(kr') dk \\ + \int_0^\infty \frac{G(k)}{F(k)} H_0^{(1)}(kr) H_0^{(2)}(kr') dk \\ \left. + \int_0^\infty \frac{G(k)}{F(k)} H_0^{(2)}(kr) H_0^{(1)}(kr') dk \right] \quad (2-6)$$

Now, by replacing  $k$  by the complex argument  $k + i\tau$ , the path of integration can be deformed into the first or fourth quadrant as shown in Figure 4 where  $\times$  denotes the Rayleigh wave pole (i.e.,  $F(k) = 0$ ). Now for each of the integrals in

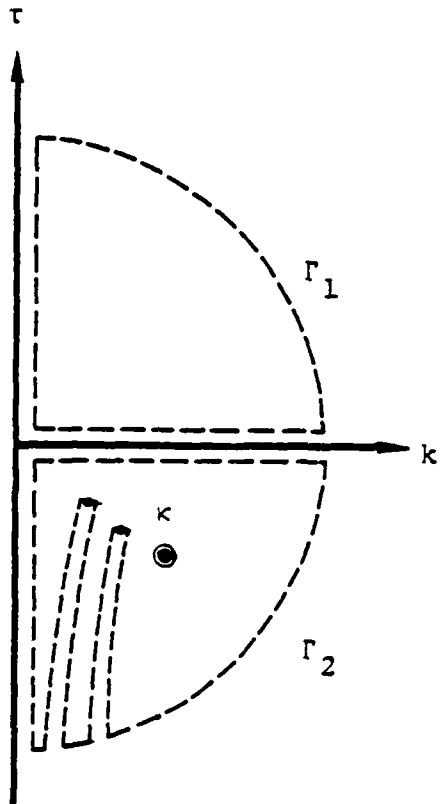


Figure 4. Path of integration for determination of Rayleigh wave contributions produced by axisymmetric surface loads.

Equation (2-6), the contour must be closed in the quadrant for which the integral along the arc (i.e.  $\Gamma_1$  or  $\Gamma_2$ ) vanishes. This choice is dictated by the asymptotic (i.e. large argument) behavior of the Hankel functions which are given by

$$\begin{aligned} H_0^{(1)}(x) &\approx \sqrt{\frac{2}{\pi x}} e^{ix} e^{-i\frac{\pi}{4}} \\ H_0^{(2)}(x) &\approx \sqrt{\frac{2}{\pi x}} e^{-ix} e^{i\frac{\pi}{4}} \end{aligned} \quad (2-7)$$

Now,  $r + r' > 0$  and consequently the first integral in (2-6) converges only if the contour is closed in the first quadrant and, since there are no singularities there, it makes no contribution to the solution. By the same reasoning, the contour for the second integral in (2-6) is always closed in the fourth quadrant yielding a residue contribution from the simple Rayleigh wave pole at  $k = \kappa$ . However, the evaluation of the third and fourth integrals in Equation (2-6) depends on the sign of  $r-r'$  and thus is different depending on whether  $r > r'$  (i.e. diverging) or  $r < r'$  (i.e. converging). Thus, for the diverging case, the third integral in (2-6) makes no contribution and combining the residue contributions from the pole at  $k = \kappa$  in the second and fourth integrals gives

$$W_0(\omega, r, r') = \frac{i}{2\mu} \frac{G(\kappa)}{F'(\kappa)} H_0^{(2)}(\kappa r) J_0(\kappa r') \quad r > r' \quad (2-8)$$

where  $F'(\kappa)$  denotes differentiation with respect to  $k$  followed by evaluation at  $\kappa$ . Similarly, for the converging case, the fourth integral in (2-6) does not contribute and combining the residue contributions from the second and third integral gives

$$W_0(\omega, r, r') = \frac{i}{2\mu} \frac{G(\kappa)}{F'(\kappa)} J_0(\kappa r) H_0^{(2)}(\kappa r') \quad r < r' \quad (2-9)$$

Thus, the converging Rayleigh wave solution can be obtained by interchanging the functional dependence of the source and propagation terms in the solution for diverging Rayleigh waves; and it follows that the solution for converging Rayleigh waves on a multilayered halfspace can be written down directly from Equation (2-1) as

$$\begin{aligned}\tilde{W}_j(\omega, r) &= -i\pi A_{R_j}(\omega) J_0(k_j r) \tilde{S}_j(\omega) \\ \tilde{U}_j(\omega, r) &= \varepsilon_j(\omega) \frac{J_1(k_j r)}{J_0(k_j r)} \tilde{W}_j(\omega, r)\end{aligned}\quad (2-10)$$

where

$$\tilde{S}_j(\omega) = \int_{r_1}^{r_2} p(r', \omega) H_0^{(2)}(k_j r') r' dr'. \quad (2-11)$$

Comparing Equations (2-10) and (2-1), it can be seen that the converging wave solution is characterized by a Bessel function propagation term as opposed to the more familiar Hankel function propagation term associated with the diverging wave solution. Thus, for the converging wave solution, the amplitude of the vertical component of motion reaches its maximum at the origin ( $r=0$ ) while the horizontal component vanishes at the center point as would be expected by symmetry. Clearly, for an observation point located within the loaded region, the total Rayleigh wave displacement will be given as a superposition of contributions arising from the two wave types given by Equations (2-1) and (2-10).

### 2.3 SCALING LAWS FOR RAYLEIGH WAVES

With reference to Equation (2-1), it can be seen that at a fixed distant observation point, the characteristics of the Rayleigh waves are determined primarily by the behavior of the source ( $S(\omega)$ ) and Rayleigh wave site response ( $A_R(\omega)$ ) functions. In this section, scaling laws will be derived for

each of these functions and then combined to assess the dependence of the Rayleigh wave spectrum on source and site parameters.

### 2.3.1 Source Scaling

In order to define scaling laws for the Rayleigh wave source function,  $S(\omega)$ , it is first necessary to specify the functional dependence of the airblast load. Following Brode (1968) this will be approximated as

$$p(r, \tau) = \Delta P_s (1-\tau) (ae^{-\alpha\tau} + be^{-\beta\tau} + ce^{-\gamma\tau}) \quad (2-12)$$

where  $a$ ,  $b$ ,  $c$ ,  $\alpha$ ,  $\beta$ ,  $\gamma$  are pressure-dependent constants usually given in tabular form,  $\Delta P_s$  is the peak shock pressure given by

$$\Delta P_s = \frac{3152W}{r^3} + \frac{240W^{\frac{1}{2}}}{r^{\frac{3}{2}}} + 0.0215 \quad (2-13)$$

for  $\Delta P_s$  in psi, yield  $W$  in megatons and range  $r$  in kilofeet and  $\tau$  is the reduced time defined by

$$\tau = \frac{t - t_s}{D_p} \quad (2-14)$$

where  $t_s$  is the shock arrival time and  $D_p$  is the duration of the positive phase. It follows from (2-12) and (2-14) that the Fourier transform of the airblast load can be written in the form

$$p(r, \omega) = \Delta P_s D_p e^{-i\omega t_s} \left[ \frac{a}{\alpha + i\omega D_p} \left( 1 - \frac{1}{\alpha + i\omega D_p} \right) + \frac{b}{\beta + i\omega D_p} \left( 1 - \frac{1}{\beta + i\omega D_p} \right) + \frac{c}{\gamma + i\omega D_p} \left( 1 - \frac{1}{\gamma + i\omega D_p} \right) \right] \quad (2-15)$$

Consider first the low-frequency limit. Now

$$\lim_{\omega \rightarrow 0} J_0(kr) \rightarrow 1 \quad (2-16)$$

and it follows from Equation (2-2) that

$$\lim_{\omega \rightarrow 0} S(\omega) = \int_{r_0}^{\infty} \lim_{\omega \rightarrow 0} p(r', \omega) r' dr'. \quad (2-17)$$

But, by the definition of the Fourier transform,

$$\lim_{\omega \rightarrow 0} p(r', \omega) = \int_0^{\infty} p(r', t) dt \quad (2-18)$$

and thus

$$\lim_{\omega \rightarrow 0} S(\omega) = \int_0^{\infty} \int_0^{\infty} p(r', t) r' dt dr' \quad (2-19)$$

which is easily recognized as the total impulse delivered by the airblast. Now, by Equation (2-13) the peak pressure  $\Delta P_s$  is invariant under cube-root scaling and, consequently, at the same scaled distance the impulse is proportional to  $W^{\frac{1}{3}}$  (i.e.,  $D_p^{\frac{1}{3}}$ ). Moreover, the area over which it is applied is proportional to  $r^2$  and thus proportional to  $W^{\frac{2}{3}}$ . Thus, the total impulse is directly proportional to yield, or

$$\lim_{\omega \rightarrow 0} S(\omega) \sim W \quad (2-20)$$

independent of the site characteristics.

In the high-frequency limit, Equation (2-15) simplifies to

$$\lim_{\omega \rightarrow \infty} p(r, \omega) = \Delta P_s e^{-i\omega t_s} \frac{a+b+c}{i\omega}. \quad (2-21)$$

But from (2-12), the condition  $p(r, 0) = \Delta P_s$  implies  $a+b+c = 1$  and it follows that

$$\lim_{\omega \rightarrow \infty} p(r, \omega) = \frac{\Delta P_s}{i\omega} e^{-i\omega t_s} \quad (2-22)$$

Furthermore, when  $\omega$  is large,  $kr$  is also large over the range of integration  $r_0$  to  $\infty$  and thus the Bessel function in (2-2) can be replaced by its asymptotic approximation

$$\begin{aligned} J_0(kr) &\approx \sqrt{\frac{2}{\pi kr}} \sin\left(kr + \frac{\pi}{4}\right) \\ &= -i \sqrt{\frac{\tilde{c}}{2\pi\omega r}} \left\{ e^{i\frac{\pi}{4}} e^{i\omega\frac{r}{\tilde{c}}} - e^{-i\frac{\pi}{4}} e^{-i\omega\frac{r}{\tilde{c}}} \right\} \end{aligned} \quad (2-23)$$

where  $\tilde{c}$  denotes the Rayleigh wave phase velocity ( $\tilde{c} = \omega/k$ ). It follows that in the high-frequency limit Equation (2-2) takes the form

$$\begin{aligned} \lim_{\omega \rightarrow \infty} S(\omega) &= -\frac{1}{\omega^{\frac{3}{2}}} \sqrt{\frac{\tilde{c}}{2\pi}} \left\{ e^{i\frac{\pi}{4}} \int_{r_0}^{\infty} r'^{-\frac{1}{2}} \Delta P_s(r') e^{-i\omega[t_s(r') - \frac{r'}{\tilde{c}}]} dr' \right. \\ &\quad \left. - e^{-i\frac{\pi}{4}} \int_{r_0}^{\infty} r'^{-\frac{1}{2}} \Delta P_s(r') e^{-i\omega[t_s(r') + \frac{r'}{\tilde{c}}]} dr' \right\}. \end{aligned} \quad (2-24)$$

Now  $t_s, r' > 0$  and it follows that the integrand in the second term of (2-24) is highly oscillatory in the high-frequency limit and thus the contribution of this term to the solution is negligible. Likewise, in the first integral in (2-24), over the range in which the quantity  $t_s(r') - r'/\tilde{c}$  is rapidly varying, this term will contribute little to the solution. It follows then that in the high-frequency limit, the solution depends only on the behavior of the first integral in the vicinity of  $r = \tilde{r}$  where  $\tilde{r}$  is the point at which

$$t_s'(r) \equiv \frac{1}{V(r)} = \frac{1}{\tilde{c}} \quad (2-25)$$

where the prime denotes differentiation with respect to  $r$  and  $V(r)$  is the propagation velocity of the airblast at  $r$

(such a point will always exist in the range of integration  $r_0' \propto$  provided  $\tilde{c} > V_0$  where  $V_0$  is the sound velocity in air). This contribution can be evaluated by the principle of stationary phase (Papoulis, 1962, p.140) to obtain

$$\lim_{\omega \rightarrow \infty} \int_{r_0}^{\infty} r^{1/2} \Delta P_s(r') e^{-i\omega \left[ t_s(r') - \frac{r'}{\tilde{c}} \right]} dr' \quad (2-26)$$

$$= \tilde{r}^{1/2} \Delta P_s(\tilde{r}) \sqrt{\frac{2\pi}{\omega |t_s''(\tilde{r})|}} e^{-i\omega \left[ t_s(\tilde{r}) - \frac{\tilde{r}}{\tilde{c}} \right]} e^{i\frac{\pi}{4}}$$

and it follows from (2-24) that

$$\lim_{\omega \rightarrow \infty} |S(\omega)| = \frac{\Delta P_s(\tilde{r})}{\omega^2} \sqrt{\frac{\tilde{c} \tilde{r}}{|t_s''(\tilde{r})|}} \quad (2-27)$$

Thus, at high frequencies the Rayleigh wave source spectrum is proportional to  $\omega^{-2}$ . The yield and site dependence of the spectral amplitude level at high-frequencies can be evaluated from (2-27) once the dependence of  $t_s$  on  $r$  has been specified. For example, at ranges greater than  $159W^{1/3}m$  (W in megatons) Brode (1968) suggests

$$t_s(r) \sim \frac{r^{5/2}}{W^{1/2}} \quad (2-28)$$

and it follows that

$$t_s''(\tilde{r}) \sim \frac{\tilde{r}^{5/2}}{W^{1/2}} \quad (2-29)$$

But  $\tilde{r} \sim W^{1/3}$  which implies  $t''(\tilde{r}) \sim W^{-1/3}$  and, using the fact that  $\Delta P_s$  is invariant under cube-root scaling, it follows from (2-27) that

$$\lim_{\omega \rightarrow \infty} |S(\omega)| \sim W^{1/3} \quad (2-30)$$

A similar line of reasoning can be followed to deduce the dependence of the high-frequency spectral amplitude level on the site geology, which enters through the Rayleigh wave phase velocity  $\tilde{c}$ . Suppose that at a fixed high-frequency  $\omega_0$  and yield  $W$  the phase velocity at one site is  $\tilde{c}_1$  and at another site is  $\tilde{c}_2$  where  $\tilde{c}_2 = k \tilde{c}_1$ . Now, if the airblast propagation velocity  $V(r) = \tilde{c}_1$  at  $r = r_1$ , it follows from (2-28) that  $V(r) = \tilde{c}_2$  at  $r = r_2$  where  $r_2 = r_1/k^{2/3}$ . Then it follows from (2-27) that

$$\left| \frac{S_2(\omega_0)}{S_1(\omega_0)} \right| = \frac{\Delta P_s \left( \frac{r_1}{k^{2/3}} \right)}{\Delta P_s(r_1)} k^{1/3} \quad (2-31)$$

and, since  $\Delta P_s$  is a decreasing function of  $r$ ,  $\lim_{\omega \rightarrow \infty} |S(\omega)|$  increases as  $\tilde{c}$  increases. Moreover, in the high-frequency limit,  $\tilde{c}$  is proportional to the near-surface shear wave velocity and thus the high-frequency Rayleigh wave spectral amplitude level will increase as the near-surface shear wave velocity increases.

These scaling laws are summarized graphically in Figures 5 and 6. Figure 5 shows a schematic representation of the Rayleigh wave source spectra corresponding to explosive yields  $W_1, W_2$  with  $W_2 > W_1$ . By Equation (2-19) the spectral amplitude levels approach constant values at low frequencies (i.e., the respective total impulses) and this level scales as the first power of the yield. At high-frequencies, by Equation (2-27), the spectra are proportional to  $\omega^{-2}$  and the spectral amplitude level at a fixed high-frequency is proportional to  $W^{1/3}$ . This implies the existence of a corner frequency which scales like  $W^{-1/3}$ , such as that shown on this figure. Figure 6 shows a schematic representation of the Rayleigh wave source spectra corresponding to two different sites characterized by high-frequency phase velocities  $\tilde{c}_1, \tilde{c}_2$ .

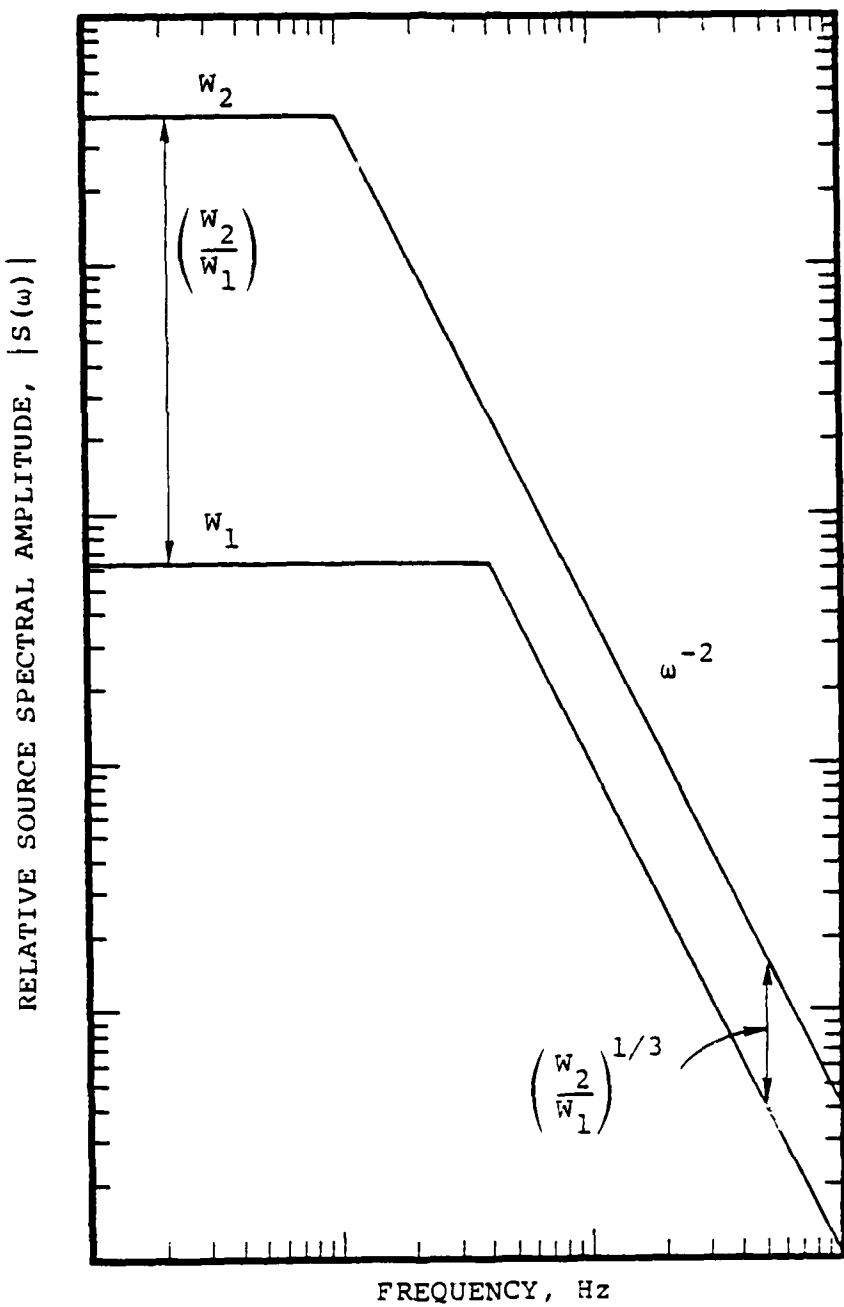


Figure 5. Schematic diagram illustrating the yield dependence of the Rayleigh wave source functions at a fixed site.

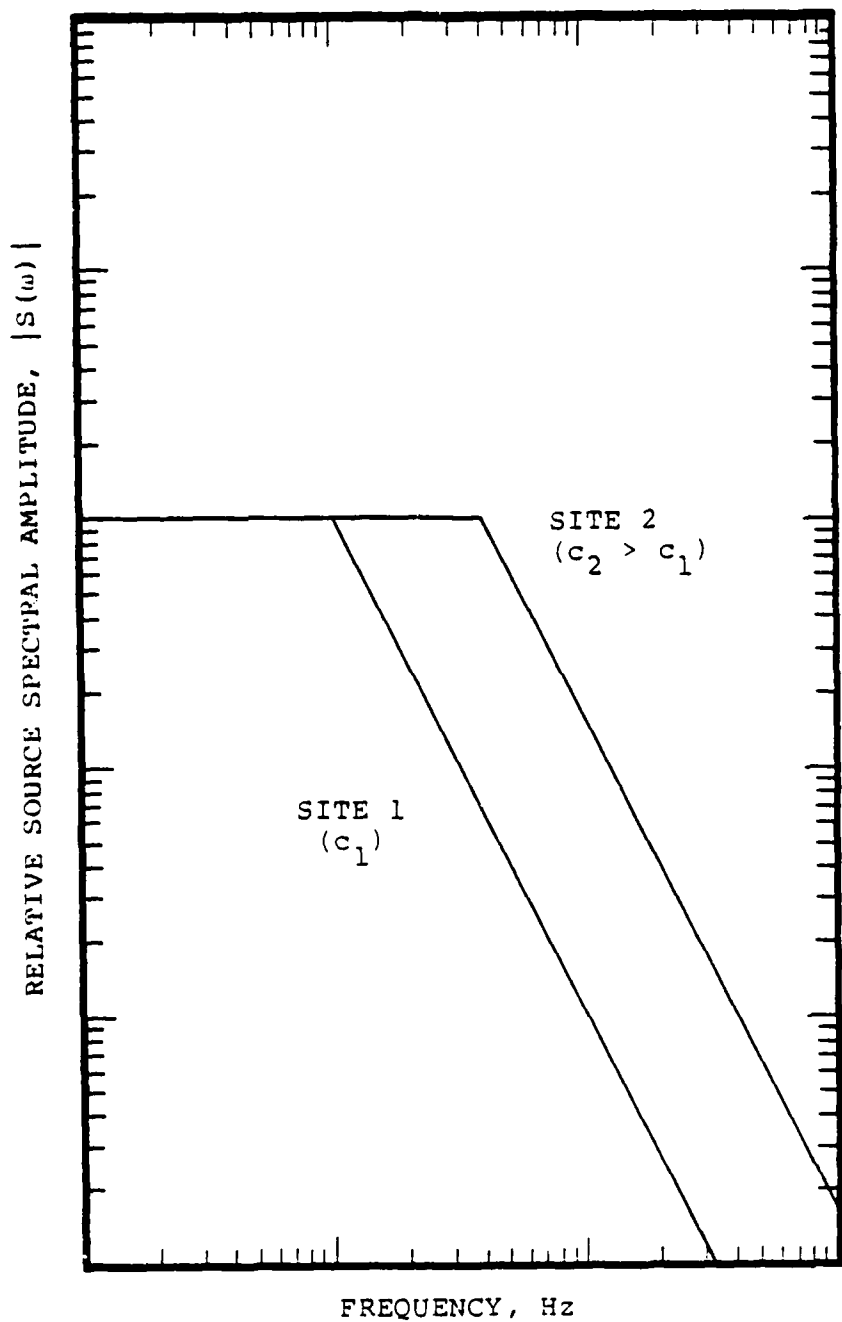


Figure 6. Schematic diagram illustrating the site dependence of the Rayleigh wave source function at a fixed yield.

with  $\tilde{c}_2 > \tilde{c}_1$ . Since the low-frequency spectral amplitude level is independent of the site geology and the high-frequency spectral amplitude level increases with increasing  $\tilde{c}$ , it follows that the site with the higher value of  $\tilde{c}$  must be characterized by a higher corner frequency leading to a difference in spectral composition such as that shown on this figure.

### 2.3.2 Site Scaling

The Rayleigh wave site response function,  $A_R(\omega)$ , incorporates all the complexity of the subsurface geology and, consequently, in the general case the relationship between the spectral composition of  $A_R(\omega)$  and the physical properties of the site is not a simple one. However, for the special case of a single layer over a halfspace, a simple scaling law can be derived which provides insight into the response characteristics of some more complicated geologic models, including those of interest in MX siting.

The simple-layer-over-halfspace model selected for analysis is shown in Figure 7, where it is indicated that the layer thickness ( $H$ ) and shear wave velocity in the layer ( $\beta_1$ ) will be considered as free parameters to be varied. Figures 8 and 9 show the fundamental mode  $A_R(\omega)$  as a function of frequency for different values of  $H$  and  $\beta_1$ . Figure 8 shows the variation with  $H$  at a fixed value of  $\beta_1$  (316 m/sec); Figure 9 shows the variation with  $\beta_1$  at a fixed value of  $H$  (12 m). In general, the  $A_R$  functions are characterized by a well defined corner frequency below which the response drops off very rapidly and above which the response increases at a rate which asymptotically approaches the first power of frequency (Harkrider et al, 1974). A more important observation with regard to the present investigation is that these corner frequencies correlate very well with the frequencies of minimum group velocity which are indicated by the locations of the tips of the arrows on these two figures. The

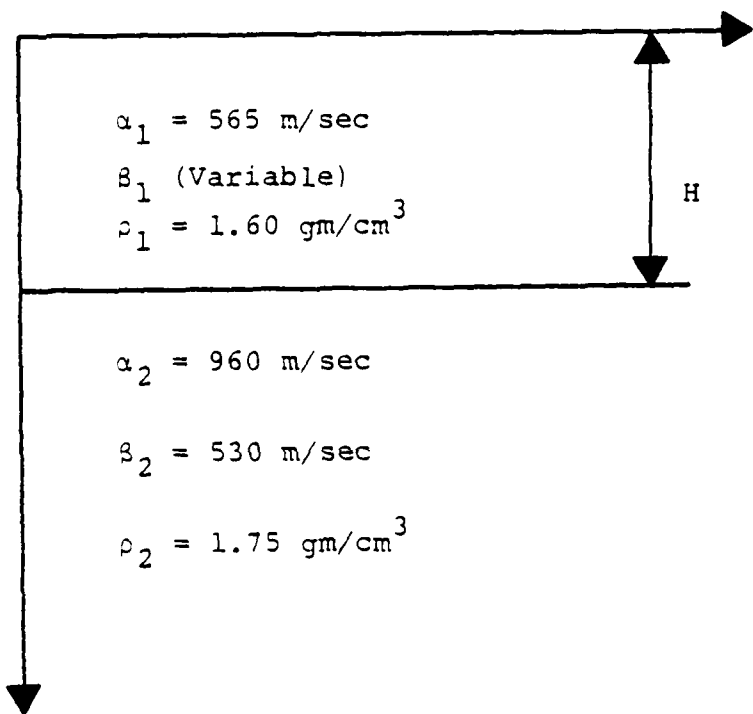


Figure 7. Geologic model for the parametric study of the Rayleigh wave site response function.

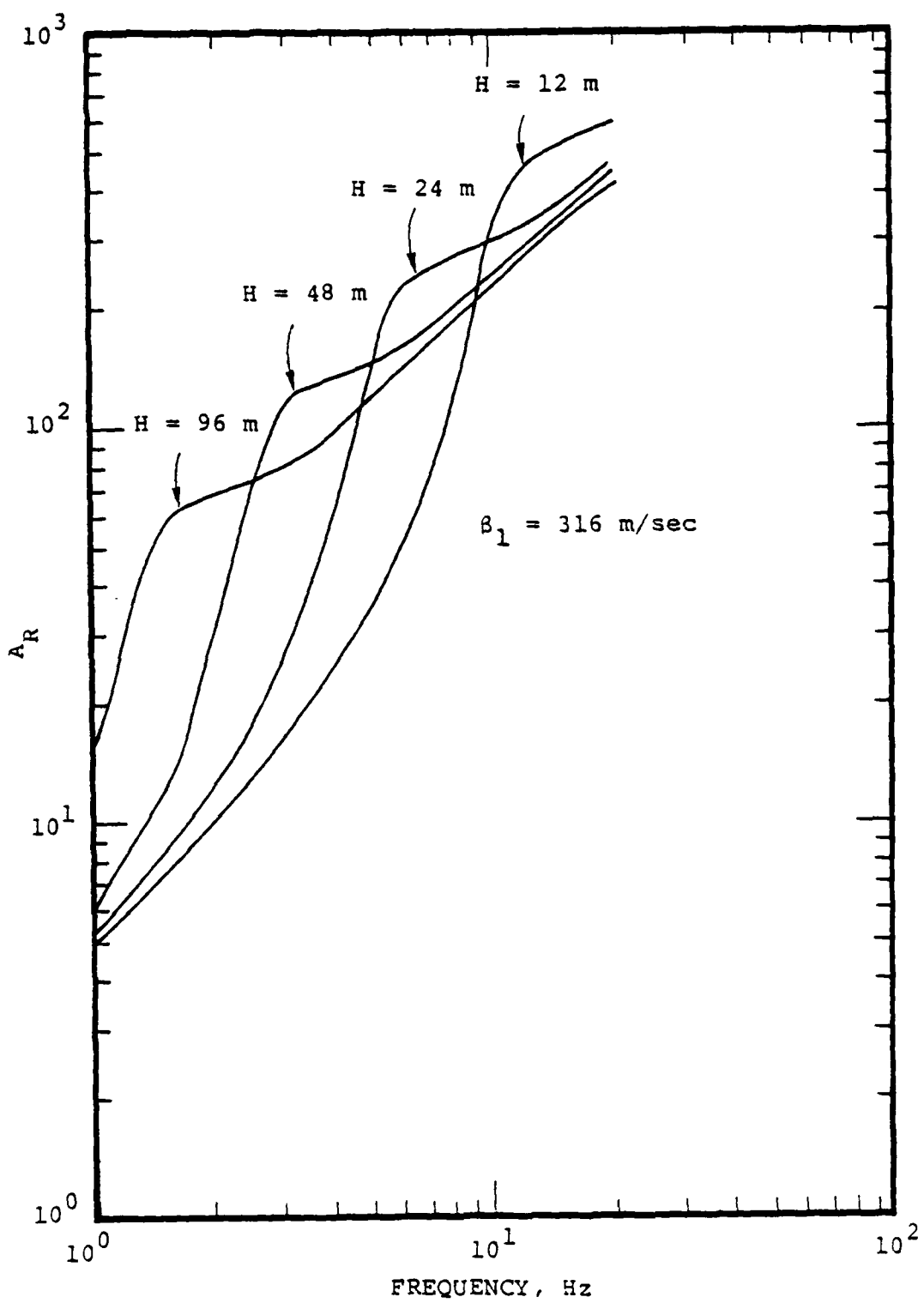


Figure 8. Variation of  $A_R$  spectral response as a function of  $H$  for a fixed value of  $\beta_1$ .

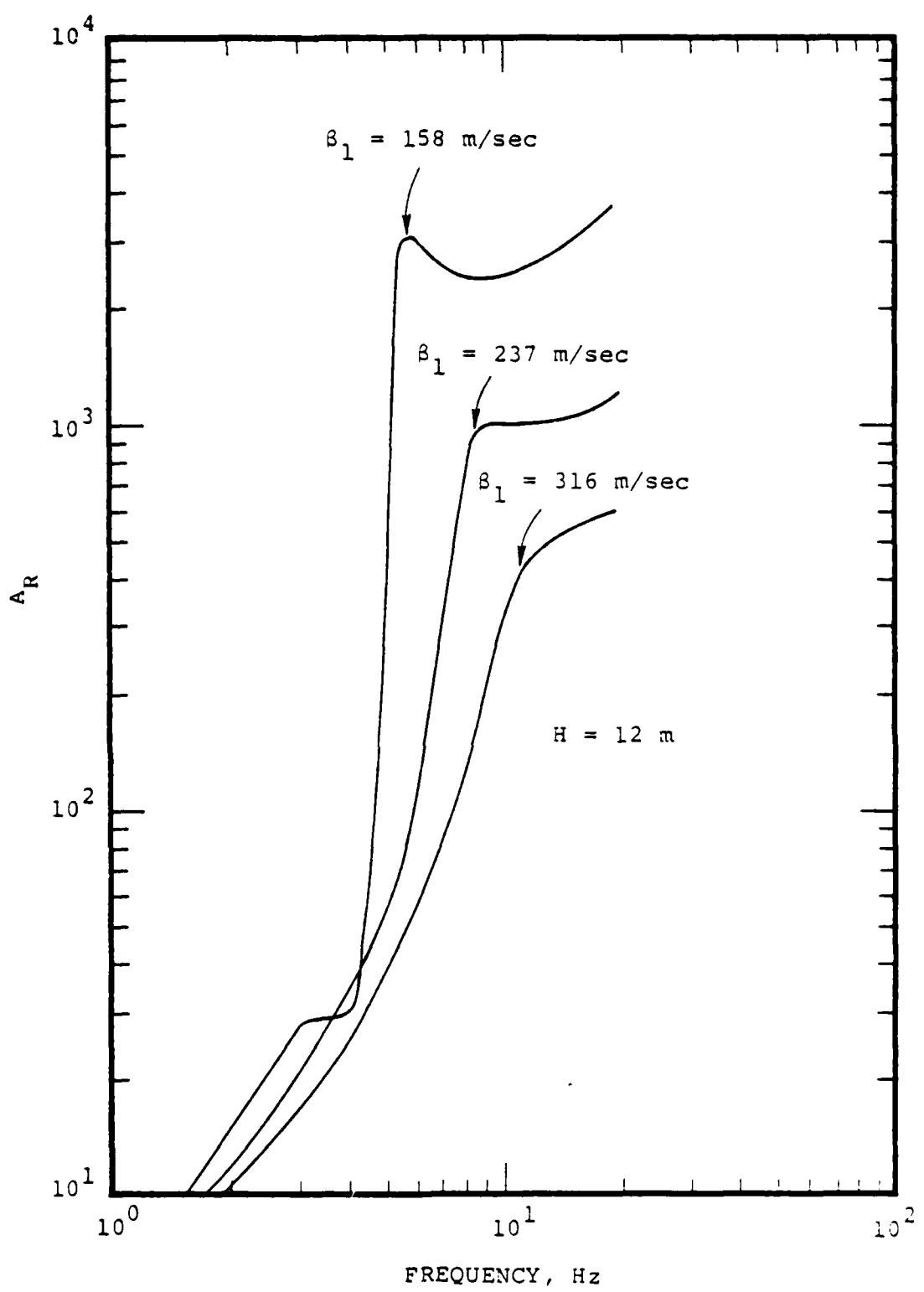


Figure 9. Variation of  $A_R$  spectral response as a function of  $\beta_1$  for a fixed value of  $H$ .

significance of this fact is that it can be shown that for a wide range of physical property choices, the frequency of minimum group velocity is directly proportional to  $\beta_1$  and inversely proportional to  $H$ . In fact, for the fundamental mode, this frequency ( $f_c$ ) can be approximated very closely by the relation (Mooney and Bolt, 1966)

$$f_c = \frac{\beta_1}{2.3H} . \quad (2-32)$$

While this relation strictly applies only to the single-layer-over-halfspace problem, it has been found that it can be applied to MX-type geologic environments with the following modifications. Let  $\bar{H}$  denote the depth to the first significant discontinuity in the shear wave velocity (e.g., soil/rock interface) and  $\bar{\beta}$  the depth-averaged shear wave velocity given by

$$\bar{\beta} = \frac{\sum_i \frac{H_i}{\beta_i}}{\sum_i \left( \frac{H_i}{\beta_i} \right)} \quad (2-33)$$

where  $\sum_i H_i = \bar{H}$ . Then, the corner frequency of the fundamental mode site response function can be approximated as (Auld and Murphy, 1979)

$$f_c \approx \frac{\bar{\beta}}{2\bar{H}} . \quad (2-34)$$

### 2.3.3 Rayleigh Wave Scaling Relations

It now remains to combine the scaling laws for  $S(\omega)$  and  $A_R(\omega)$  so that the dependence of the total Rayleigh wave spectrum on yield and site characteristics can be assessed. Figure 10 shows a schematic representation of the  $A_R$  functions for two hypothetical sites. It can be seen that in both cases the amplitude response increases as  $\omega^3$  up to

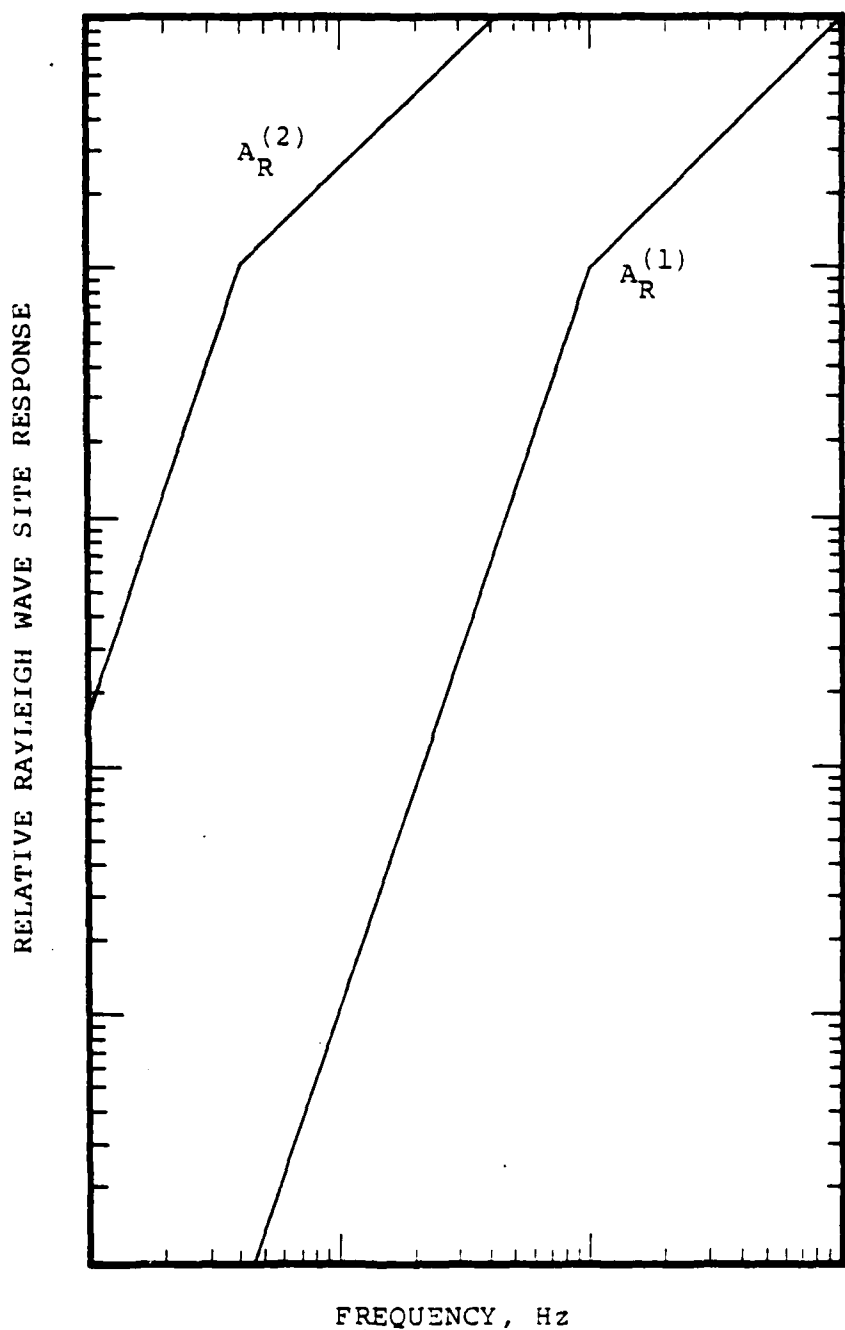


Figure 10. Schematic representation of the  $A_R$  spectral response at two hypothetical sites.

widely-separated corner frequencies above which the response increases more gradually (i.e.  $\sim \omega$ ). These spectra have been multiplied by the simplified source spectra of Figure 5 to illustrate the range of possible Rayleigh wave yield scaling conditions. Figure 11 shows the results of multiplying the source functions of Figure 5 by the  $A_R^{(2)}$  Rayleigh wave site response function of Figure 10. In this case, the corner frequency of the site response function lies below the corner frequency of the source functions and as a result the peak Rayleigh wave spectral response scales with the source function. That is, the frequency of maximum spectral amplitude level scales as  $W^{-1/3}$  and the maximum amplitude level is directly proportional to  $W^{2/3}$ . However, as is illustrated in Figure 12, the result is quite different when these same two source functions are multiplied by the  $A_R^{(1)}$  site response function of Figure 10. In this case, the source function corner frequencies lie below the corner frequency of the site response function which now controls the frequency of maximum Rayleigh wave response. Consequently, in this case, the dominant Rayleigh wave frequency is independent of yield and the maximum spectral amplitude is proportional to  $W^{1/3}$ . Although the above examples have contrasted the effects of different site response characteristics, it should be noted that since the source function corner frequency is proportional to  $W^{-1/3}$ , there will be a yield level for every site above which the dominant Rayleigh wave frequency remains constant. It will be shown in the following section that for the range of MX prototype geologies considered to date, this yield threshold appears to be of the order of a few hundred kilotons.

#### 2.4 RAYLEIGH WAVE GROUND MOTION ESTIMATES FOR SOME PROTOTYPE MX SITES

Most of the siting alternatives currently being considered for the MX system involve deployment in one or more

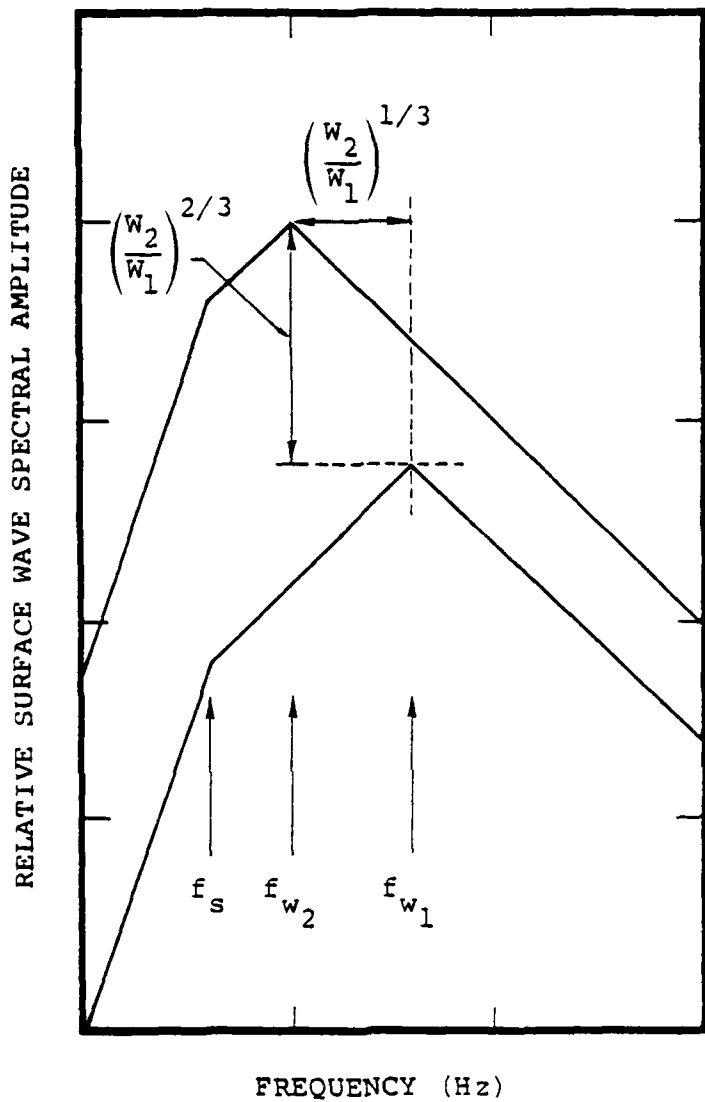


Figure 11. Schematic diagram illustrating the Rayleigh wave yield scaling relations for site A<sup>(2)</sup>. Here  $f_s$  denotes the site corner frequency and  $f_{w_i}$  denotes the source function corner frequency for yield  $W_i$ .

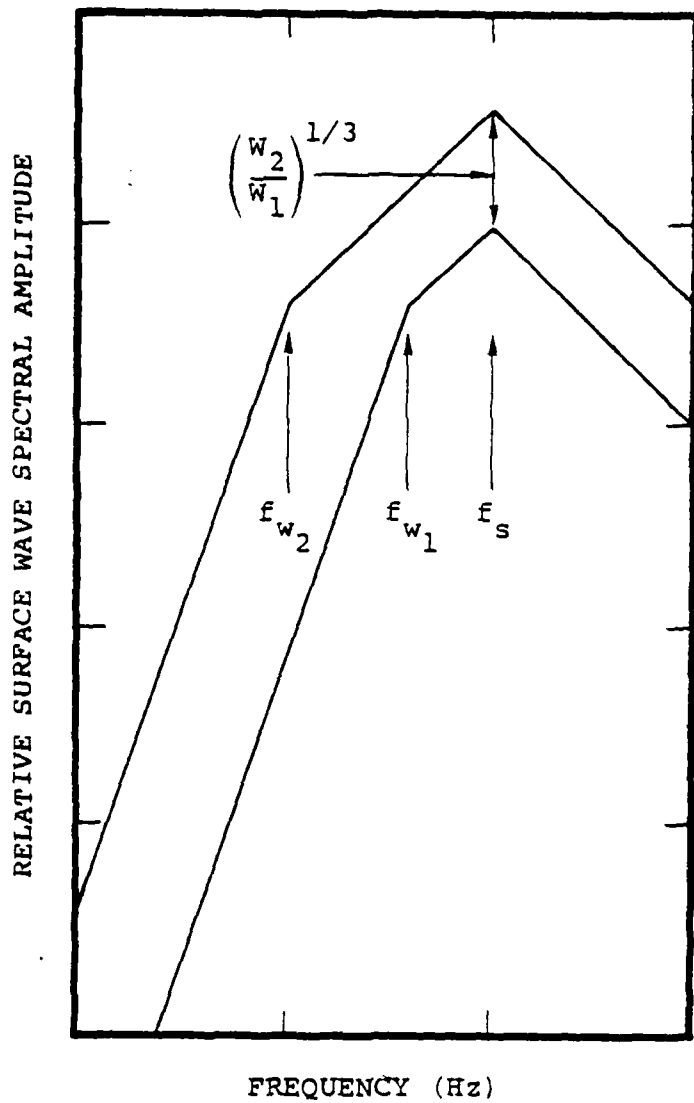


Figure 12. Schematic diagram illustrating the Rayleigh wave yield scaling relations for site  $A^{(1)}$ . Here  $f_s$  denotes the site corner frequency and  $f_{w_i}$  denotes the source function corner frequency for yield  $w_i$ .

valleys located somewhere in the Basin and Range Province of the southwestern U.S. Thus, it is possible to specify the range of site geologies that may be encountered and use these site descriptions to estimate the characteristics of the low-frequency ground motion environment to be expected under a variety of conditions. Subsurface geologic profiles for the five sites selected for analysis by the Data Analysis Working Group (1978) are shown in Figures 13 and 14. It can be seen that they are all characterized by a relatively thick surficial layer of soil (90 to 1000 m) representing the alluvium-filled valleys. The physical properties which have been assigned to the various geologic units are summarized in Table 1. Note that for these models the first significant discontinuity in the shear wave velocity always occurs at the soil/rock interface. Thus, although the water table represents a significant discontinuity in compressional wave velocity, it corresponds to only a relatively minor change in the shear wave velocity.

The fundamental mode, Rayleigh wave site response functions for these five sites are shown in Figures 15 through 17. It can be seen that the computed corner frequencies (i.e.,  $f_C$ ) vary over a broad range (0.3 to 2.3 Hz). Moreover, if  $\bar{H}$  is defined as the total soil thickness and  $\bar{v}$  the average soil velocity, then it can be shown that the corner frequencies for these five cases scale in very good agreement with Equation (2-34). In terms of the examples shown in Section 2.3.3 above, however, the question remains as to whether the dominant Rayleigh wave frequency will be controlled by the source or site response characteristics for attack scenarios of interest. In order to address this question, a series of calculations have been performed assuming that each of the five sites was loaded with the airblast to be expected from a single, one megaton surface burst.

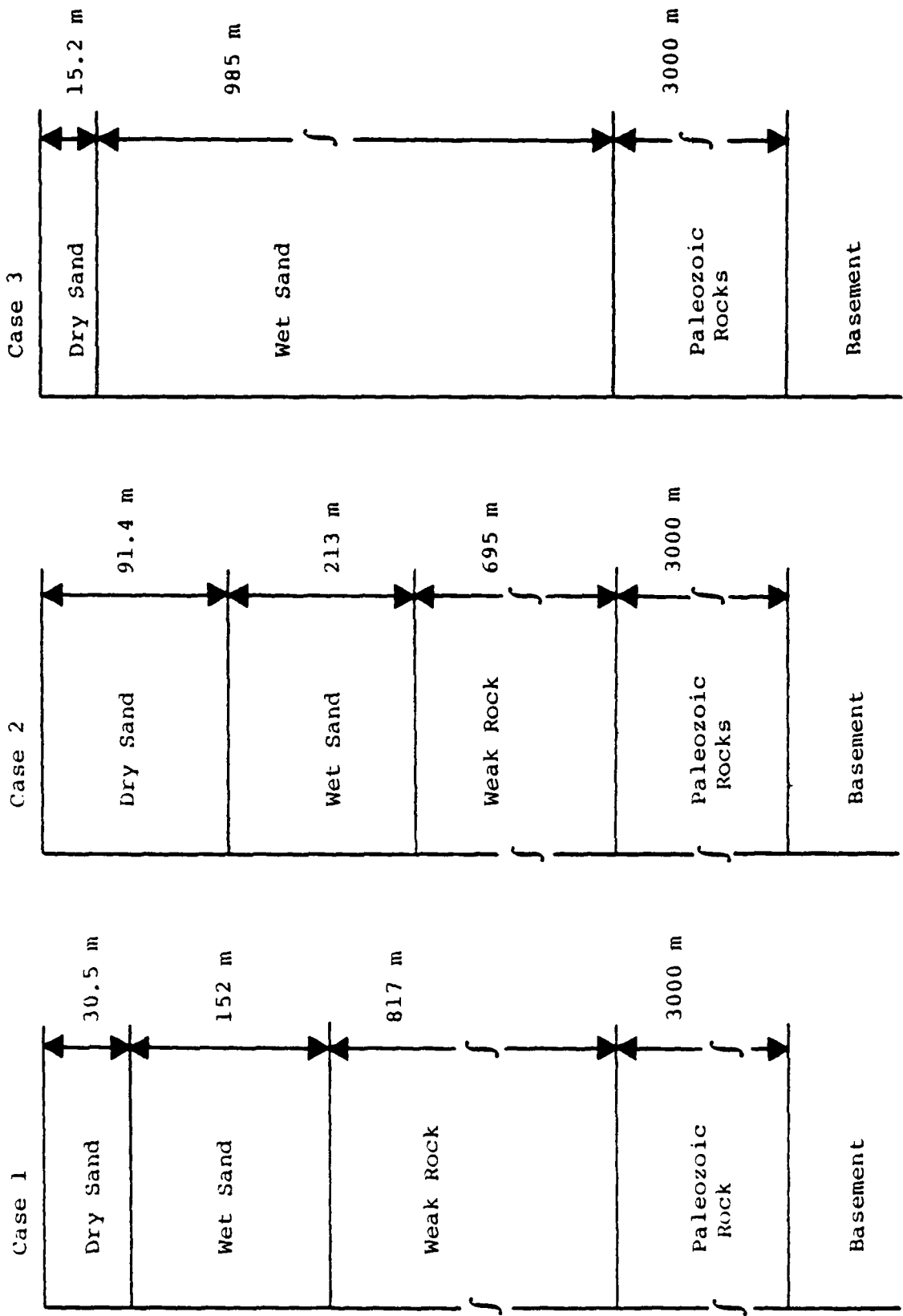


Figure 13. Subsurface geologic profiles for MX prototype cases 1 through 3.

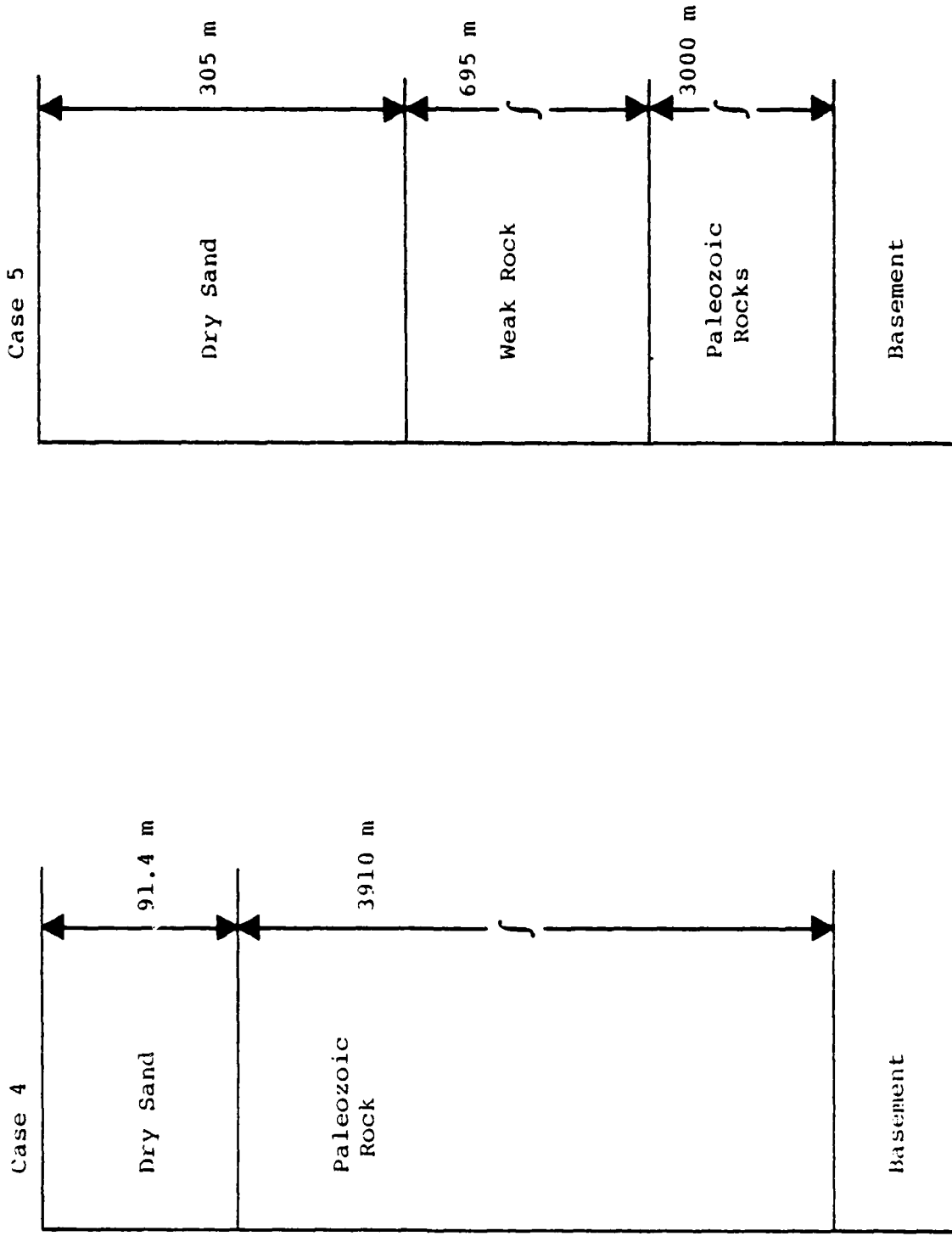


Figure 14. Subsurface geologic profiles for MX prototype cases 4 and 5.

TABLE 1  
PHYSICAL PROPERTY DATA

MEDIUM	COMPRESSIVE WAVE VELOCITY, km/sec	SHEAR WAVE VELOCITY, km/sec	DENSITY, gm/cm <sup>3</sup>
Dry Sand	0.91	0.46	1.84
Wet Sand	1.98	0.58	2.00
Weak Rock	2.74	1.58	2.40
Paleozoic Rocks	4.00	2.32	2.40
Basement	5.80	3.36	2.80

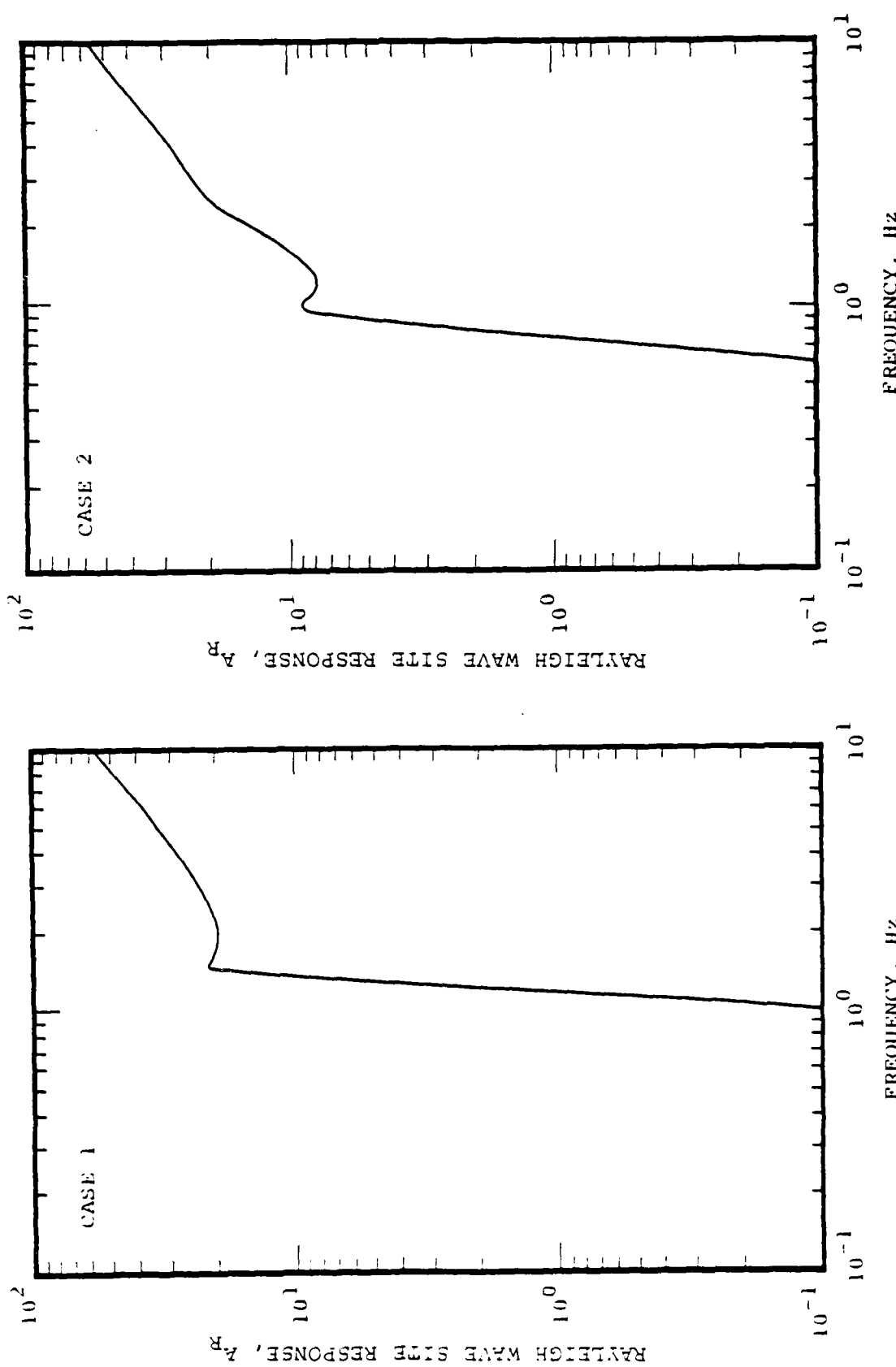


Figure 15. Fundamental mode Rayleigh wave site response functions for Cases 1 and 2.

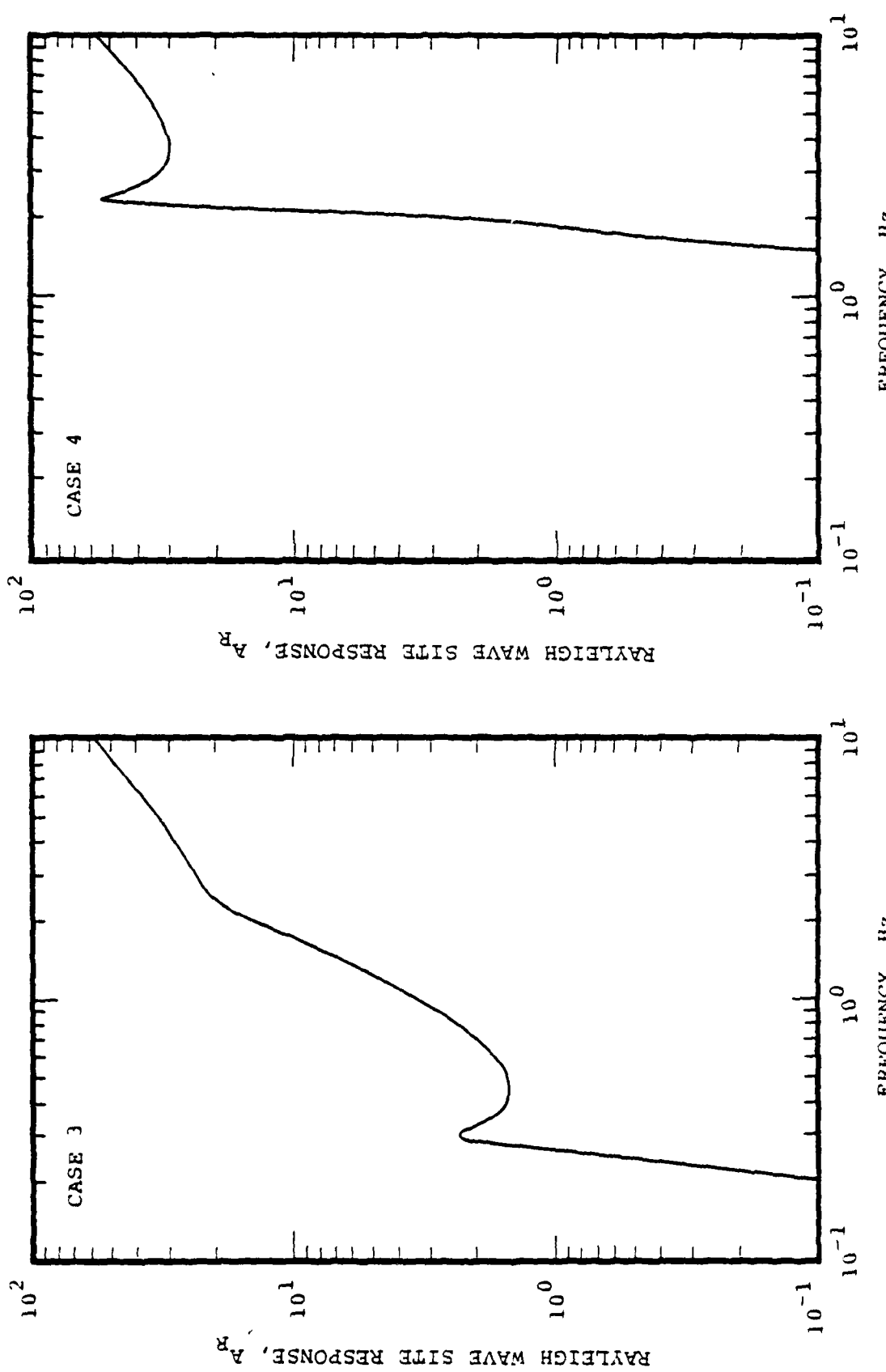


Figure 16. Fundamental mode Rayleigh wave site response functions for Cases 3 and 4.

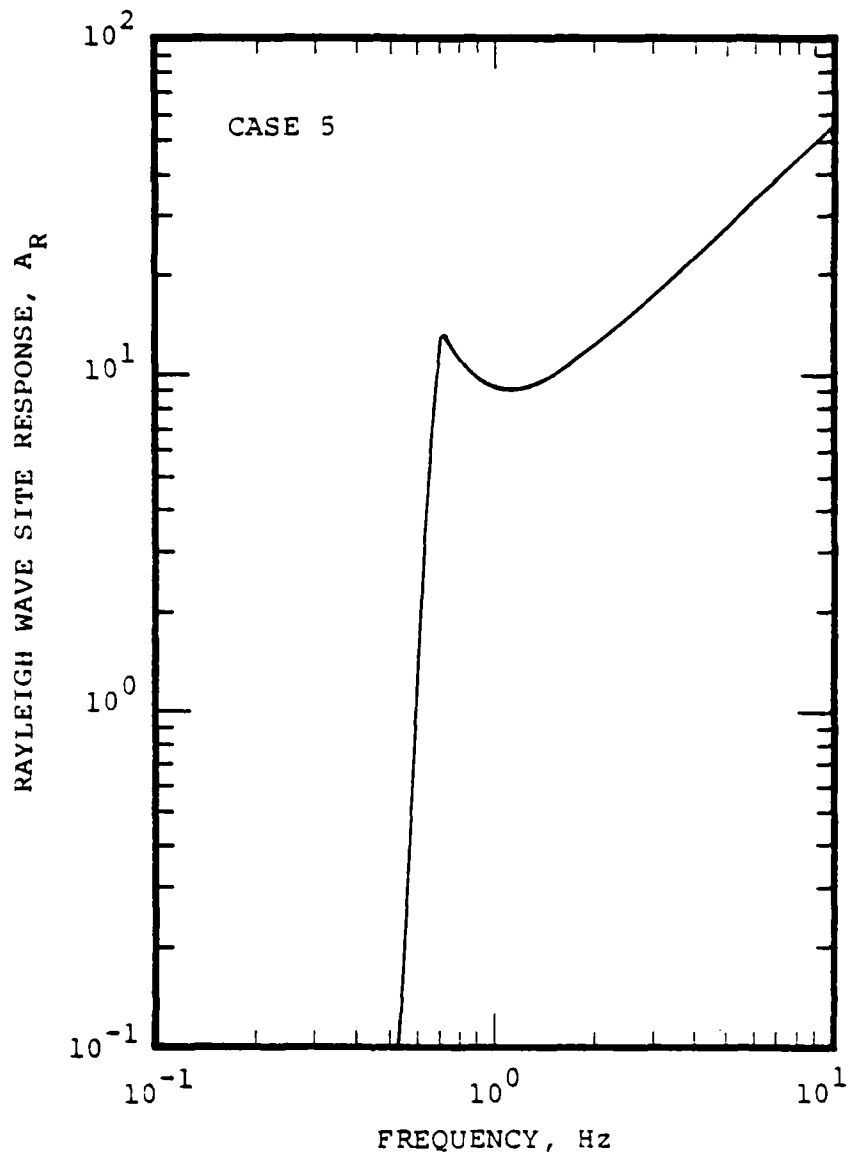


Figure 17. Fundamental mode Rayleigh wave site response function for Case 5.

As in the case of the previous HE calculations (Murphy, 1978) the airblast load for the Rayleigh wave calculations has been approximated by a series of simple functions of the form

$$p(r, t) = C_i e^{-\alpha_i r} e^{-\beta_i (t - \tau_i)} H(t - \tau_i) \quad (2-35)$$

in order to simplify the numerical calculations. Here, the subscript  $i$  denotes the fact that a series (i.e., four) of such functions is used to describe the overpressure in various distance ranges,  $\tau_i$  denotes the arrival time of the airblast at radius  $r$  and  $H$  is the unit step function. Taking the Fourier transform of Equation (2-35) and substituting into Equation (2-2) leads to the following expression for the diverging component of the Rayleigh wave source function:

$$S_j(\omega) = \sum_{i=1}^4 \frac{C_i e^{-i\omega \tilde{\tau}_i} (\beta_i - i\omega)}{s_i^2 + \omega^2} \left[ \int_{r_{i-1}}^{r_i} r' e^{-ar'} J_0(k_j r') \cos \frac{\omega}{U_i} r' dr' \right. \\ \left. - i \int_{r_{i-1}}^{r_i} r' e^{-ar'} J_0(k_j r') \sin \frac{\omega}{U_i} r' dr' \right] \quad (2-36)$$

where  $j$  denotes the mode number,  $U_i$  is the average airshock propagation velocity across the surface disk bounded by  $r_{i-1}$  and  $r_i$  and  $\tilde{\tau}_i$  is the arrival time of the shock at  $r_{i-1}$ . A similar relation holds for the converging component of the source function (i.e.,  $\tilde{S}_j(\omega)$ , Equation (2-11)) with the Hankel function replacing the Bessel function in the integrands of Equation (2-36). The parameters of the overpressure fit for this case have been computed by scaling those from the 100-ton fit (Murphy, 1978) to a yield of one megaton and are given in Table 2. It can be seen from this table that the innermost disk extending from the origin out to 246 m is loaded with an overpressure which is of considerably lower amplitude than that which would ordinarily be predicted in

TABLE 2  
 PARAMETERS FOR AIRBLAST APPROXIMATION:  
 1 Mt SURFACE BURST

i	$r_{i-1}, m$	$r_i, m$	$C_i, \text{psi}$	$\alpha_i, m^{-1}$	$\beta_i, \text{sec}^{-1}$	$u_i, m/\text{sec}$
1	0	246	3,500	0	23.2	17,980
2	246	657	33,666	$2.10 \times 10^{-3}$	9.28	2,865
3	657	2627	1,124	$5.10 \times 10^{-4}$	3.71	610
4	2627	6567	36	$1.11 \times 10^{-4}$	0.93	380

this range for an explosion of this yield. This reflects the observation that loading inside this scaled radius does not seem to be efficiently coupled into radiated surface waves. The reason for this effect is not known at this time, but may be related to energy losses associated with crater formation and other strong nonlinear interactions which are known to take place in the immediate vicinity of ground zero (Murphy, 1978).

The above defined loading conditions have been used to compute Rayleigh wave ground motion time histories for each of the five prototype MX sites. The resulting fundamental-mode displacement components at a fixed range of 1800 m are shown in Figures 18 through 26. For Cases 1 through 4, displacement time histories computed using finite difference codes are also shown for purposes of comparison. The finite difference solutions for Cases 1 through 3, which are shown in Figures 18 through 23, were computed using a nonlinear finite difference code in which the geologic models were driven by the complete airblast loading expected from a one megaton surface burst (Sandler, 1978). The finite difference solutions for Case 4, on the other hand, were computed using a linear, elastic finite difference code in which the geologic model was driven by a modified airblast load comparable to that defined by Equation (2-35) and Table 2 (Auld, 1978). Although the details of the modeling assumptions are different enough to preclude absolute amplitude comparisons at this time, the general character of the low-frequency ground motions, including dominant frequency and relative displacement amplitude levels between sites, would be expected to agree fairly well. This seems to be true for Cases 1 through 3, for which it appears that the fundamental mode Rayleigh wave dominates the displacement motions at this range. However, the agreement between the computed motions for Case 4 is not nearly as good, and this is somewhat puzzling in that the airblast loading functions used in the finite difference and

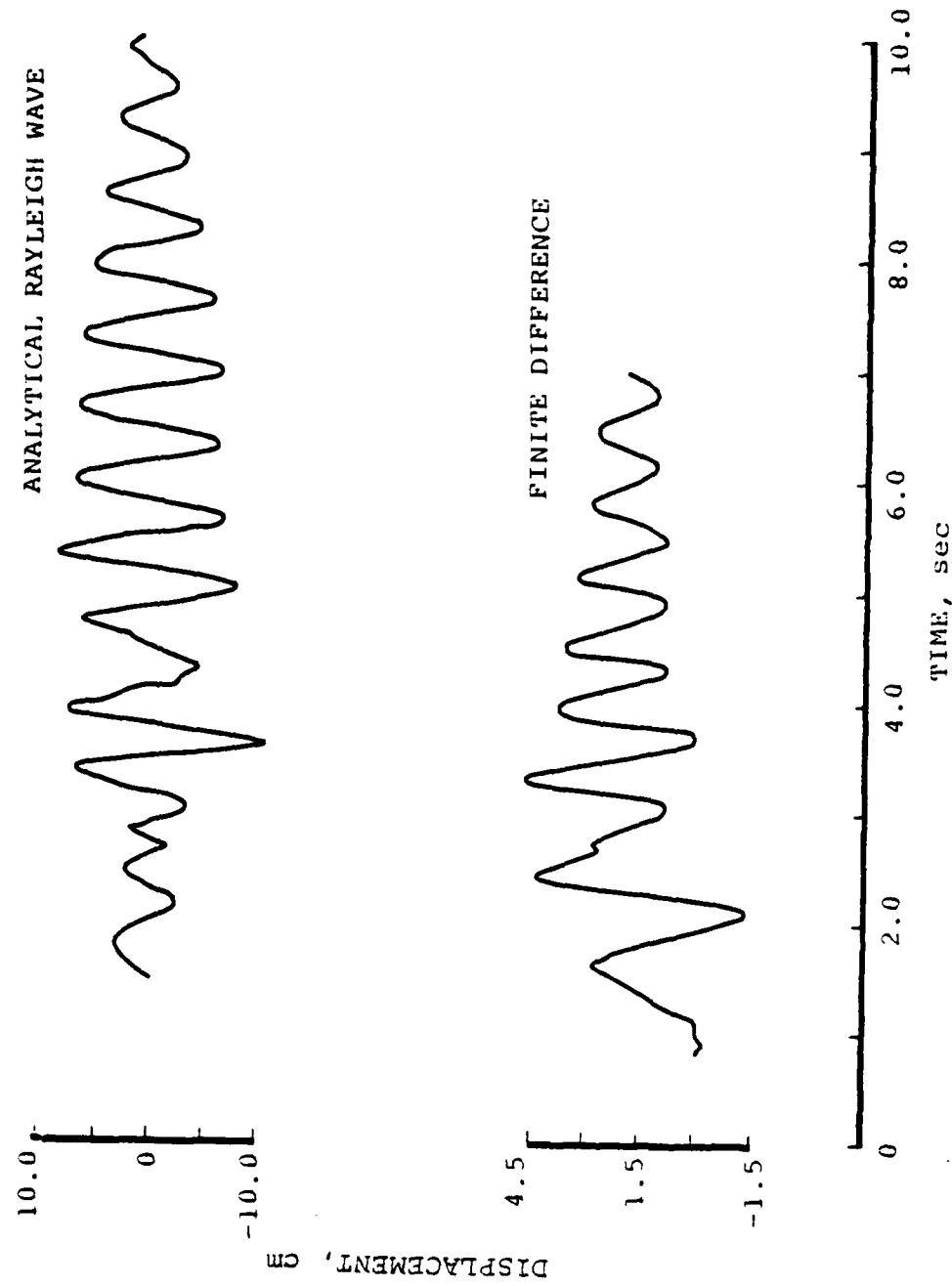


Figure 18. Comparison of analytical Rayleigh wave and finite difference displacement time histories, Case 1, vertical component,  $W = 1 \text{ Mt}$ ,  $R = 1800 \text{ m}$ .

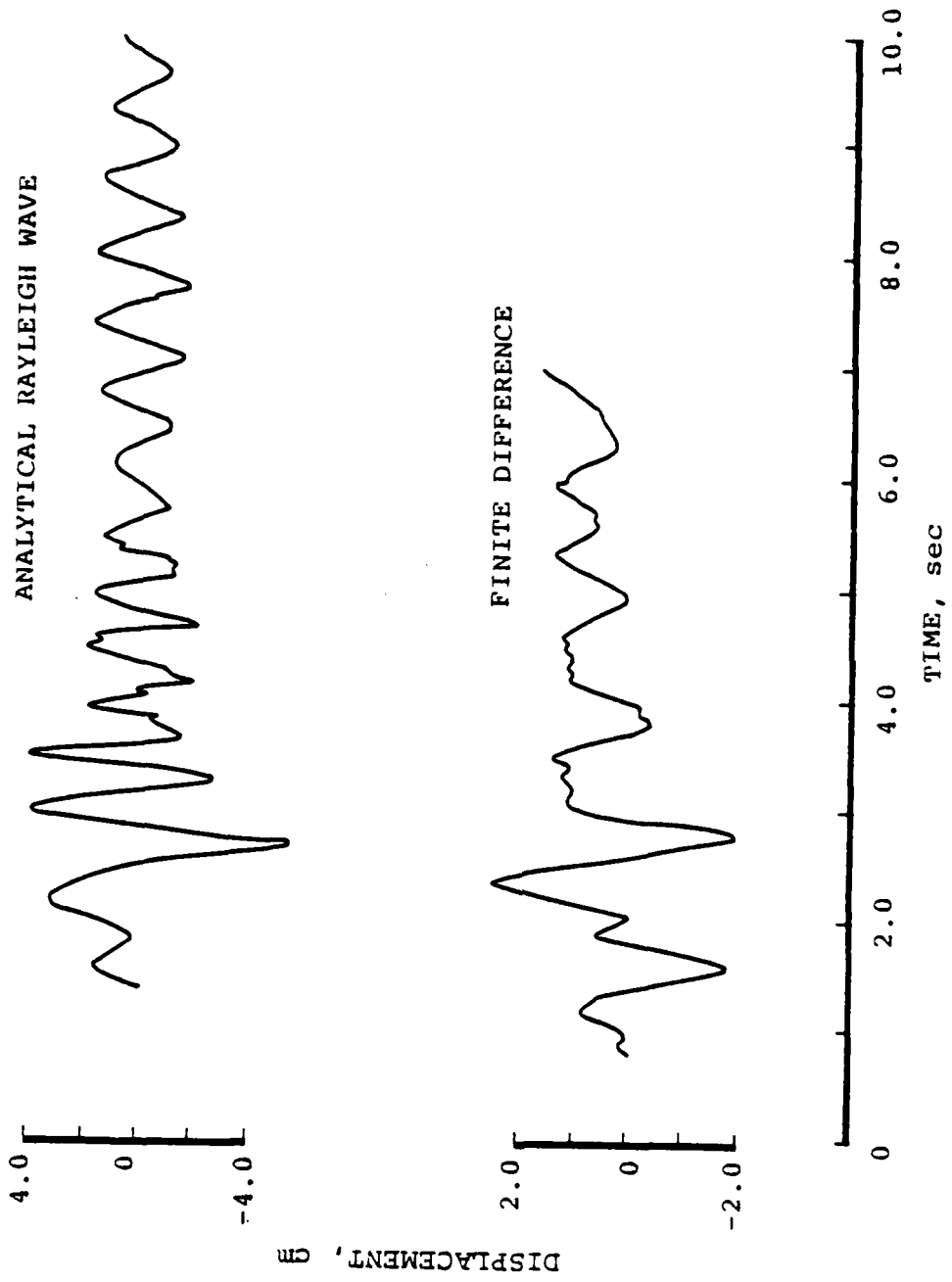


Figure 19. Comparison of analytical Rayleigh wave and finite difference displacement time histories, Case 1, radial component,  $W = 1 \text{ Mt}$ ,  $R = 1800 \text{ m}$ .

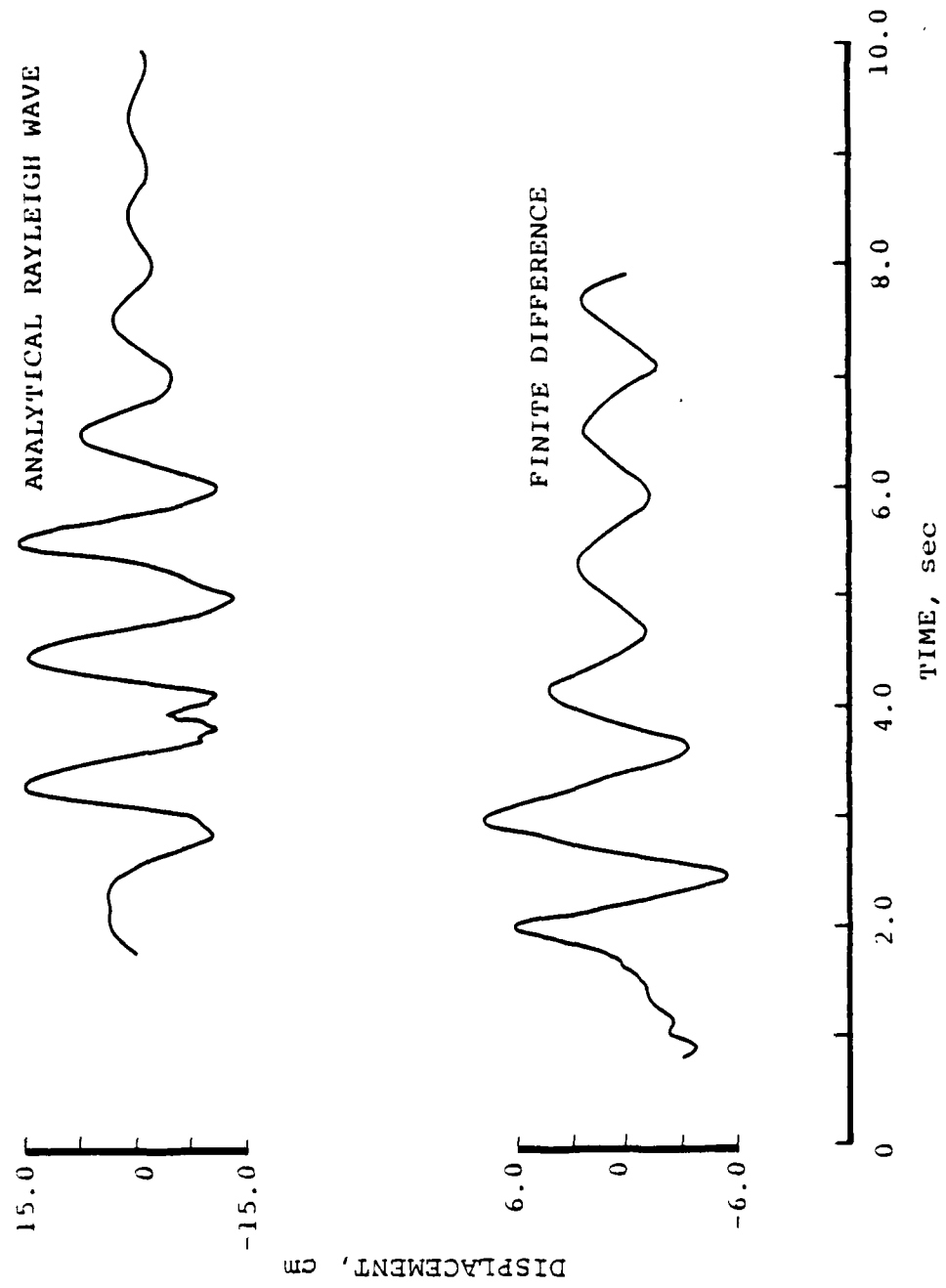


Figure 20. Comparison of analytical Rayleigh wave and finite difference displacement time histories, Case 2, vertical component,  $W = 1 \text{ Mt}$ ,  $R = 1800 \text{ m}$ .

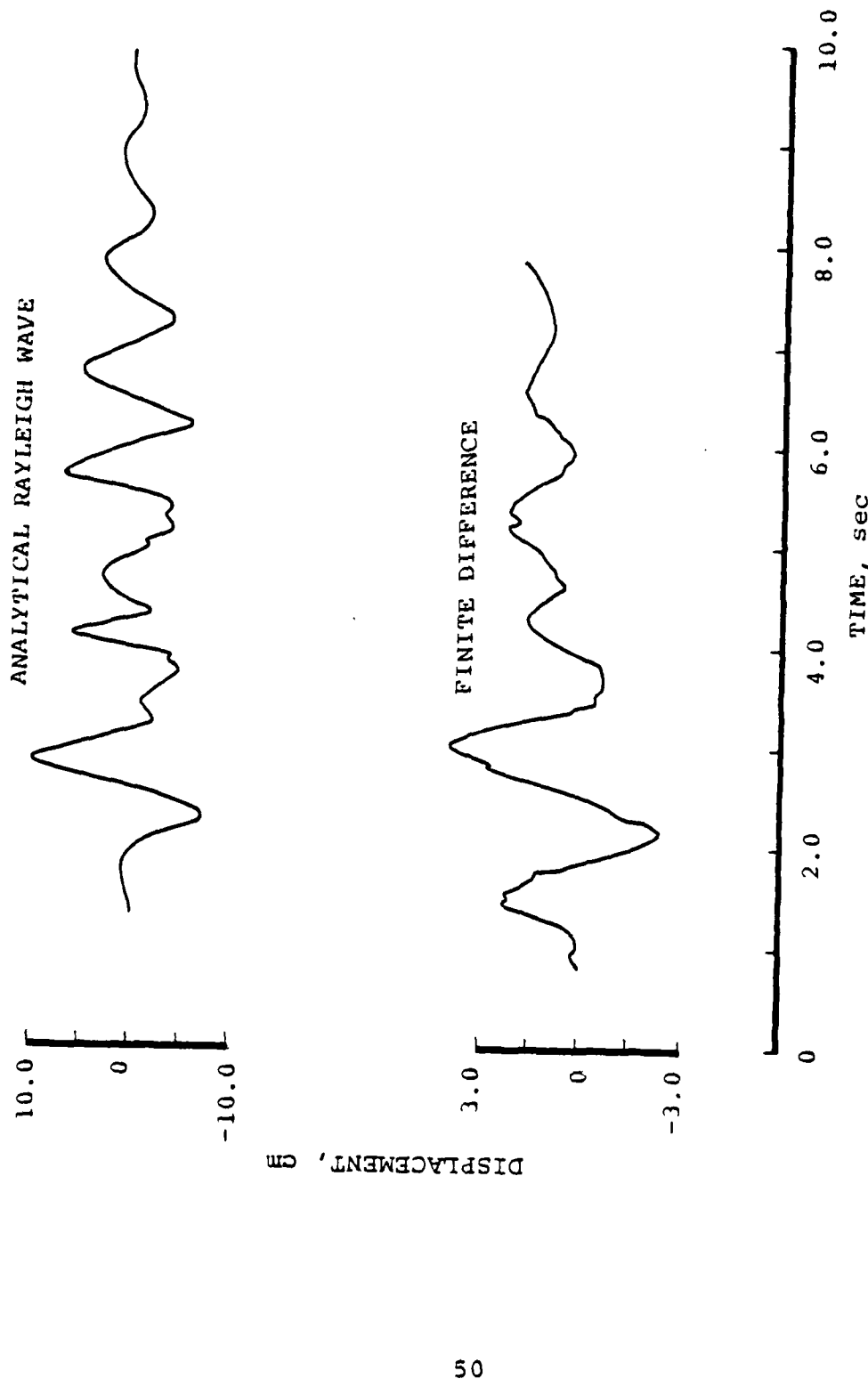
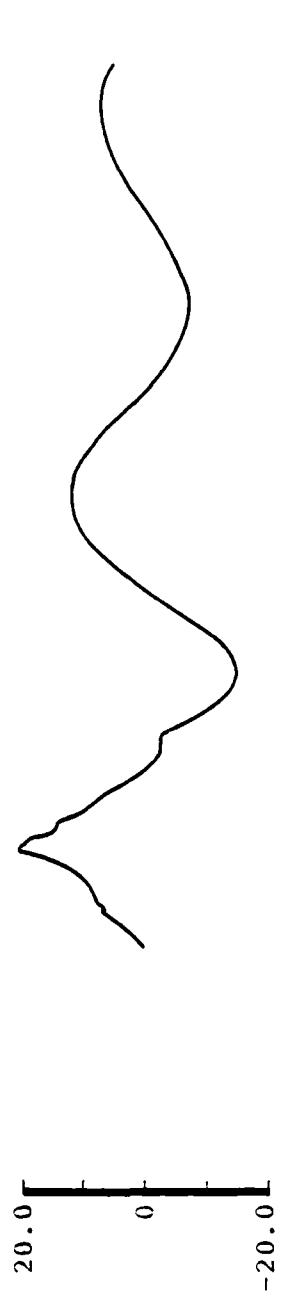


Figure 21. Comparison of analytical Rayleigh wave and finite difference displacement time histories, Case 2, radial component,  $W = 1 \text{ Mt}$ ,  $R = 1800 \text{ m}$ .

ANALYTICAL RAYLEIGH WAVE



51 FINITE DIFFERENCE

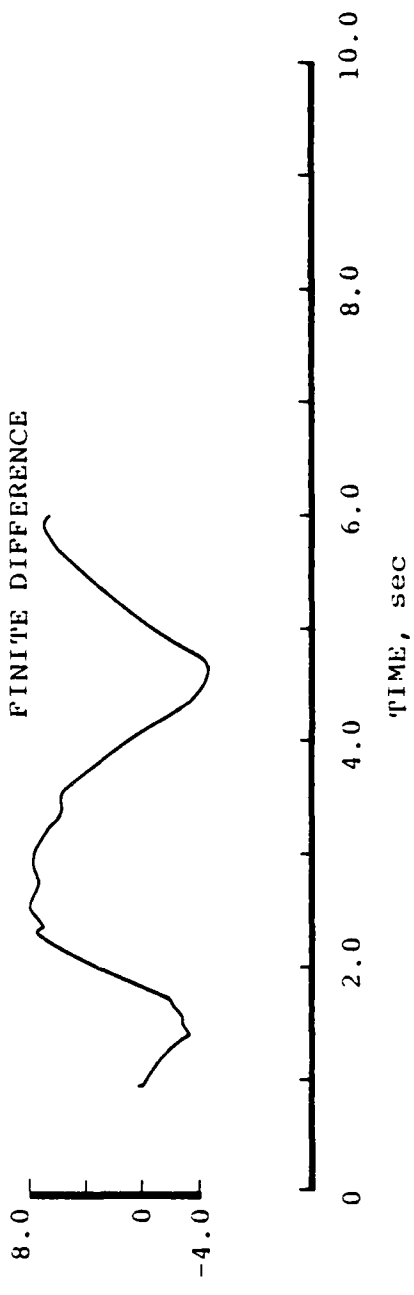


Figure 22. Comparison of analytical Rayleigh wave and finite difference displacement time histories, Case 3, vertical component,  $W = 1 \text{ Mt}$ ,  $R = 1800 \text{ m}$ .

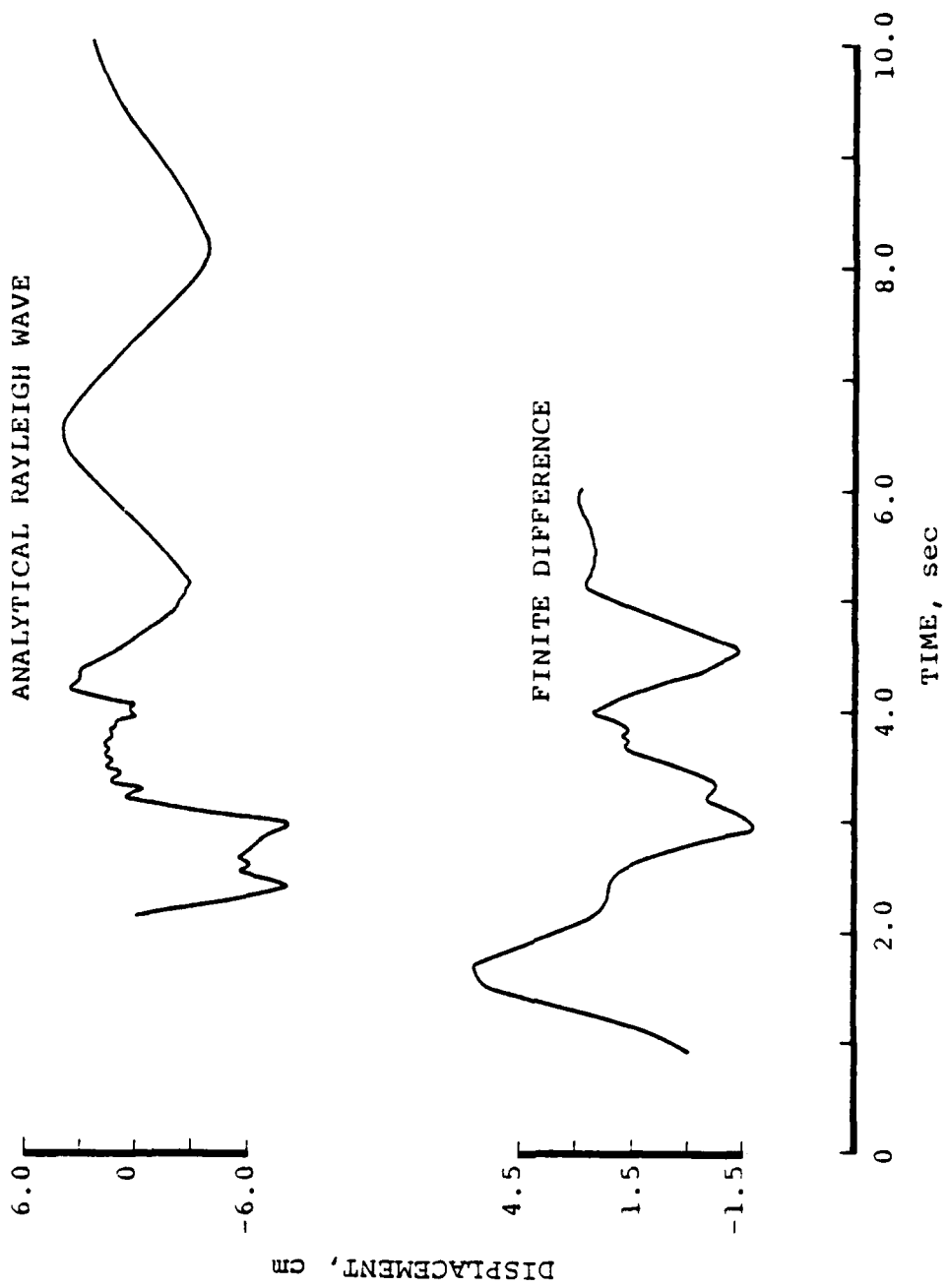


Figure 23. Comparison of analytical Rayleigh wave and finite difference displacement histories, Case 3, radial component,  $W = 1 \text{ Mt}$ ,  $R = 1800 \text{ m}$ .

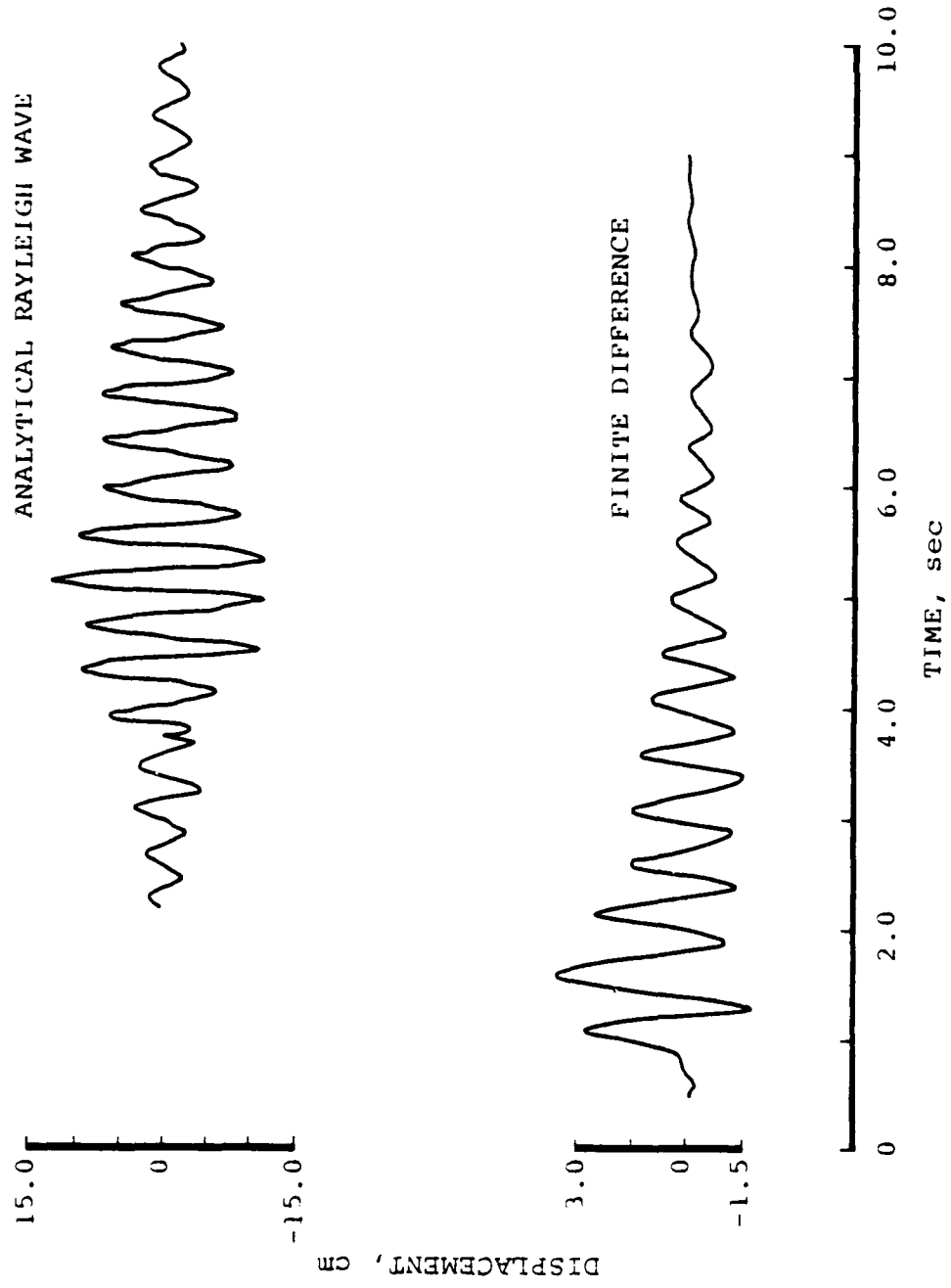


Figure 24. Comparison of analytical Rayleigh wave and finite difference displacement time histories, Case 4, vertical component,  $W = 1 \text{ Mt}$ ,  $R = 1800 \text{ m}$ .

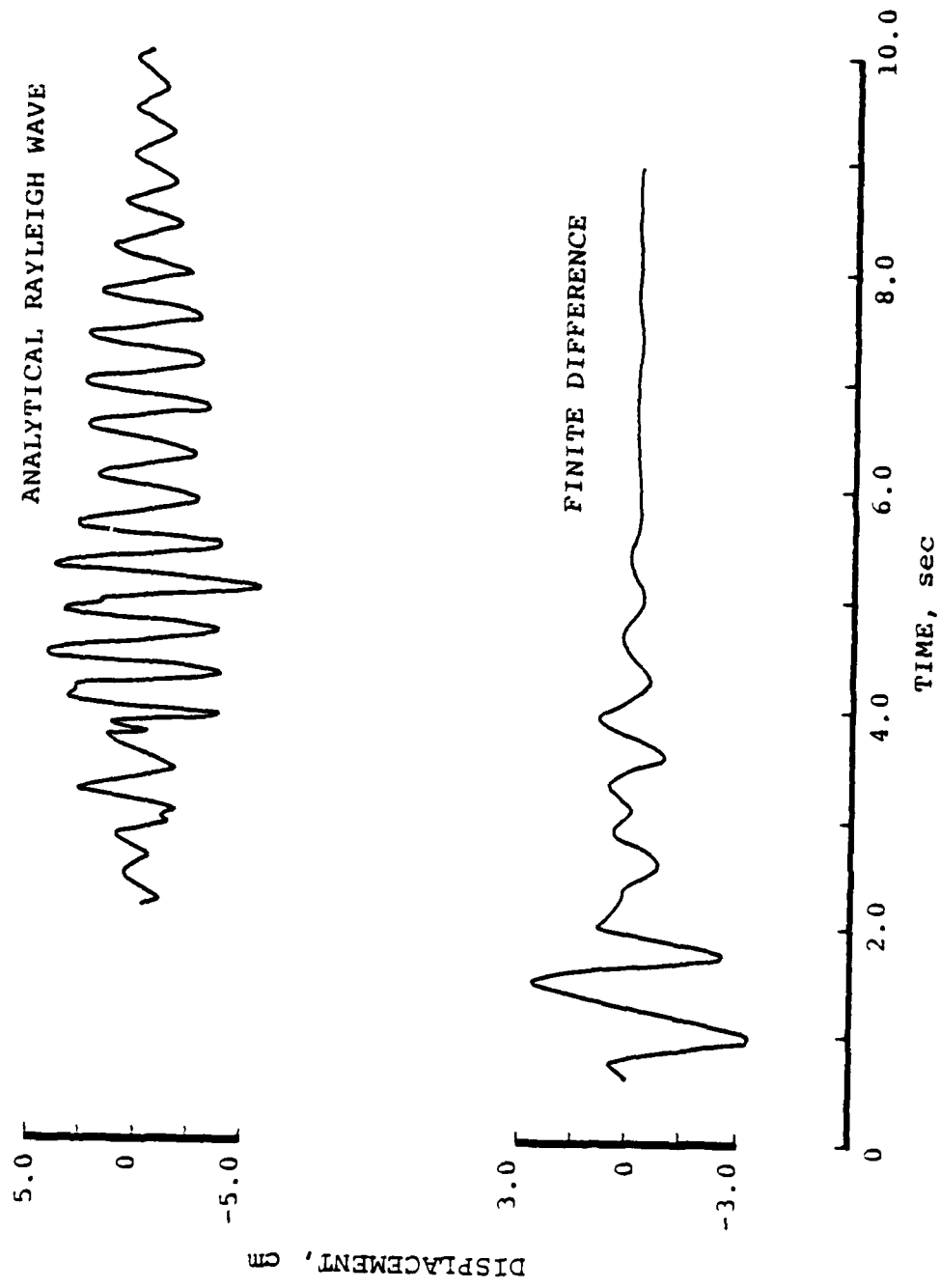


Figure 25. Comparison of analytical Rayleigh wave and finite difference displacement time histories, Case 4, radial component,  $W = 1 \text{ Mt}$ ,  $R = 1800 \text{ m}$ .

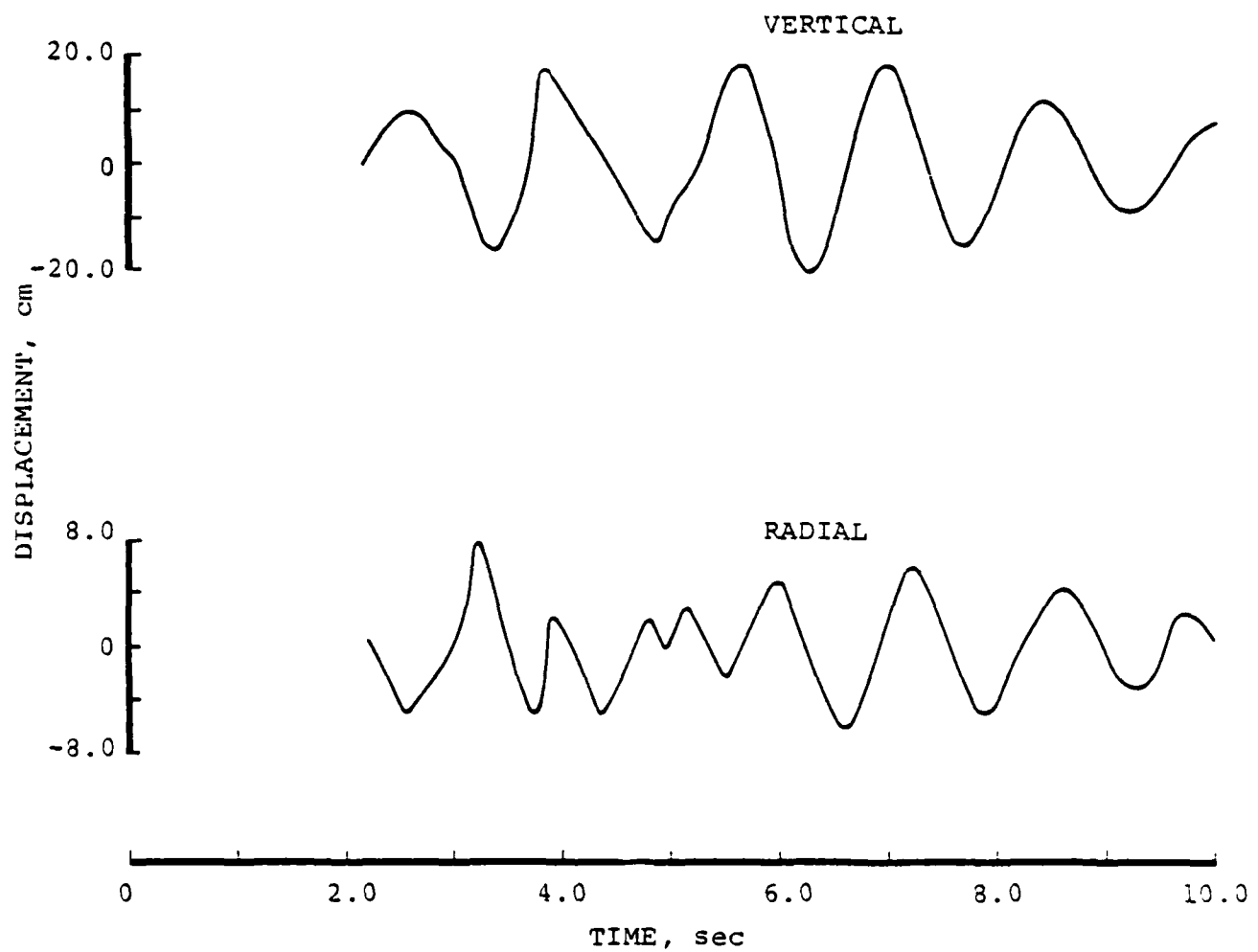


Figure 26. Analytical Rayleigh wave displacement time histories  
Case 5,  $W = 1 \text{ MT}$ ,  $R = 1800 \text{ m}$ .

analytic Rayleigh wave calculations were most nearly the same in this case. Thus, although the dominant frequencies are still comparable, the general character of the motions is quite different. This may be an indication that the higher mode Rayleigh waves are making a significant contribution in this case, although preliminary theoretical calculations which include the contributions from the first higher mode do not seem to support this interpretation.

In any case, it can be seen that the predominant frequencies of the Rayleigh wave and finite difference solutions are in good agreement with each other and also with the site response corner frequencies shown in Figures 15 through 17. Thus, it can be concluded that the corner frequencies of the Rayleigh wave source functions corresponding to a one megaton surface burst lie below the site response corner frequencies in all of these cases. In fact, parametric calculations indicate that this is true for all yields above a few hundred kilotons. That is, for yields above this level the predominant Rayleigh wave frequency can be expected to be independent of yield and the amplitude level is expected to be proportional to  $W^{\frac{1}{3}}$  at a fixed range for these sites. This is illustrated in Figure 27 which compares the fundamental mode, vertical component Rayleigh wave displacements at a fixed range of 1800 m computed for Case 2 assuming modified air-blast loadings corresponding to 1 and 30 megaton surface bursts. It can be seen that the dominant frequency of the motion remains constant and that the amplitude level increases as the cube root of the ratio of the yields, as predicted.

In summary, available evidence suggests that the dominant frequency and relative amplitude level of the low-frequency ground motions to be expected at a variety of prototype MX sites from megaton level surface bursts can be

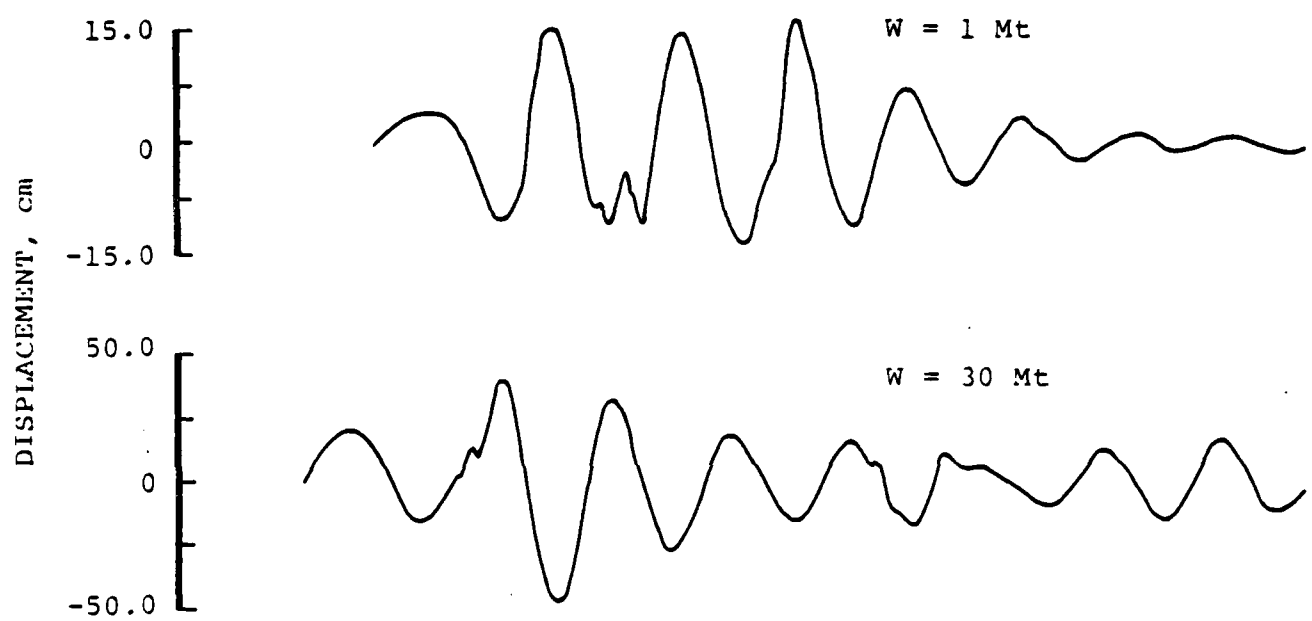


Figure 27. Comparison of vertical component Rayleigh wave displacement time histories for yields of 1 and 30 Mt, Case 2,  $R = 1800$  m.

reliably estimated using elastic Rayleigh wave theory. In particular, the dominant frequency can be approximated as  $\bar{\beta}/2\bar{H}$ , where  $\bar{H}$  denotes the total soil thickness at the site and  $\bar{\beta}$  is the average shear wave velocity of the soil column. For yields above a few hundred kilotons, this dominant frequency will be independent of yield and the amplitude of the Rayleigh wave ground motion at a fixed range will be proportional to  $W^{1/3}$ .

The results of the above analysis suggest a possible simplified means of ranking candidate MX sites according to the expected severity of the low-frequency ground motion environment. Thus, for each site under consideration,  $S(f_c)$  can be approximated from (2-27) for the yield of interest (for  $W$  greater than about 200 kt) and multiplied times  $A_R(f_c)$  to obtain an estimate of the relative displacement amplitude level to be expected at the predominant Rayleigh wave frequency of the site (i.e.  $f_c$ ). Moreover, since the computed time histories are approximately sinusoidal, the relative displacement amplitude levels could then be converted to estimates of the corresponding relative particle velocity amplitude levels by simply multiplying by the quantity  $2\pi f_c$ .

## 2.5 MULTIBURST SURFACE WAVE EFFECTS ON MISERS BLUFF II-2

The Misers Bluff II (MBII) experiments were a series of two high explosive surface burst tests conducted by the Defense Nuclear Agency in a small scale valley structure at Planet Ranch in Arizona. The second test conducted at this site (MBII-2) consisted of an array of six simultaneous 120 ton ANFO explosions deployed in a hexagonal pattern. Figure 28 shows a schematic drawing of the source array together with some representative receiver locations as well as a plane layered approximation to the subsurface geology at the site. It can be seen that the site is characterized by a 70 m thick

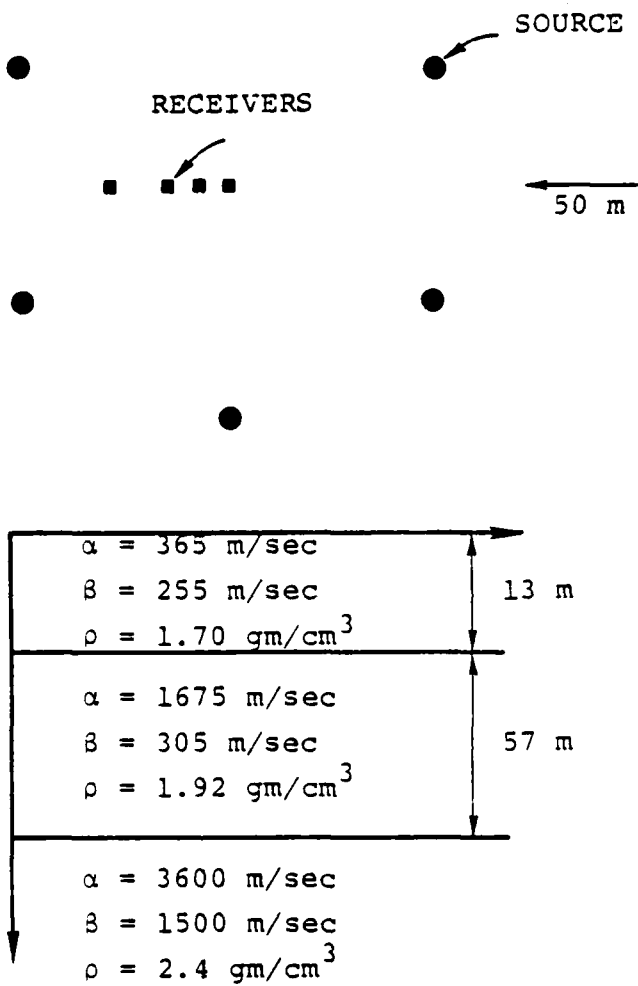


Figure 28. Source/receiver pattern and subsurface geologic profile for the Misers Bluff II-2 experiment.

layer of alluvium (saturated below the water table at a depth of 13 m) overlying basalt. An unusual feature of the ground motion recordings taken interior to this source array is the presence of a large burst of energy arriving at the center of the array about 800 milliseconds after detonation time. This arrival is illustrated in Figure 29 which shows the observed vertical displacement records measured interior to the source array along a common azimuth. It can be seen that the maximum peak-to-peak displacement at the center of the source array (i.e.  $r = 0$ ) is about five times larger than that observed at the station located midway between the origin and the source radius (i.e.  $r = 50$  m). Analysis of the complete set of data recorded interior to the source array indicates that the diagnostic characteristics of this signal are: (i) that it is propagating inward toward the center of the array with a phase velocity of around 500 m/sec, (ii) that the amplitude of the vertical component of the motion increases to a maximum at the center of the array, as opposed to the amplitude of the horizontal component of motion which reaches a minimum at that point and (iii) that the signal is approximately axisymmetric. Since no such arrival was observed on the companion single burst experiment conducted at this site (MBII-1) and since linear superposition of the motions from the six explosions is unable to explain the observed spatial variation of the displacement peaks, it has been concluded that this arrival was generated by the nonlinear interaction between the multiple sources. Moreover, the observed phase velocity and character of the signal suggest that it may be a surface wave and consequently the arrival has been modeled as a Rayleigh wave converging on the origin. Now, despite the fact that the airblast loading is known to be very complicated in this case, the symmetric nature of the late-time arrival of interest here suggests that its source may be axisymmetric to

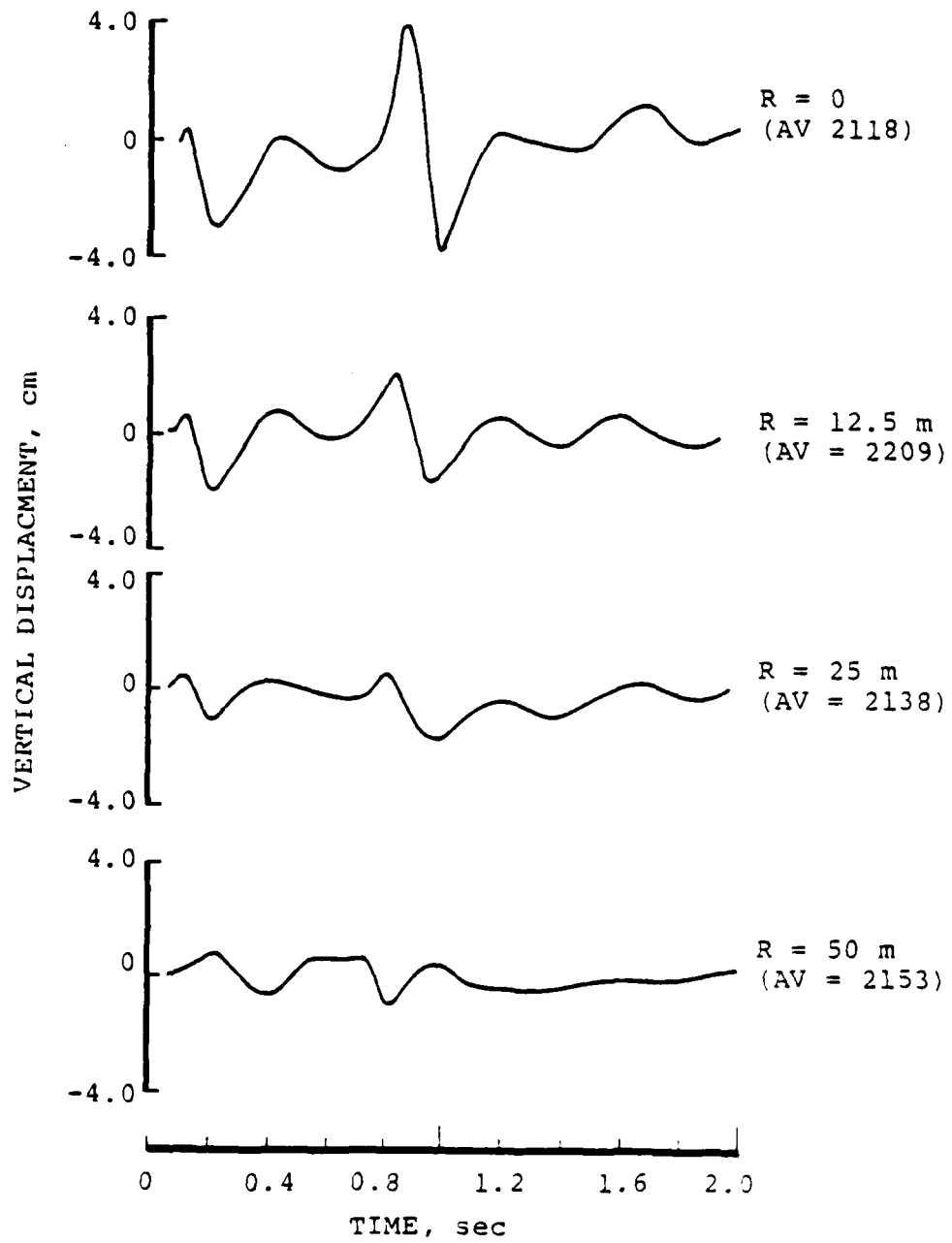


Figure 29. Observed vertical displacement inside source array, MBII-2.

a first order of approximation. Consequently, the MBII-2 observations have been theoretically simulated by loading a surface ring of the geologic model shown in Figure 28 with a simple, impulsive (i.e.,  $\alpha = 10 \text{ sec}^{-1}$ ) overpressure approximation of the form

$$p(r, t) = p_0 e^{-\alpha(t-t_0)} H(t-t_0) \quad (2-37)$$

where  $t_0$  is a free parameter defining the time required for the interacting shock waves from the six events to form an approximately axisymmetric loading condition. In this case, the source integral of Equation (2-11) has the form

$$\tilde{S}(\omega) = \frac{p_0 e^{-i\omega t_0}}{\alpha + i\omega} \int_{r_1}^{r_2} H_0^{(2)}(kr') r' dr' \quad (2-38)$$

which can be integrated analytically to obtain

$$\begin{aligned} \tilde{S}(\omega) &= \frac{p_0 e^{-i\omega t_0}}{(\alpha + i\omega) k} \left[ r_2 J_1(kr_2) - r_1 J_1(kr_1) \right] \\ &- \frac{i p_0 e^{-i\omega t_0}}{(\alpha + i\omega) k} \left[ r_2 Y_1(kr_2) - r_1 Y_1(kr_1) \right]. \quad (2-39) \end{aligned}$$

The converging fundamental mode Rayleigh waves produced by applying three different ring loads centered on the source radius (100 m) to the geologic model of Figure 28 are shown in Figures 30 through 32. It can be seen that the theoretical prediction for the case shown in Figure 32 (i.e.,  $r_1 = 90 \text{ m}$ ,  $r_2 = 110 \text{ m}$ ,  $t_0 = 0.4 \text{ sec}$ ) fits the observations very well. In particular, the phase velocity, dominant frequency and surface wave waveforms are nearly exactly duplicated while the predicted relative amplitude levels are within the scatter in the experimental data.

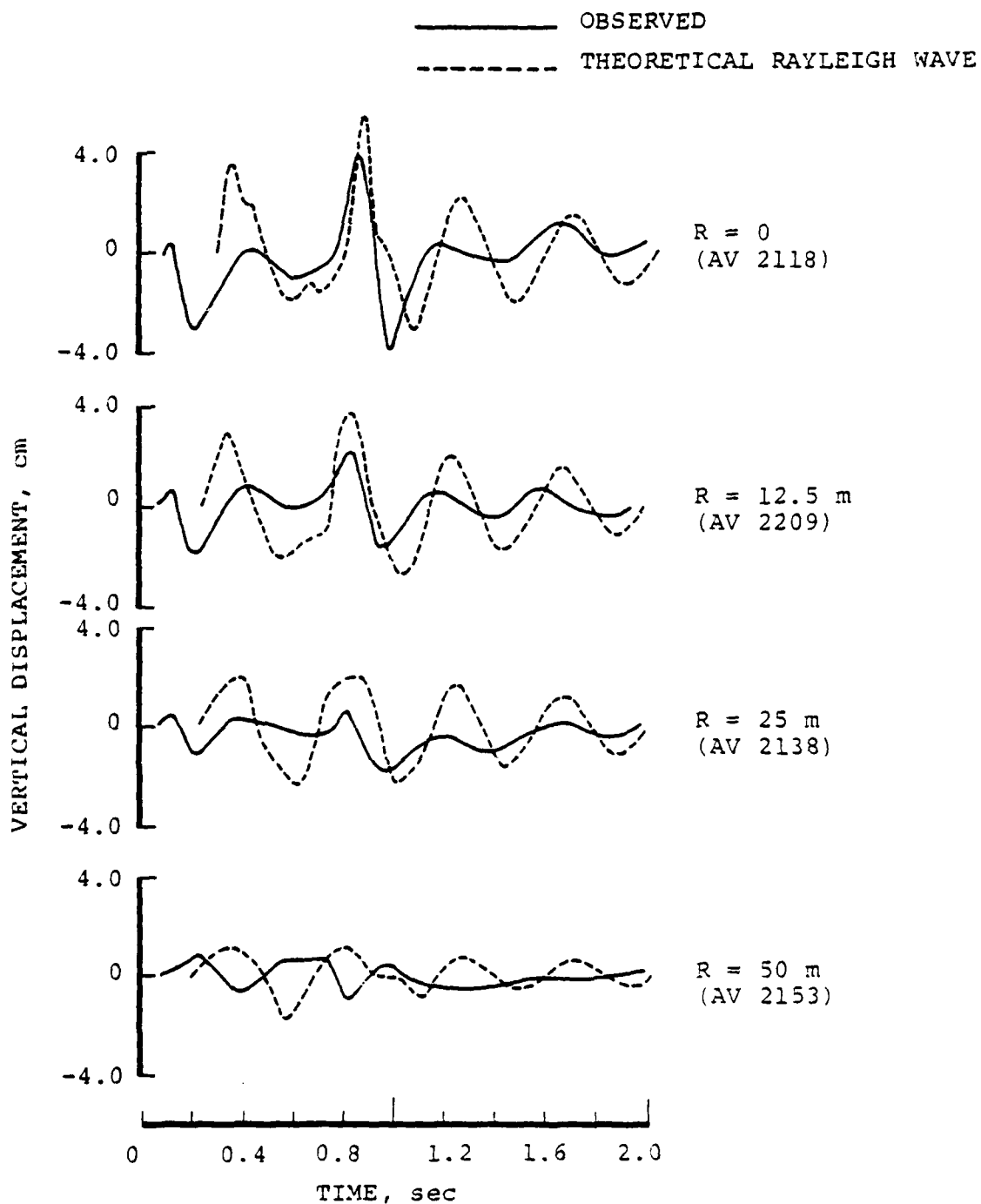


Figure 30. Comparison of observed MBII-2 vertical displacement data with theoretical converging Rayleigh wave solution; distance measured from center of source array ( $t_0 = 0$ ,  $r_1 = 50$  m,  $r_2 = 150$  m).

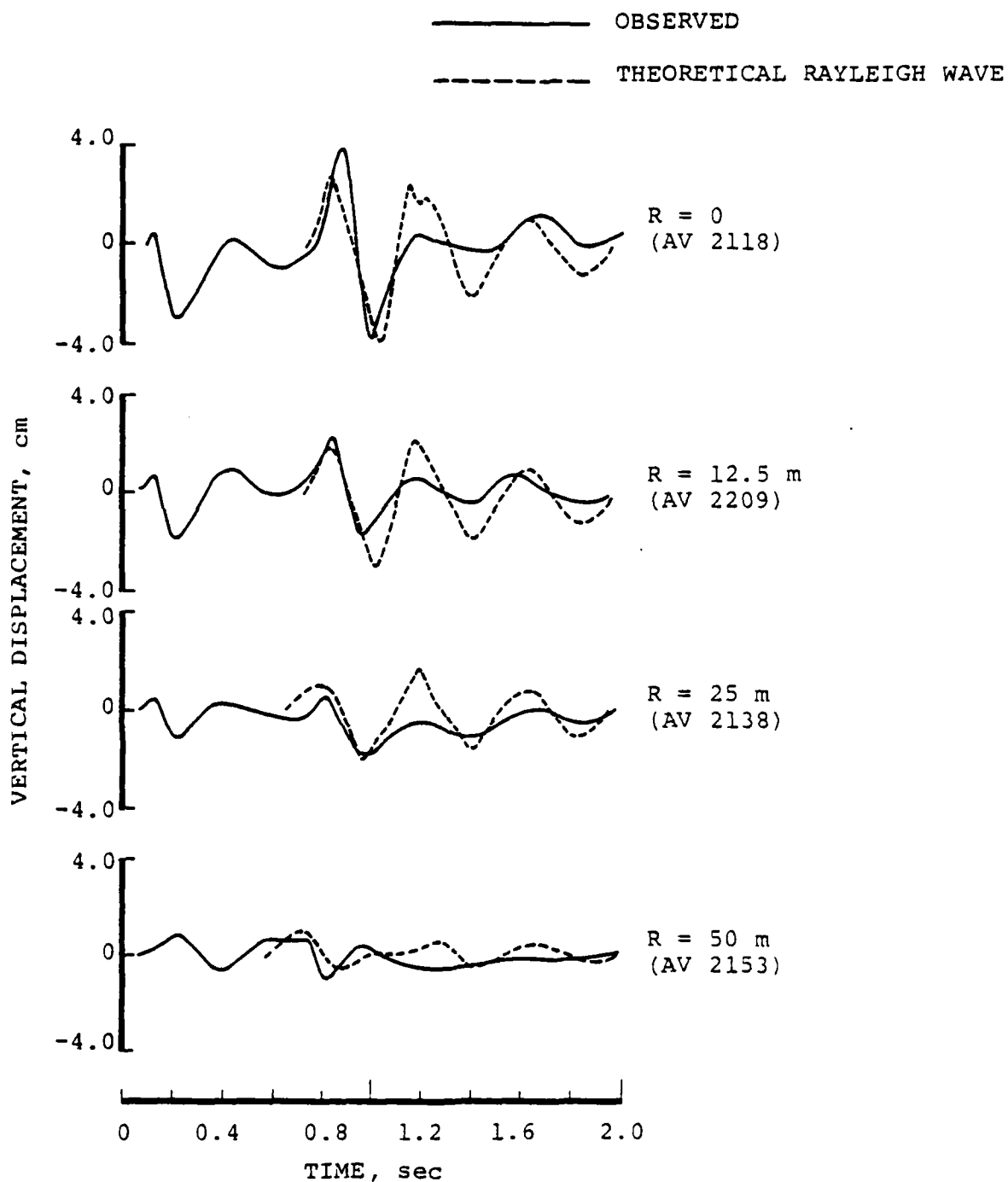


Figure 31. Comparison of observed MBII-2 vertical displacement data with theoretical converging Rayleigh wave solution; distance measured from center of source array ( $t_0 = 0.4$  seconds,  $r_1 = 75$  m,  $r_2 = 125$  m).

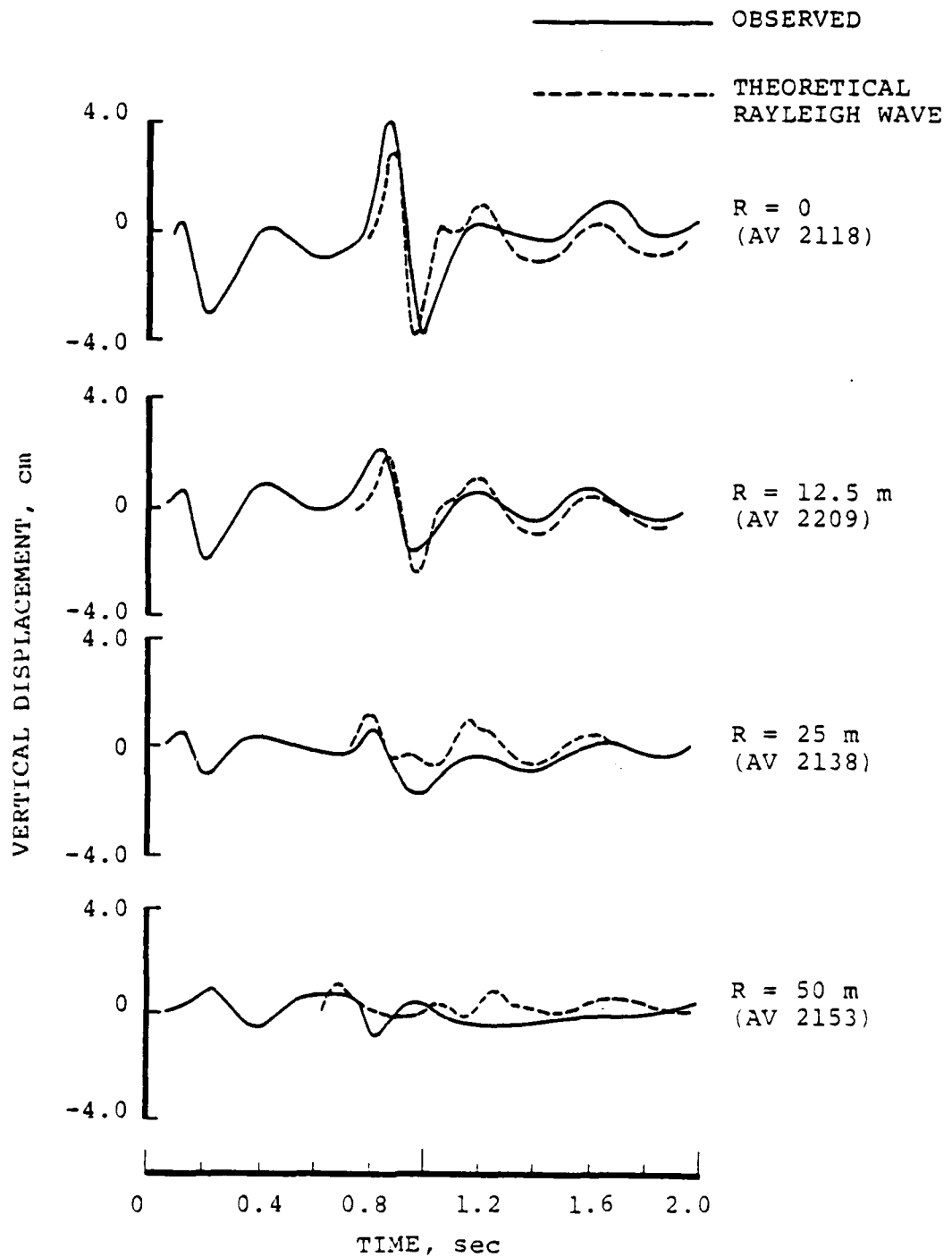


Figure 32. Comparison of observed MBII-2 vertical displacement data with theoretical converging Rayleigh wave solution; distance measured from center of source array ( $t_0 = 0.4$  seconds,  $r_1 = 90 \text{ m}$ ,  $r_2 = 110 \text{ m}$ ).

These results provide strong evidence that the 800 millisecond arrival observed on MBII-2 is a converging Rayleigh wave produced by an axisymmetric surface load acting over a relatively small area centered on the source locations. The question still remains, however, of how this axisymmetric loading is set up by the interacting shock waves from the six MBII-2 sources. For example, in order to match the observed arrival times in Figure 32, it was necessary to assume a value of  $t_0 = 0.4$  seconds. In view of the fact that the air-blast reaches the center of the source array in less than 0.1 seconds, this is a very late time phenomena. It is interesting to note that a major spall closure did occur at about 0.4 seconds on the companion single explosive event conducted at this site (MBII-1) suggesting that the interacting spall closures from the multiple explosions may be the source of this arrival. However, more detailed analyses of the measured MBII-2 near-source data will be required in order to provide a definitive test of this hypothesis.

In summary, multiburst loadings resulting from at least some charge spacings can produce long-period surface wave motions which seem to have no counterparts on single burst recordings. This suggests that the possible influence of such phenomena on the ground motion environment for MX should be carefully evaluated on a case-by-case basis.

### III. VALLEY REVERBERATION

#### 3.1 INTRODUCTION

It has been recognized from the early planning stages that the geologic environment of potential MX sites (i.e., alluvium-filled valleys) is quite different from that encountered in the Minuteman siting. As a result, questions have been raised concerning the issue of whether the ground motion environment in the valley produced by near-surface explosions will be significantly altered, and in particular enhanced, as a result of the presence of the valley boundaries. For example, Figure 33 shows a schematic geologic cross section of a typical Basin and Range valley. It can be seen that at the edges of the valley the alluvium is terminated by boundary faults, giving rise to a significant seismic impedance contrast at the steeply-dipping alluvium/rock interface. Thus, it can be expected that at least some of the outgoing seismic energy induced by a surface explosion will be reflected back from the valley boundaries (particularly for the horizontally propagating surface waves) and contribute to the ground motion experienced at a target point in the valley. This is in contrast to the situation at the Minuteman sites where the subsurface geologic structure is more nearly laterally homogeneous and, consequently, contributions to the ground motion due to reflections from vertical boundaries would be expected to be negligible.

An example of the effects of valley boundaries is provided by Figure 34 where the radial component seismograms recorded at a station in the Las Vegas Valley (SE-6) and at a station outside the valley (PAH) at about the same distance from the same Nevada Test Site (NTS) explosion are compared. It can be seen that the upper trace which was recorded

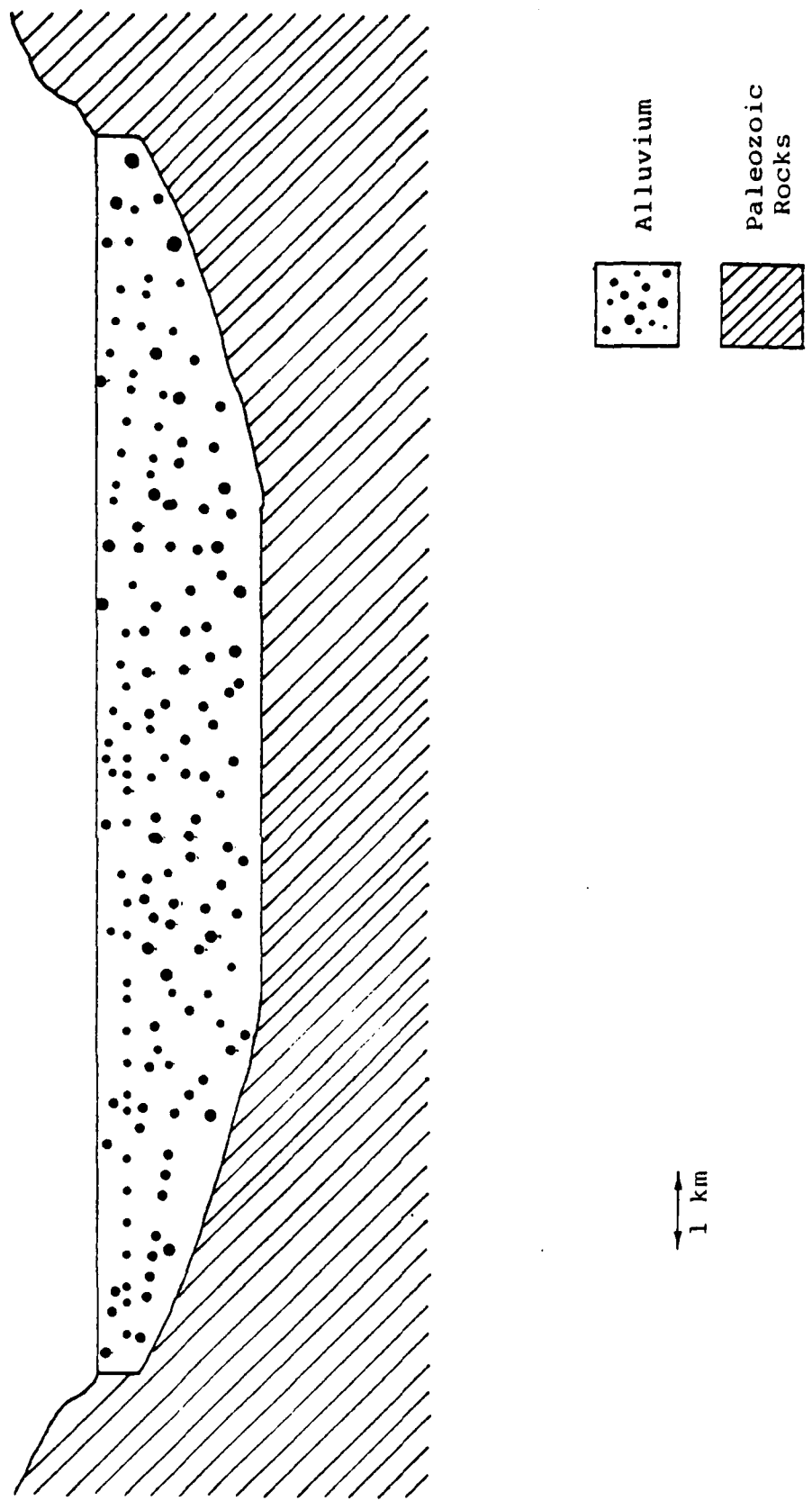


Figure 33. Schematic geologic cross section for a Basin and Range valley structure.

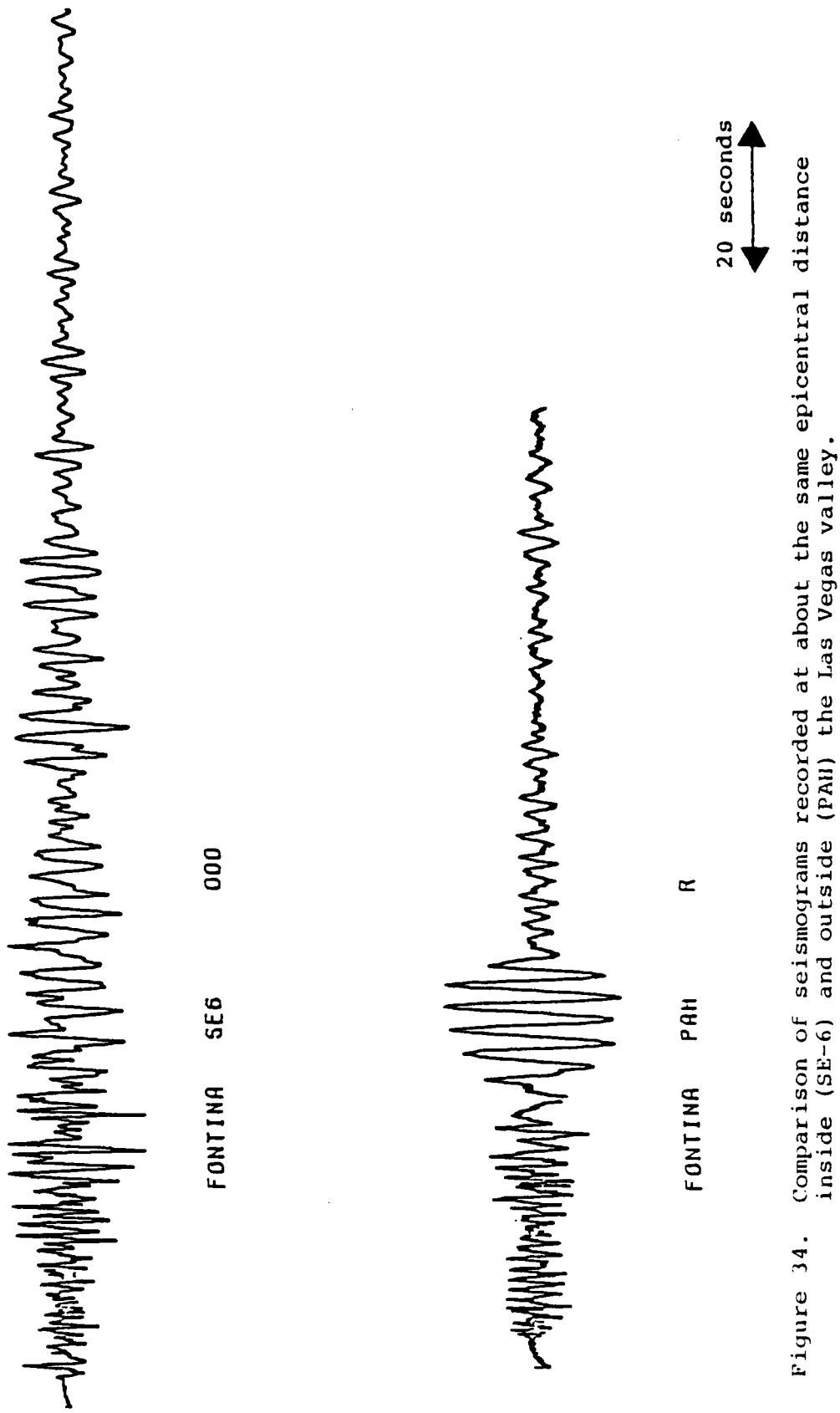


Figure 34. Comparison of seismograms recorded at about the same epicentral distance inside (SE-6) and outside (PAH) the Las Vegas valley.

within the valley is much more complex and of significantly longer duration than the lower trace which was recorded outside the valley. The inference is that multipathing (i.e., multiple reflections) of energy along the valley boundaries is the source of this dramatic increase in complexity and duration.

During the past several years a number of specific experimental and theoretical investigations have been conducted with the objective of defining the effect of valley boundaries on the ground motion environment to be expected at target points inside the valley. The ultimate goal of these studies is to develop a better understanding of the phenomenology so that an approximate synthesis model can be formulated which can be used in predicting the environment in the MX valleys of interest.

This chapter, first, summarizes the results of prior investigations which suggest that alterations in the ground motion can be anticipated in such environments and, then, focuses on analyses of ground motion measurements from the Misers Bluff II (MB-II) explosions and their implications with regard to the effects of valley boundaries.

### 3.2 RESULTS FROM PREVIOUS STUDIES

Prior investigations of ground motion near the boundaries of alluvial valleys have included both observational and theoretical studies; we will describe here the pertinent results from both types of study. Experimental studies to date have centered on the analysis of ground motion data recorded in valleys from NTS underground explosions as well as data recorded on specially designed arrays of seismometers deployed to monitor the Misers Bluff II (MB-II) explosions. The MB-II studies will be discussed more completely in Section 3.3 below. Although valuable information has been obtained from both these data sources, it should be noted that

neither are directly applicable to the definition of the MX environment. That is, the NTS data were measured from contained underground explosions while the MB-II data were measured from small-scale surface HE detonations conducted in a "miniature MX valley". Therefore, the primary goal of our consideration of these data has been to develop a better understanding of the phenomenology so that extrapolations can be made to the full-scale environment of interest.

The first data bearing on this problem was alluded to earlier and consisted of ground motion recordings made in Las Vegas from contained underground explosions located on NTS some 150 km away and outside of the Las Vegas Valley structure. The Las Vegas Valley is a prominent northwest-trending topographic depression situated in the southern part of the Basin and Range Province. The city of Las Vegas is located in the southern portion of this elongated valley in the center of a rectangular basin which is about 30 km wide and 40 km long. The city has been well instrumented to record ground motions from underground nuclear tests conducted at NTS. Figure 35 shows the locations of a selected subset of these stations and Figure 36 shows the radial component velocity time histories recorded at these stations from the CARPETBAG explosion. These records are typical and show pronounced evidence of interference at late arrival times consistent with what would be expected from the simultaneous arrival of energy from several different directions (Murphy and Hewlett, 1975).

In order to determine the direction of approach and relative amplitude of these secondary arrivals, the ground motion time histories of Figure 36 were velocity filtered using the beam-steer process which is routinely used in the detection and analysis of signals recorded at large seismic arrays such as the Montana Large Aperture Seismic Array (LASA).

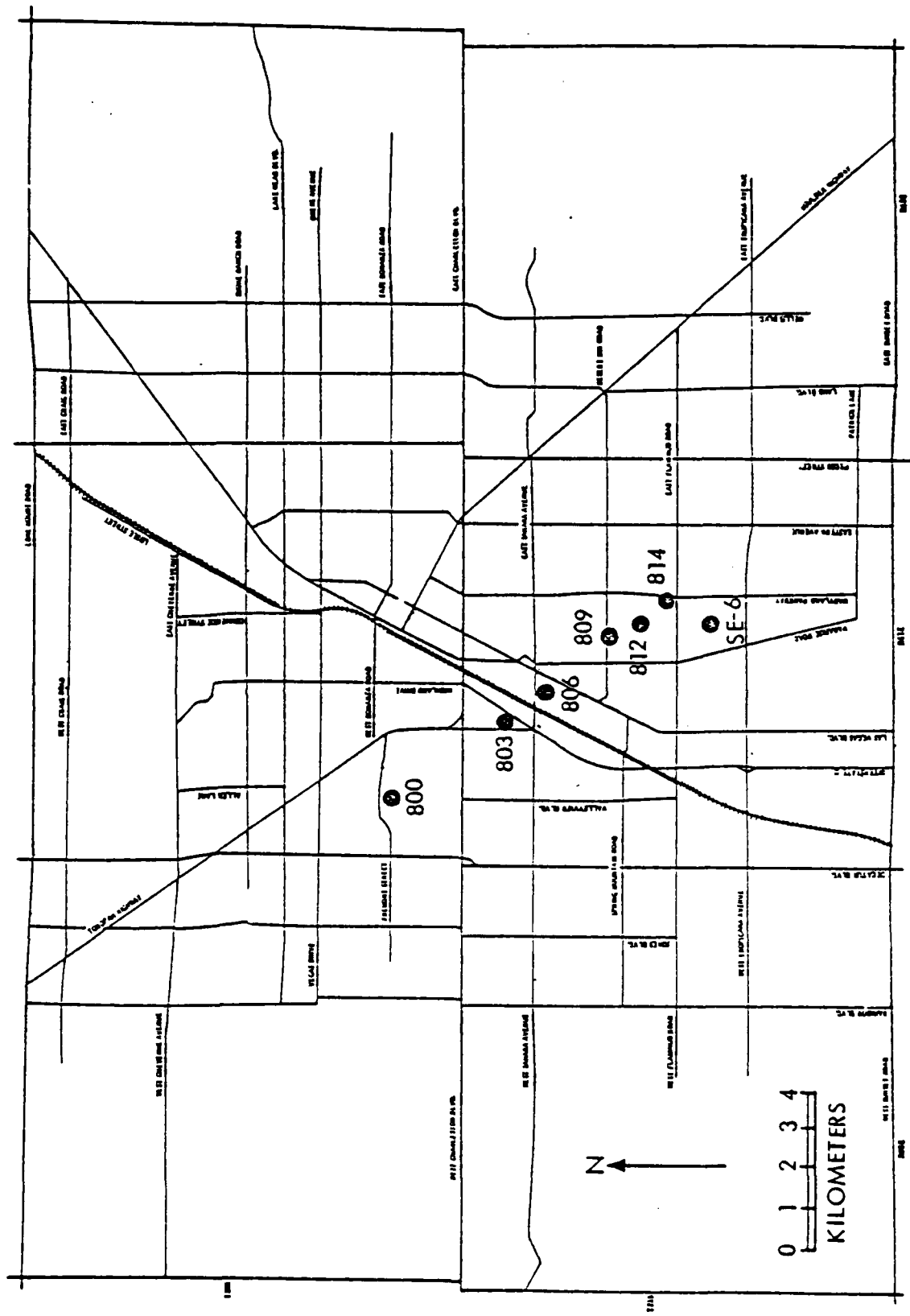


Figure 35. Station location map for Las Vegas.

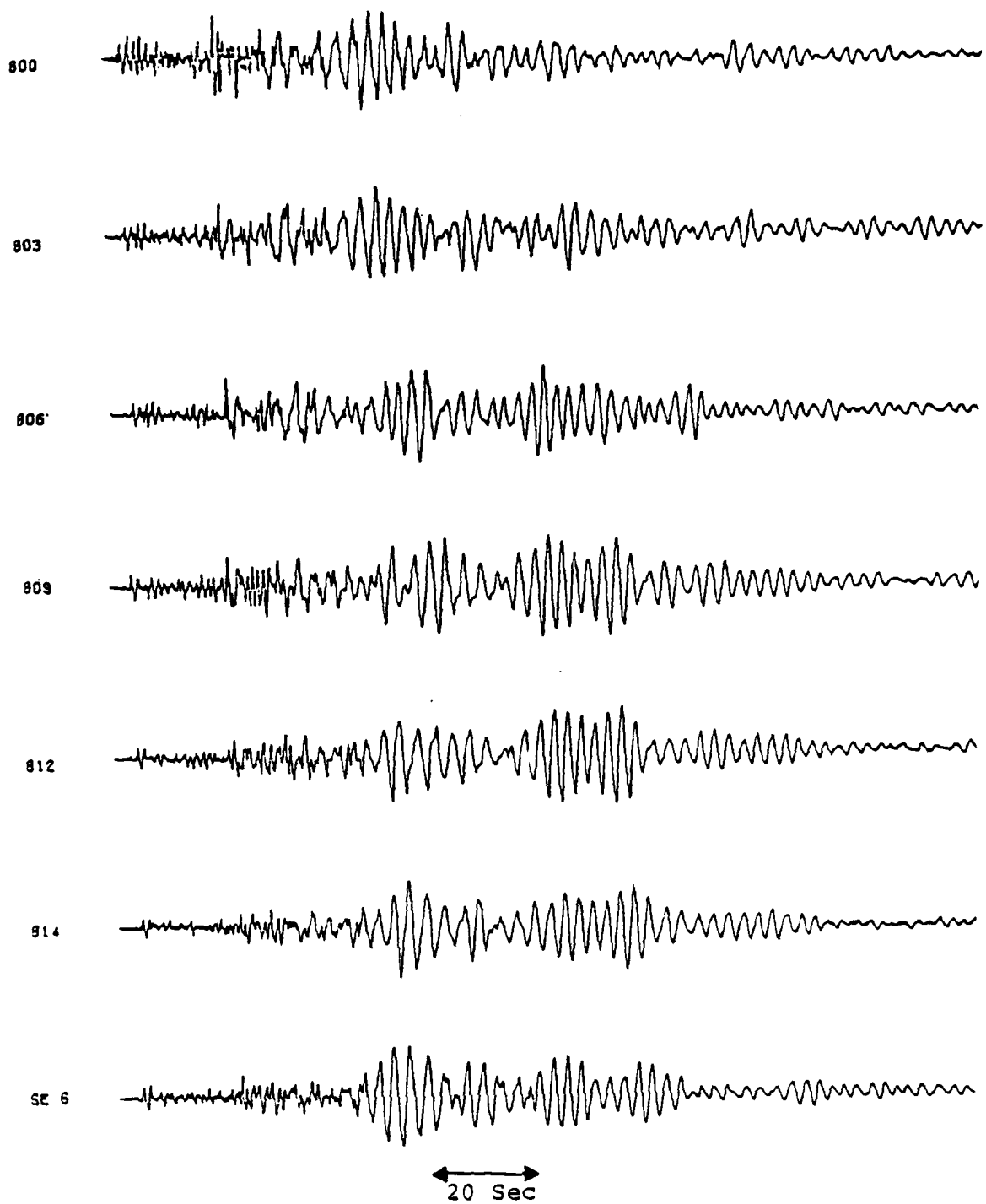


Figure 36. Radial component record section for the CARPET-BAG event.

The concept underlying this process is quite simple. Suppose an arrival of interest (e.g., a P wave) is traveling across the array from some unknown direction with phase velocity  $c$ . Now, for each possible direction of approach,  $\theta$ , there will be a unique set of delays,  $\Delta t_i(\theta)$  describing the propagation across the station locations at velocity  $c$ . Thus, if the waveforms recorded at each station are time-shifted by an amount  $\Delta t_i(\theta)$  and added together, then energy arriving from direction  $\theta$  with velocity  $c$  will add coherently while, in general, energy traveling in other directions or at other velocities will add incoherently and tend to cancel. Thus, the value of  $\theta$  for which a given arrival achieves maximum amplitude is associated with the approach azimuth of the component of that arrival traveling with velocity  $c$ . The response of such arrays is discussed more fully in Section 3.3 below.

In the Las Vegas Valley study, since visual analyses of the seismograms suggested that the reflected arrivals were predominantly Rayleigh waves with periods ranging from only about 2.0 to 4.0 seconds, the simple beam-steer process described above was modified to take advantage of this additional information (Murphy and O'Brien, 1978). Thus, since the arrivals of interest were confined to a relatively narrow frequency band, the measured data were filtered through an eighth-order bandpass filter with a transfer function of the form

$$T(S) = \left[ \frac{\omega_c S}{S^2 + \omega_c S + \omega_c^2} \right]^4 \quad (3-1)$$

where  $S$  is the Laplace transform variable and  $\omega_c = 2\pi f_c$  with  $f_c = 0.3$  Hz. This effectively eliminated shorter period body wave phases which were not of primary interest in this case. Next, in order to isolate the contribution to the observed ground motion due to Rayleigh waves arriving from a selected

approach azimuth,  $\theta$ , use was made of the fact that the Rayleigh wave particle motion is restricted to the radial-vertical plane oriented along the approach azimuth. That is, the radial component of motion with respect to  $\theta$  was computed by applying a rotation of axes to the measured orthogonal, horizontal components of motion. Finally, the filtered and rotated data from the array stations were summed with inter-station time delays appropriate for a plane wave approaching from direction  $\theta$  at the Rayleigh wave velocity corresponding to a frequency of 0.3 Hz.

The results of applying this filtering procedure to the CARPETBAG data of Figure 36 are shown in Figure 37. In this figure, zero degrees indicates the azimuth back toward the explosion source and the angle is measured clockwise from north. It can be seen that the output of the filter in this case clearly indicated some strong secondary bursts of energy arriving from directions other than along the azimuth back to the source. The strongest of these was an arrival originating at an azimuth between 160 and 180 degrees which propagated back up the line toward NTS. The general amplitude level associated with this arrival was found to be comparable to that of the direct Rayleigh waves, suggesting that the reflection coefficient at the boundary which is the source of this phase must be close to unity for incident Rayleigh waves with periods near 3.0 seconds. The only other prominent secondary burst of energy which could be easily identified (c.f., Figure 37) was a still later arrival originating at an azimuth of about 120 degrees which was quite similar in character to that originating at 180 degrees.

In order to complete the identification, it was necessary to correlate these arrivals with the structural boundaries of the valley. Figure 38 is a map of the Las Vegas Valley showing the locations of the surrounding mountain

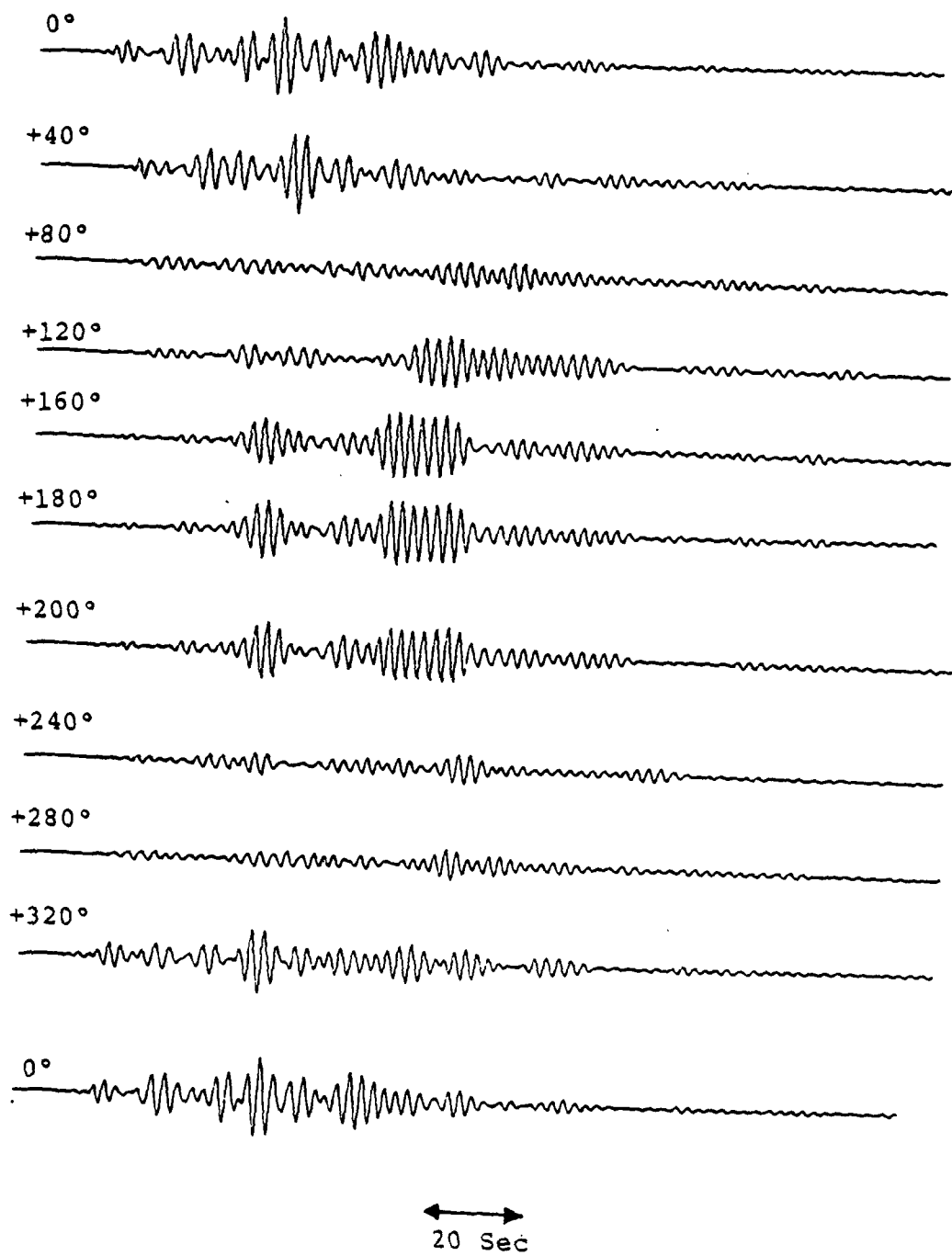
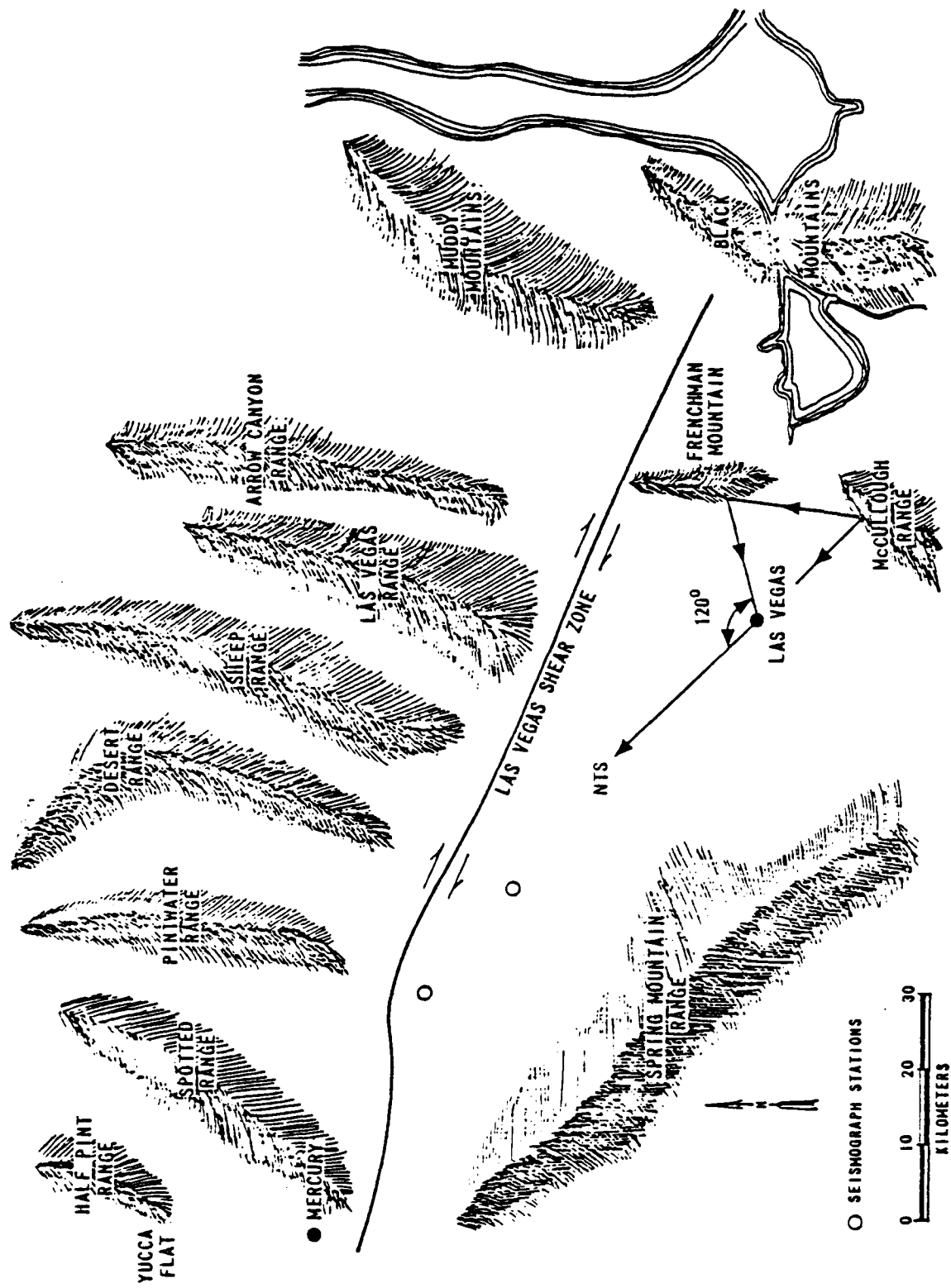


Figure 37. Beam steer analysis of the CARPETBAG Rayleigh waves recorded in Las Vegas.



ranges with respect to the instrumentation array in Las Vegas. It can be seen that the valley is terminated on the southeast by the McCullough mountain range, and the relative arrival time of the secondary signal from an azimuth of 180 degrees was found to be consistent with it being a reflection from this boundary if the average Rayleigh wave propagation velocity at a period of 3.0 seconds is assumed. Perhaps even more interesting is the observation that the arrival time of the phase propagating across the array from an azimuth of 120 degrees was consistent with it being a multiply reflected arrival from Frenchman Mountain following the rather complicated path shown on this figure. If this latter identification is correct then this arrival must correspond to a fairly localized focusing of energy, since its amplitude seems to be too large to be consistent with the hypothesized non-planar reflection.

The Las Vegas data analysis presented above clearly illustrates the fact that the presence of the valley boundaries can significantly modify the ground motion experienced in the valley. However, it is not directly relevant to the MX valley reverberation question in that the source was located some 150 km away outside of the valley. In order to examine the problem on a more appropriate scale, data recorded from the NTS event CALABASH in Yucca Valley have also been analyzed. Figure 39 shows the locations of CALABASH and the stations that were deployed to measure the near-field ground motions from this event. It can be seen from this figure that the instrumentation array encompassed stations located at about the same distance (7 to 8 km) both outside and inside the valley. Figure 40 shows a vertical subsurface geologic section along the line A-A' on Figure 39 which indicates that the alluvium in the area gradually thins to the west until it terminates against the underlying tuff formation at the valley boundary. Figure 41 shows a comparison of

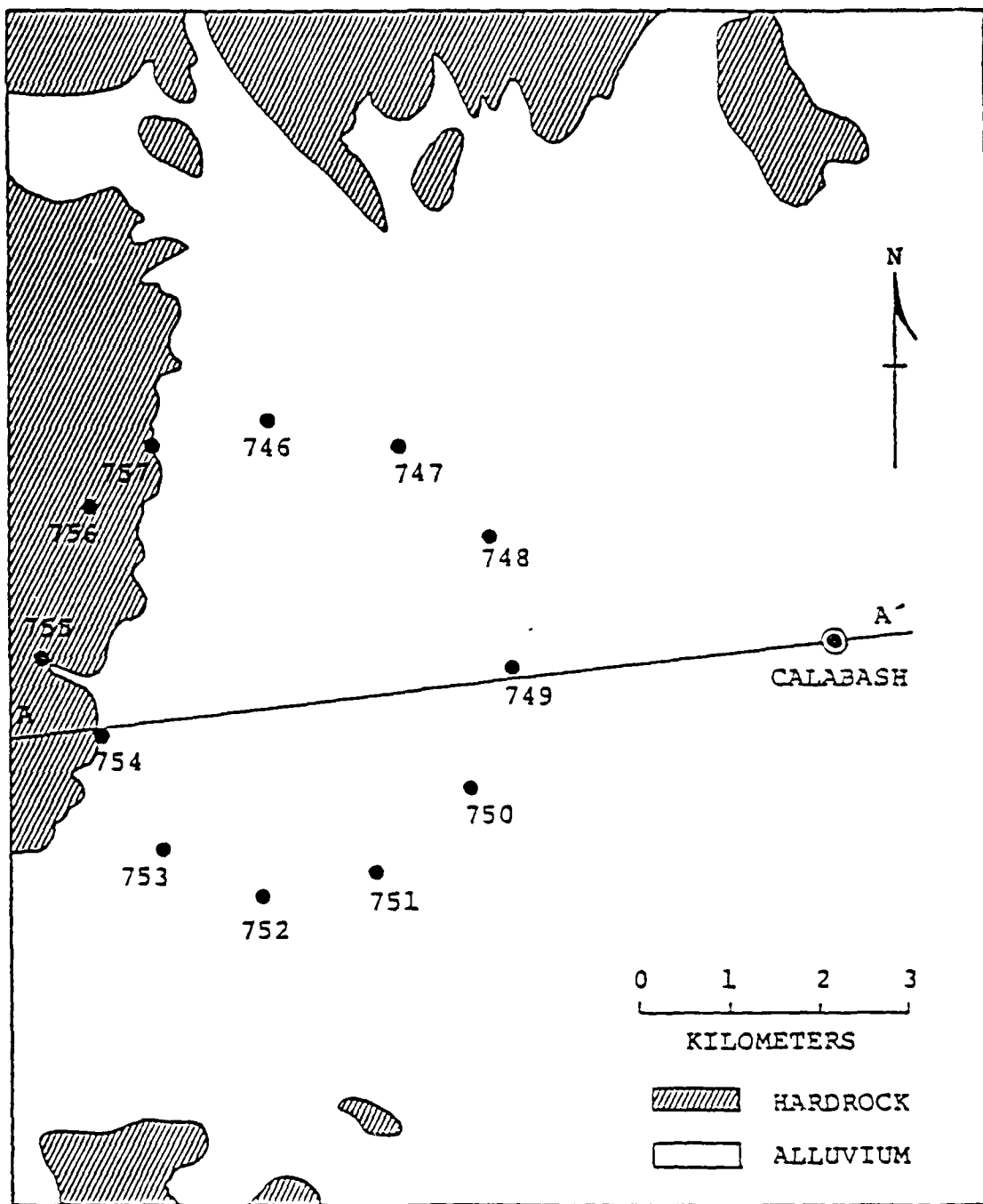


Figure 39. CALABASH station location map.

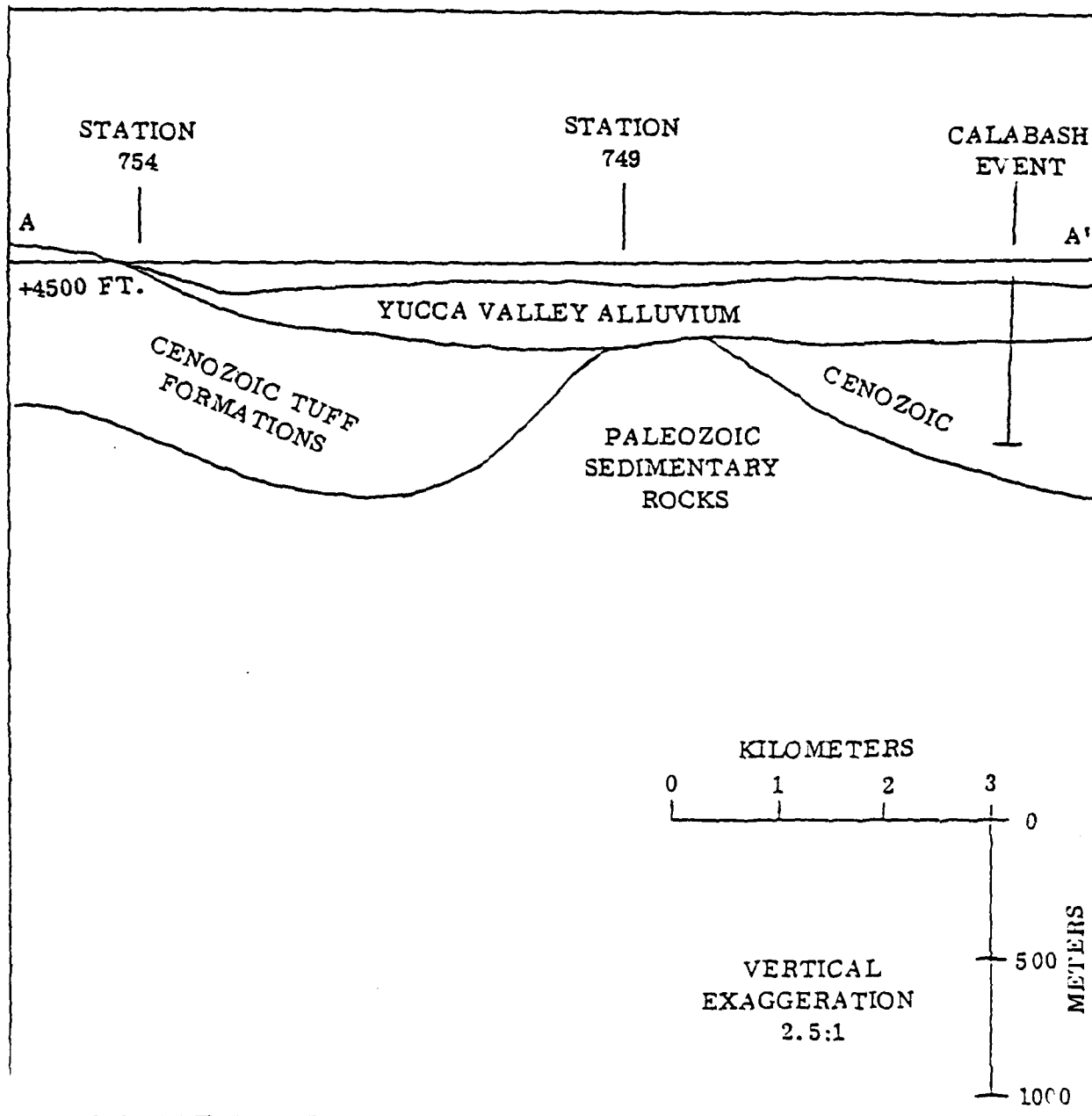


Fig. 40. Vertical geologic section for the CALABASH event.

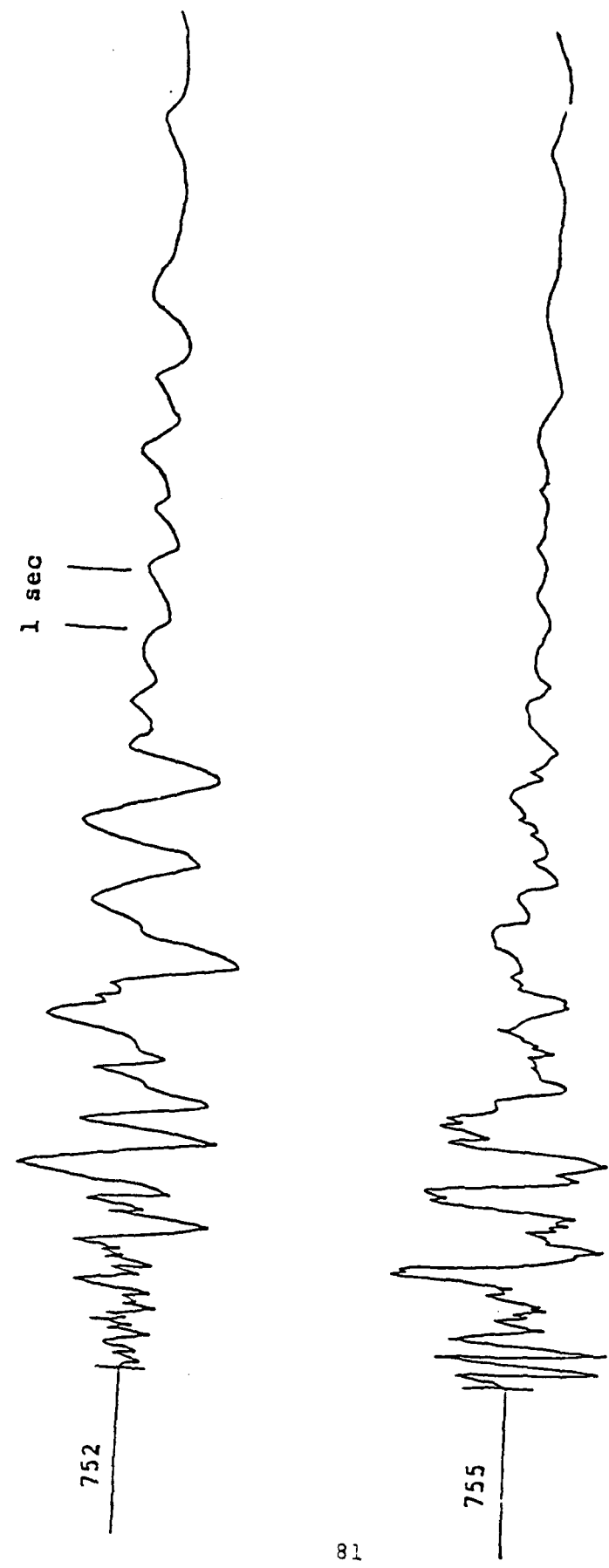
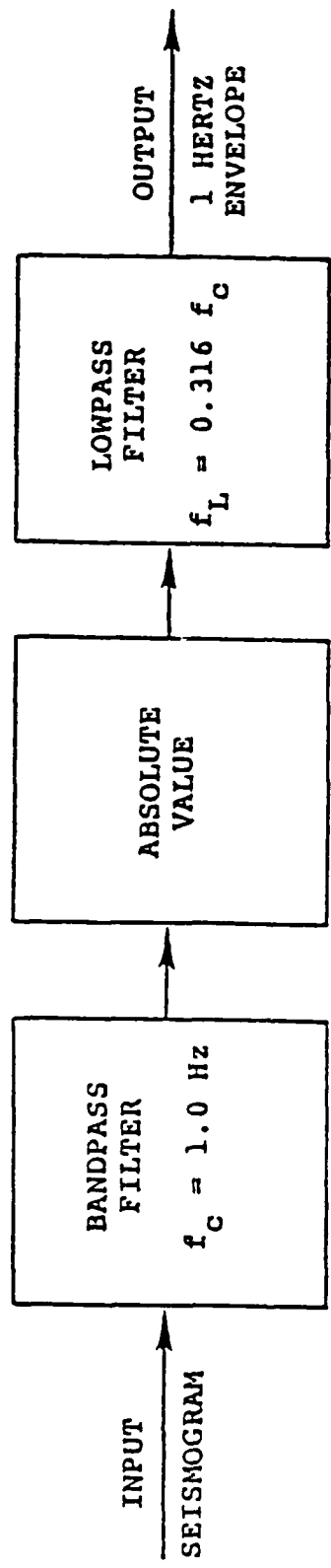


Figure 41. Comparison of ground motion records recorded at about the same distance inside (752) and outside (755) Yucca Valley, CALABASH event.

the radial component velocity time histories measured for CALABASH at stations 752 (in the valley) and 755 (on the valley boundary). It can be seen that although these stations were located at about the same distance from the source, there was a significant difference in the effective duration with the closer, in-valley station (752) showing clear evidence of later secondary arrivals. This difference is even more apparent when the envelopes of the signals in a narrow frequency band are compared. Figure 42 shows a block diagram of the envelope detector which was selected to process the recorded data. The passband around 1 Hz was chosen for analysis in this case on the basis of a visual identification of the characteristic frequencies of the late-time motions recorded on the array. Figure 43 shows the 1 Hz envelopes of the signals shown in Figure 41, and Figure 44 shows the envelopes for another pair of stations one of which was inside (746) and one of which was outside (756) the valley. In both cases there is clear evidence of strong secondary arrivals at the stations inside the valley which appear to have no counterparts on the records of adjacent stations located outside the valley. This strongly suggests that a significant amount of energy is being reflected back from the valley boundary and modifying the motion inside the valley.

We next turn to the theoretical studies; we will return to observational results from the MB-II studies in Section 3.3. The theoretical investigation of valley reverberation is a difficult problem because of the complexity of the geologic structure involved. For example, it is questionable whether valleys such as those discussed above can be adequately modeled without going to a full three dimensional description of the valley boundaries. Although such a simulation is probably within the current state of the art, it would undoubtedly be very costly and time consuming, particularly in view of the fact that there is so little previous



$$\begin{aligned}
 & \left[ \frac{\omega_C s}{s^2 + \omega_C s + \omega_C^2} \right]^4 \\
 & \frac{\omega_L^2}{s^2 + 1.414 \omega_L s + \omega_L^2}
 \end{aligned}$$

Figure 42. Block diagram of the bandpass filter envelope circuit.

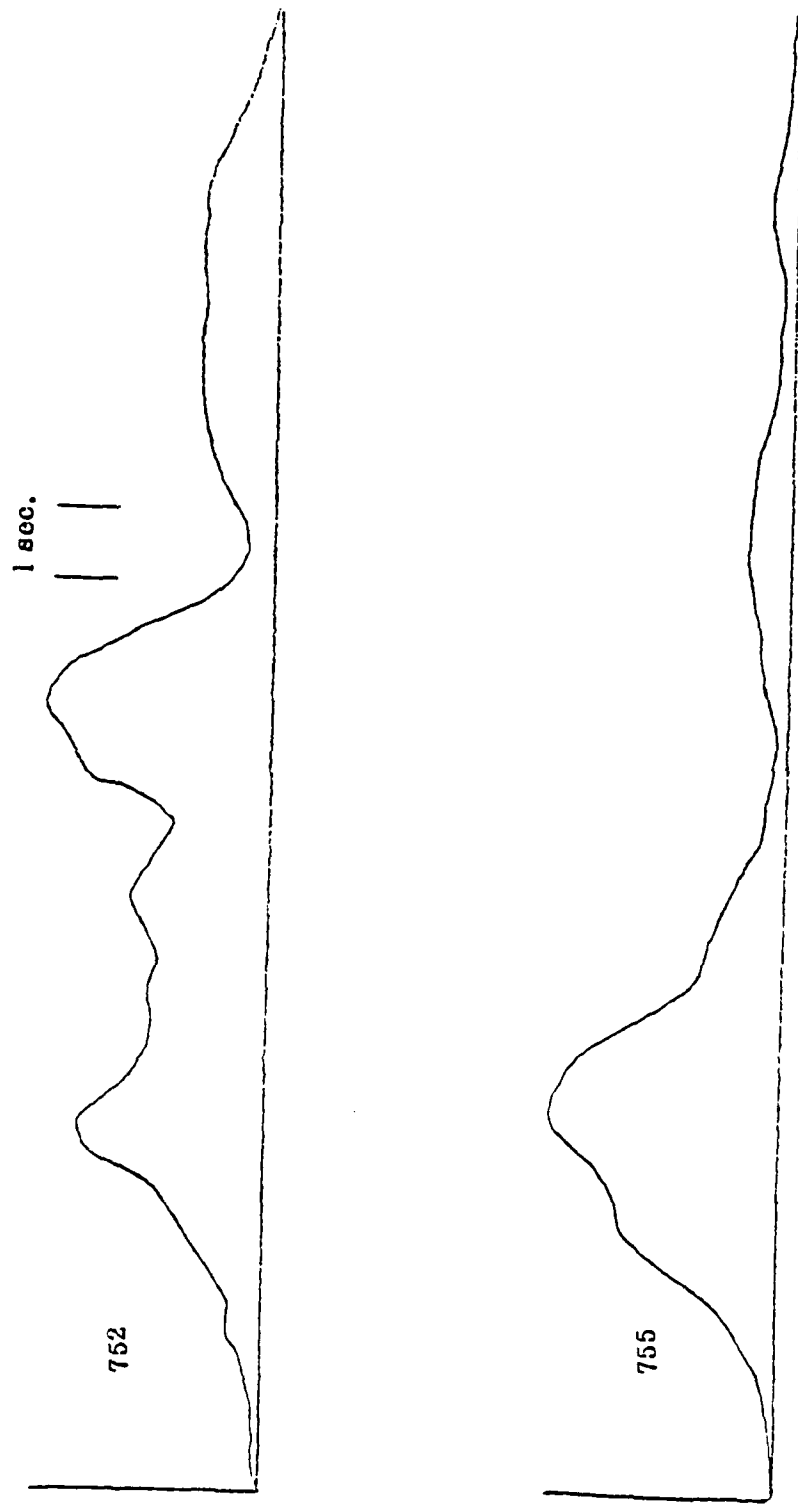


Figure 43. Comparison of the 1 Hz envelope for stations inside (752) and outside (755) Yucca Valley.

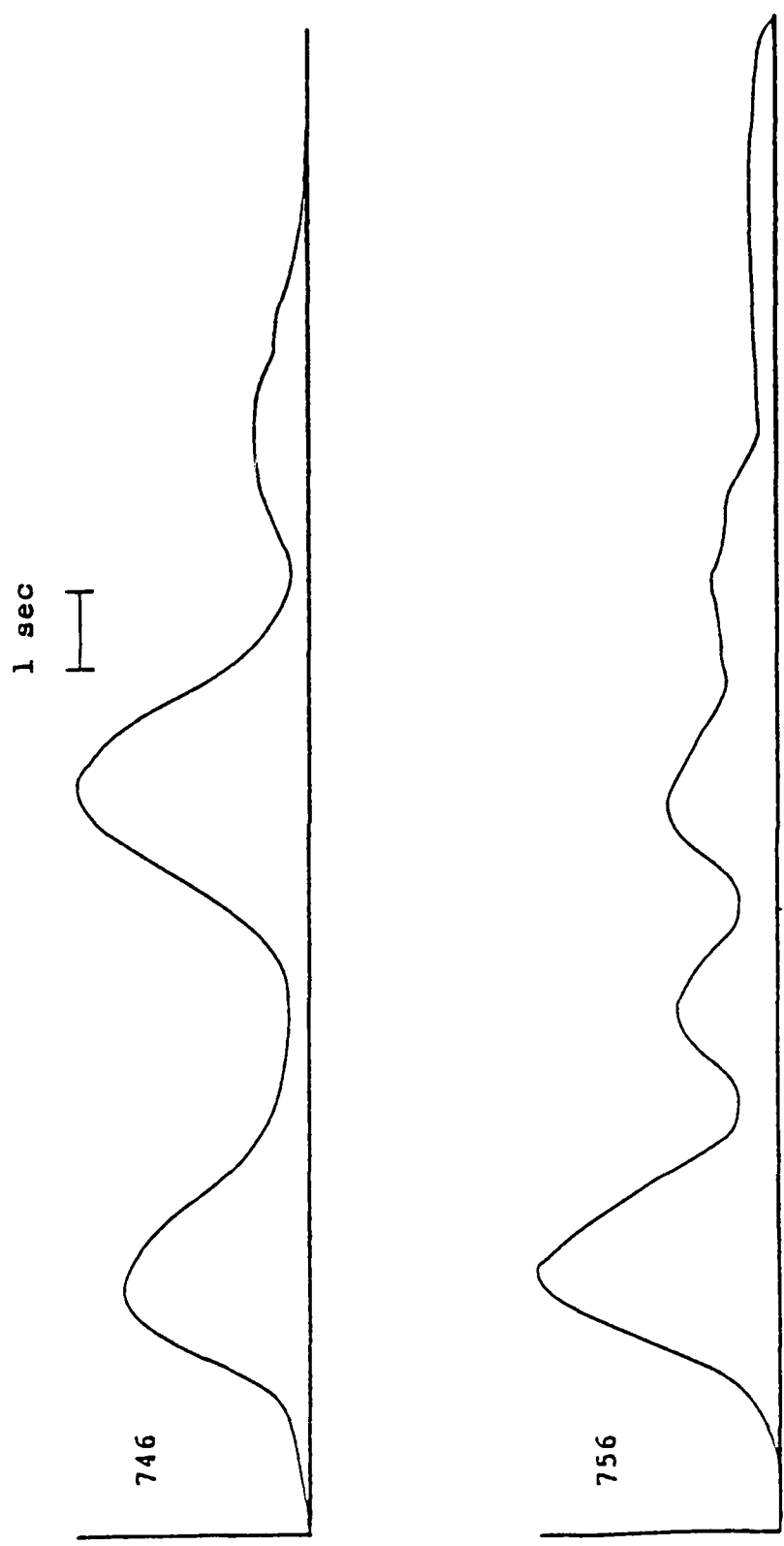
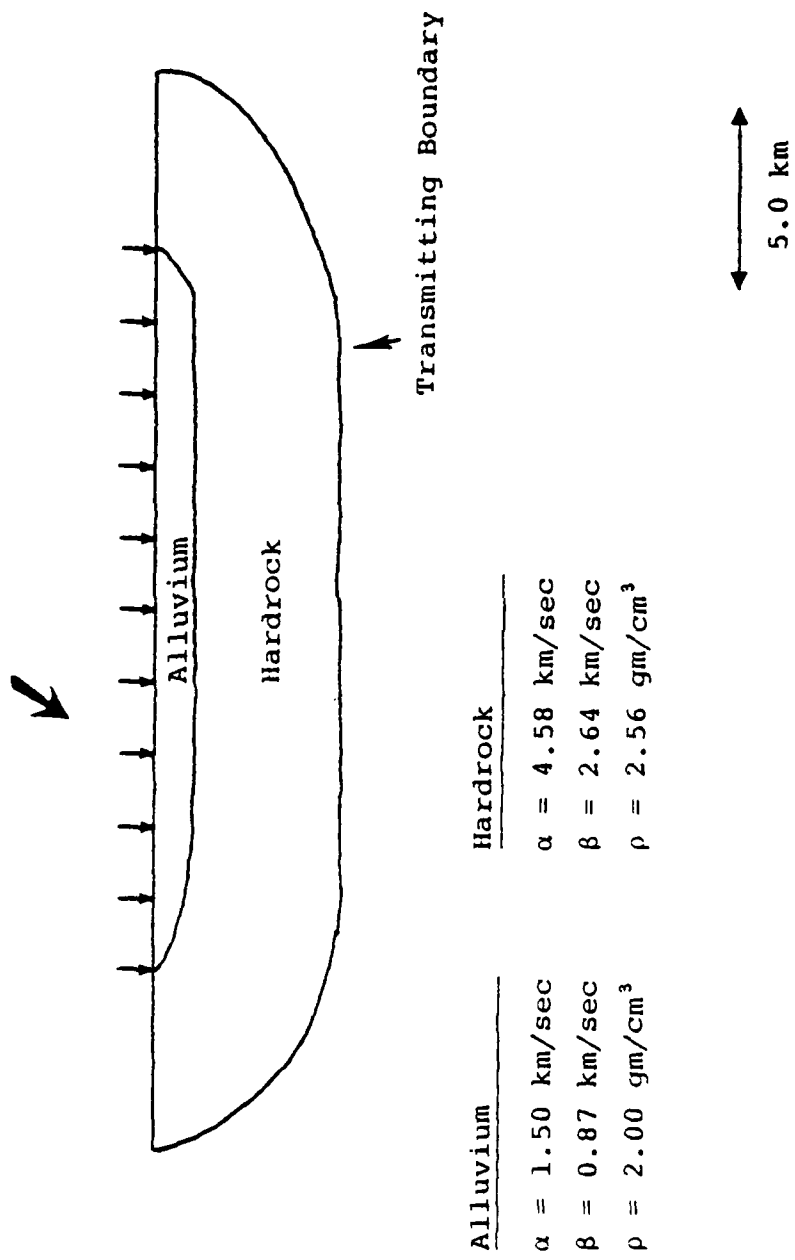


Figure 44. Comparison of the 1 Hz envelope for stations inside (746) and outside (756) Yucca Valley.

experience at modeling structures of this complexity at a realistic scale. For these reasons, the two studies conducted to date (Orphal and Hancock, 1978; Cherry, et al., 1978) have consisted of finite difference simulations of the response of highly simplified, two-dimensional approximations to a valley structure. The results of these preliminary studies are summarized in the following paragraphs.

Orphal and Hancock (1978) considered the response of a 20 km wide elliptical alluvial valley of infinite length assuming plane-strain symmetry. The geometry and loading conditions for the problem are illustrated in Figure 45 which shows that the entire valley was simultaneously loaded with an overpressure pulse of constant peak amplitude (i.e., 1 bar) and a pulse shape consistent with that expected at that peak pressure from a 1 megaton surface burst (Brode, 1968). This loading was taken as a crude approximation to the effect of a multiburst attack on an MX valley. The simulation was carried out using the Physics International PISCES 2D ELK continuum mechanics, finite difference computer code. The problem was further simplified by assuming that the response of the geologic materials to the loading was perfectly elastic everywhere. Figure 46 shows the computed horizontal particle velocity time histories as a function of range from the center of the valley (i.e.,  $r = 0$ ). Since the companion simulation run in the absence of the valley boundaries has not yet been performed, it is difficult to make a quantitative assessment of how much the valley boundaries are affecting the ground motion response. However, several strong, low-frequency secondary phases can be identified which are clearly propagating back in toward the center of the valley. This is more clearly illustrated in Figure 47 which shows "snapshots" of the horizontal particle velocity as a function of position in the valley at progressively later times. It can be seen that as time advances a standing-wave pattern

Brode Overpressure for 1 Mt  
Constant Peak Pressure of 1 bar



Alluvium

Hardrock

$\alpha = 1.50 \text{ km/sec}$   
 $\beta = 0.87 \text{ km/sec}$   
 $\rho = 2.00 \text{ gm/cm}^3$

$\alpha = 4.58 \text{ km/sec}$   
 $\beta = 2.64 \text{ km/sec}$   
 $\rho = 2.56 \text{ gm/cm}^3$

Figure 45. Geometry and loading conditions for elliptical valley approximation.

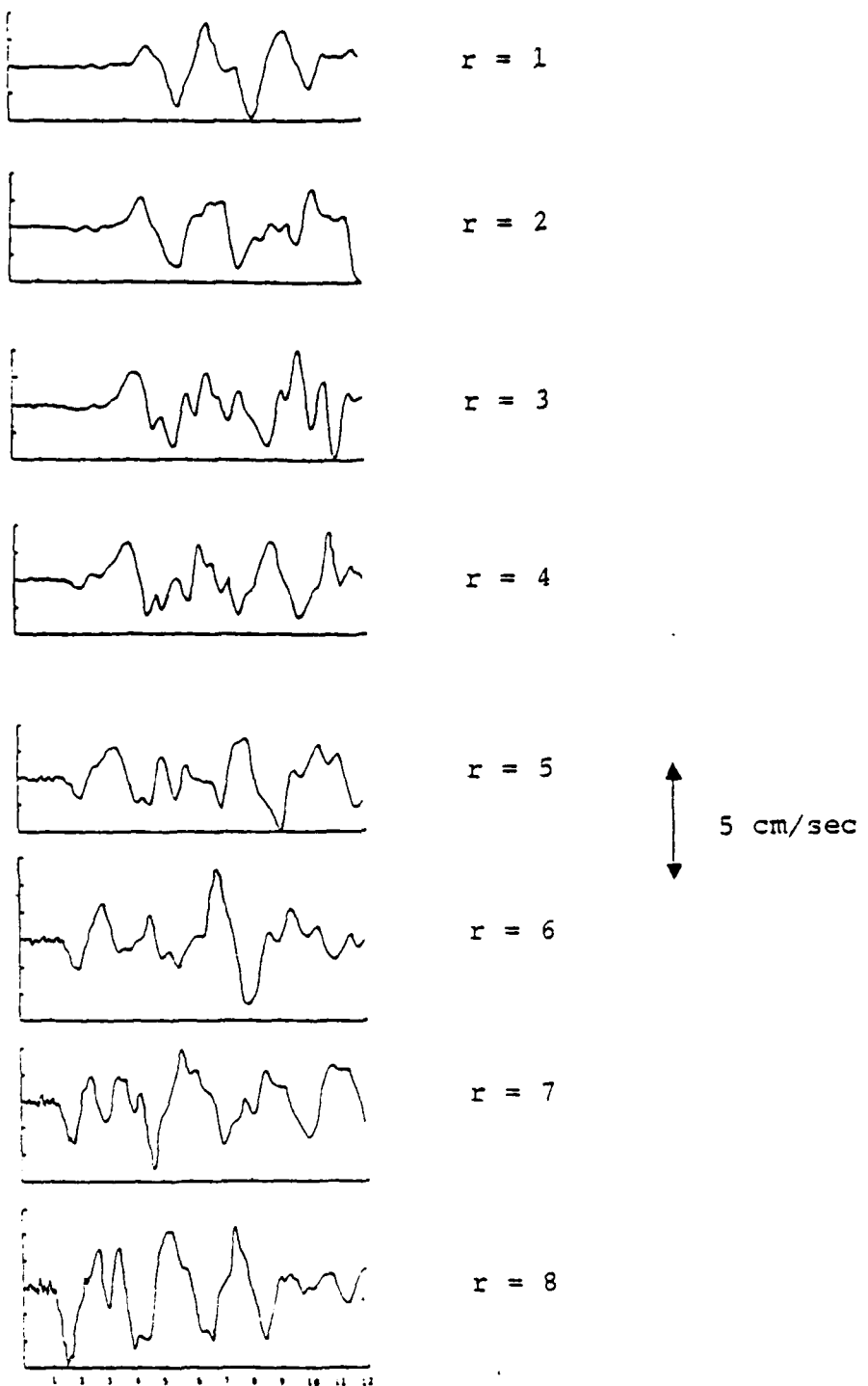


Figure 46. Computed horizontal particle velocity seismograms as a function of distance from the valley center.

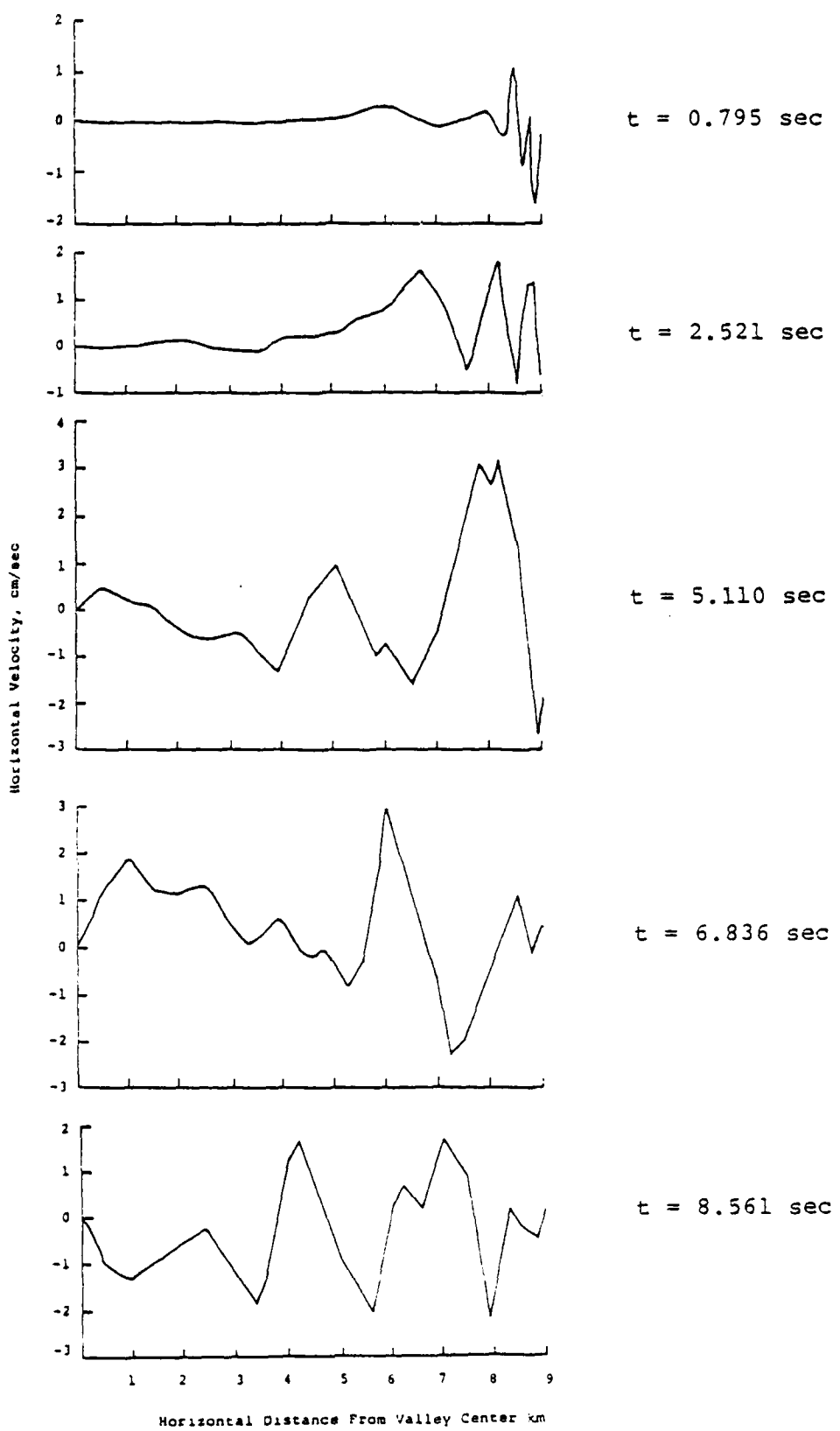


Figure 47. Comparison of particle velocity profile across the valley at selected times.

seems to be building up in the valley, although the problem was not run long enough to allow the pattern to fully develop. In any case, it seems clear that a significant amount of energy is being reflected back from the valley boundaries, leading to an increase in the duration of motion which is at least qualitatively consistent with the observed data.

Cherry, et al. (1978) considered a cylindrical valley approximation and used a special purpose, elastic finite difference code to compute the ground motion response both with and without a valley boundary. In both cases, the surface area outside the expected final crater region (i.e., region of strong nonlinear response) was loaded with a Brode (1968) airblast appropriate for a single, megaton yield surface burst. Figure 48 shows the subsurface geological model used in these simulations. It can be seen that this model was more complicated than that used by Orphal and Hancock (c.f., Figure 45) and was, in fact, chosen to be a plane layered representation of a typical Basin and Range valley structure. An initial simulation was made in which these layers were taken to have infinite horizontal extent (i.e., no valley boundaries), and this served as a basis for comparison. In the second simulation, a vertical boundary was inserted at a range of 3 km from the center of the valley, and it was surrounded by the underlying basement rock (i.e., granite). Figures 49 through 54 show comparisons of the vertical and horizontal components of the particle velocity at three different ranges (i.e., 0.9, 2.03 and 2.96 km from the center of the valley) computed with and without the valley boundary. Again, it can be seen that the valley boundaries significantly affected the ground motion response in the valley, particularly with regard to the duration of the longer-period surface waves. For example, the upper traces in Figures 49 and 50 indicate that at a range of 0.9 km the effective duration of motion was less than 10 seconds in the

DEPTH (M)	THICKNESS (M)	P VELOCITY (KM/s)	S VELOCITY (KM/s)	DENSITY (GM/CM <sup>3</sup> )
0				
	300	2.0	0.6	1.9
400				
	600	2.75	1.6	2.0
1000				
	2000	4.0	2.3	2.2
3000				
	$\infty$	5.5	3.18	2.65

Figure 48. Plane layered approximation to a Basin and Range valley structure.

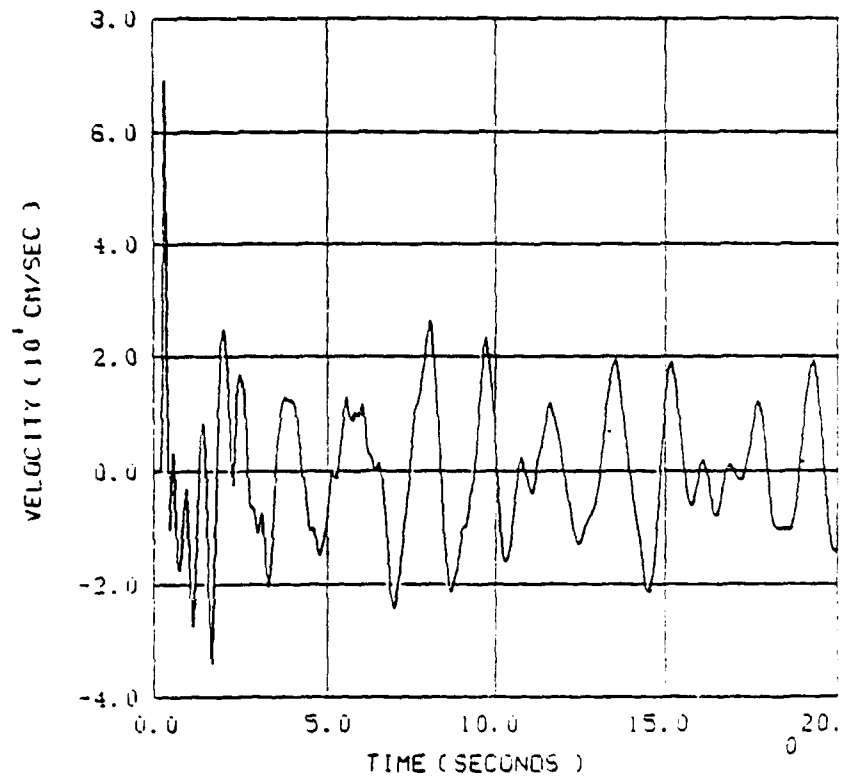
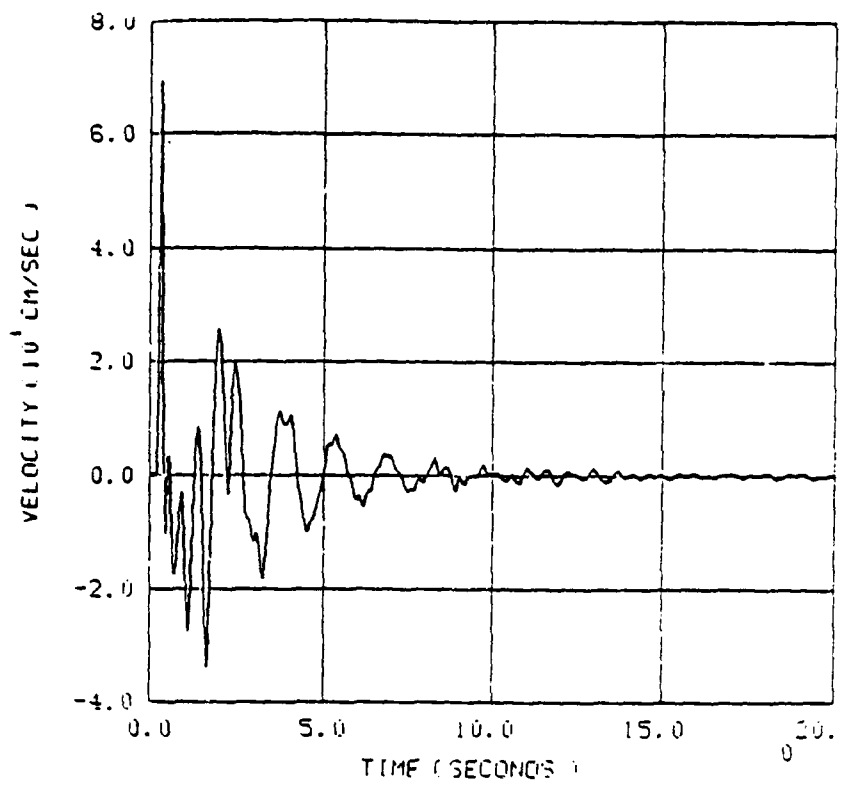


Figure 49. Comparison of free surface horizontal velocity computed without (top) and with (bottom) a valley boundary,  $r = 0.9$  km.

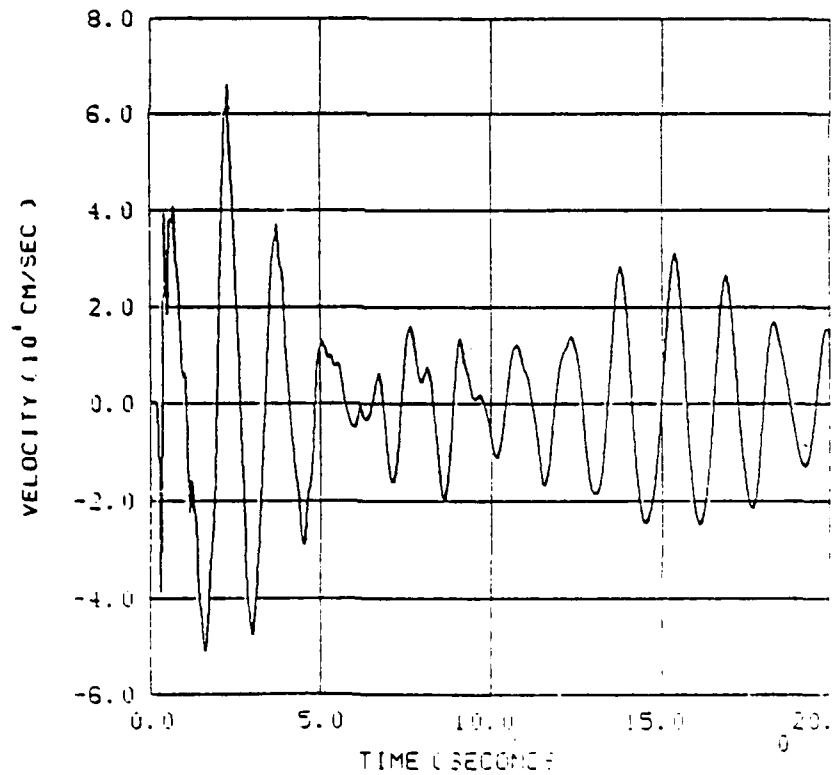
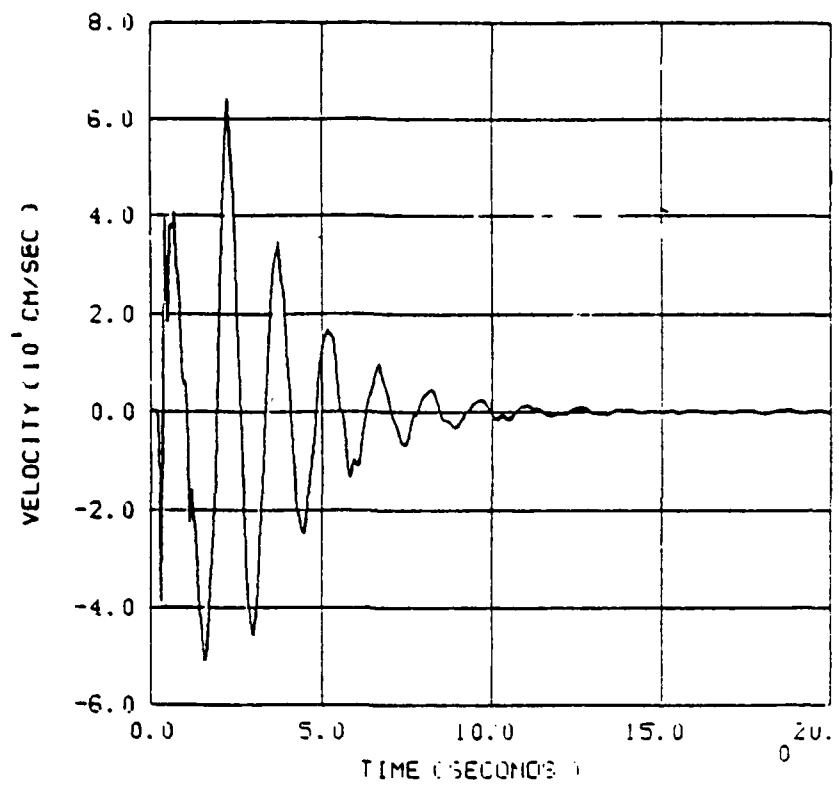


Figure 50. Comparison of free surface vertical velocity computed without (top) and with (bottom) a valley boundary,  $r = 0.9$  km.

AD-A093 794

SYSTEMS SCIENCE AND SOFTWARE LA JOLLA CA  
ANALYSIS OF THE LOW FREQUENCY GROUND MOTION ENVIRONMENT FOR MX,--ETC(U)  
JAN 80 J R MURPHY, T J BENNETT  
DNA001-79-C-0114

UNCLASSIFIED

SSS-R-80-4298

DNA-5219F

ML

2007  
42-22-16

END  
DATE 1/18/80  
TIME 2:00 PM  
2-8A  
DTIC

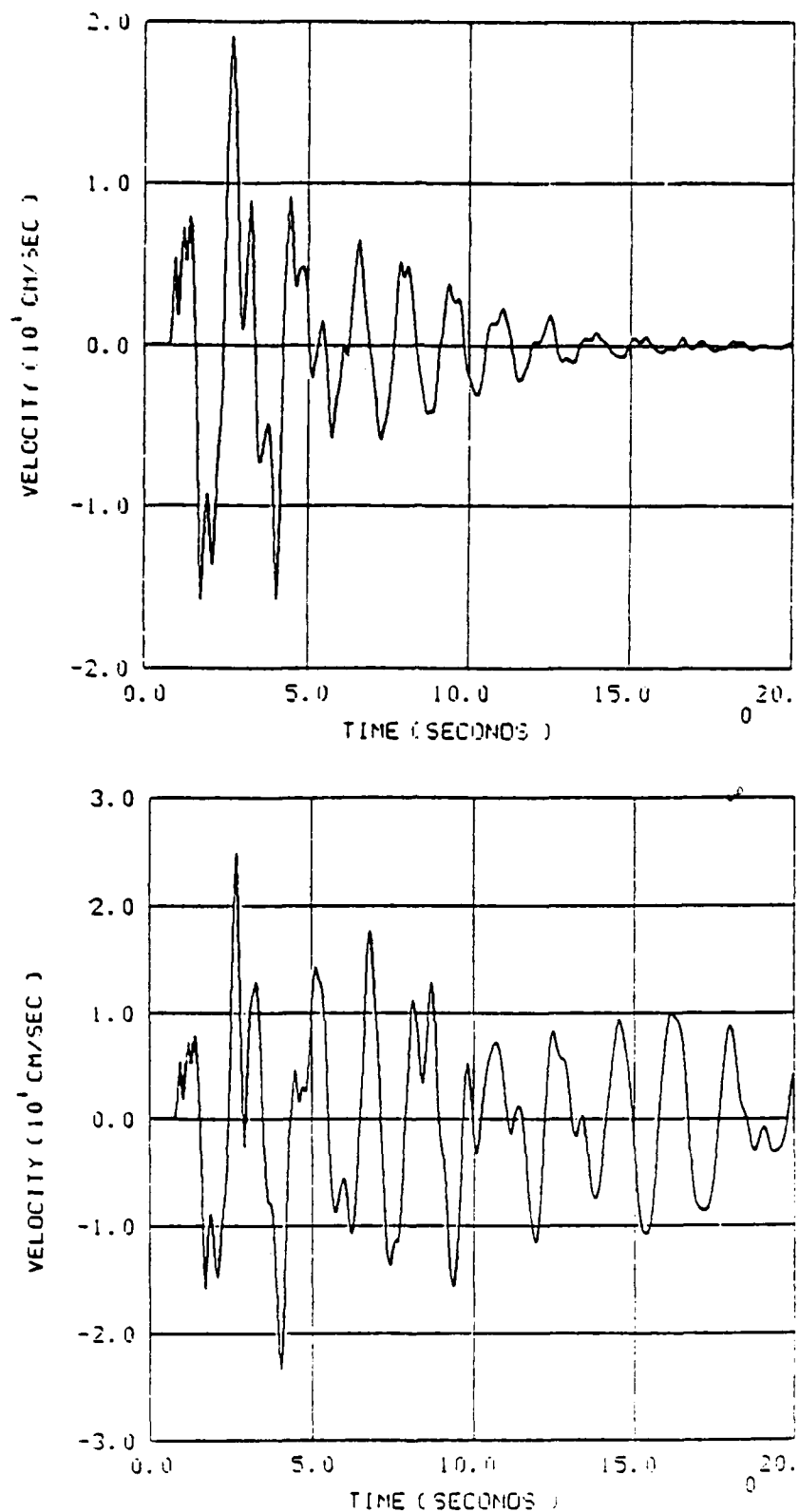


Figure 51. Comparison of free surface horizontal velocity computed without (top) and with (bottom) a valley boundary,  $r = 2.03$  km.

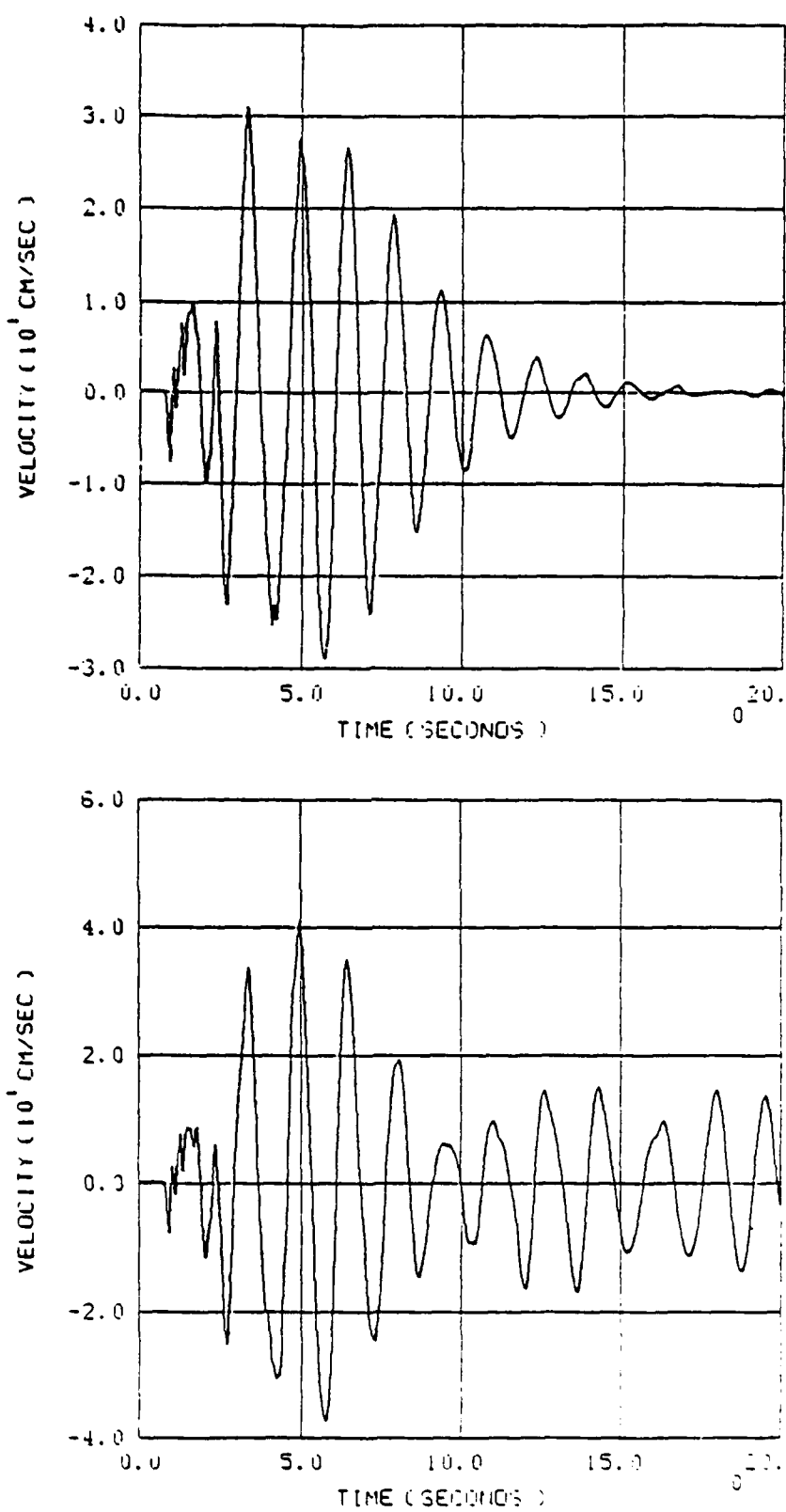


Figure 52. Comparison of free surface vertical velocity computed without (top) and with (bottom) a valley boundary,  $r = 2.03$  km.

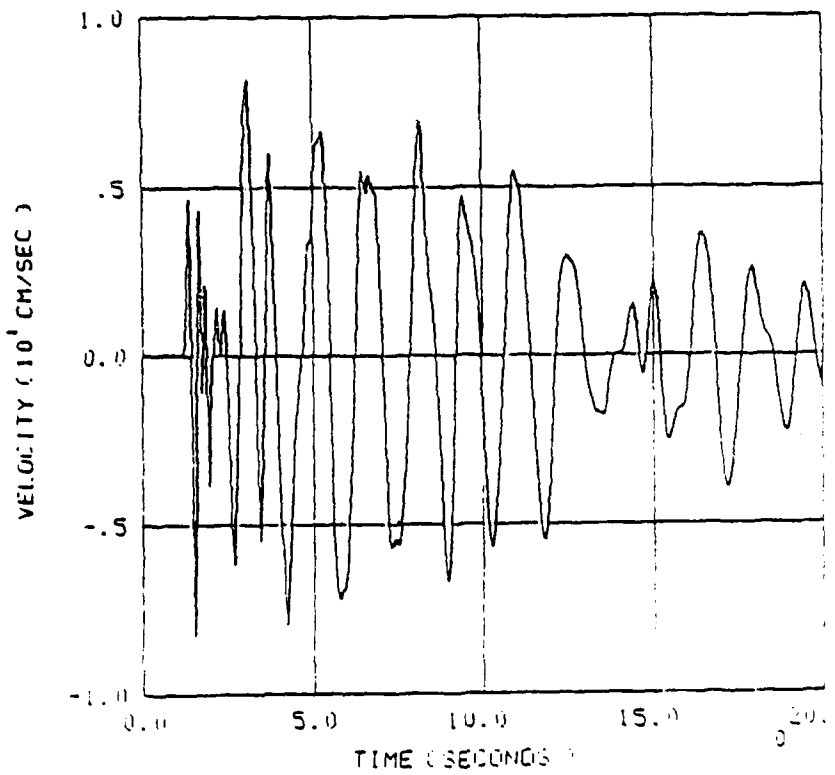
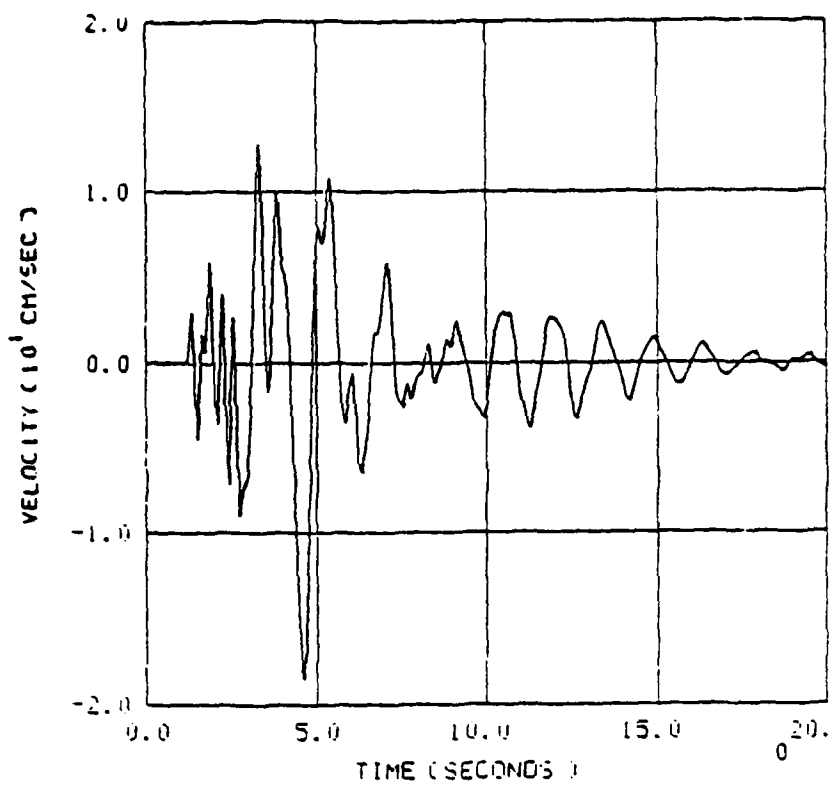


Figure 53. Comparison of free surface horizontal velocity computed without (top) and with (bottom) a valley boundary,  $r = 2.96$  km.

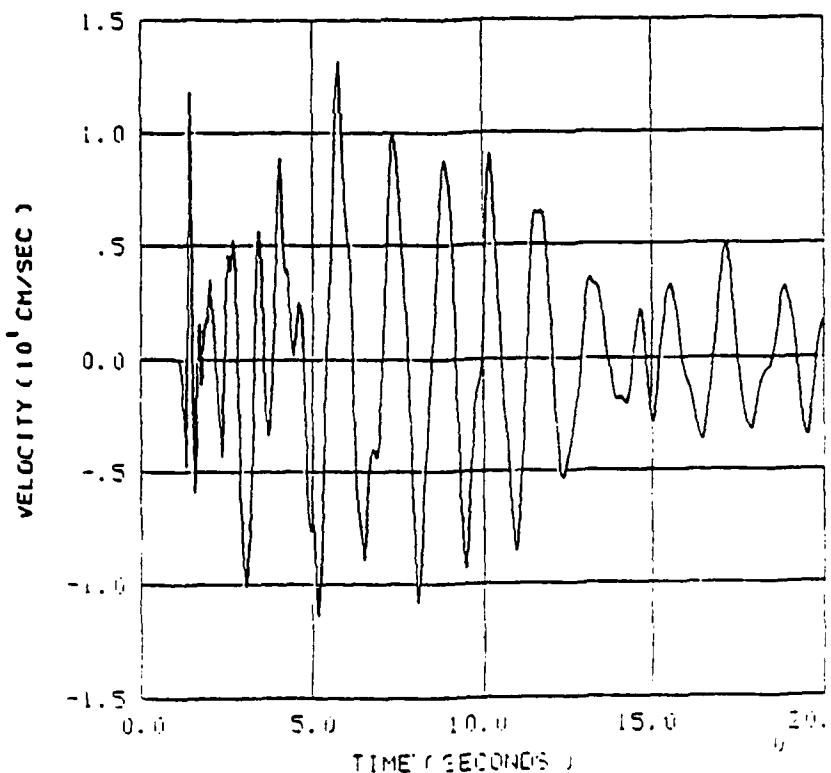
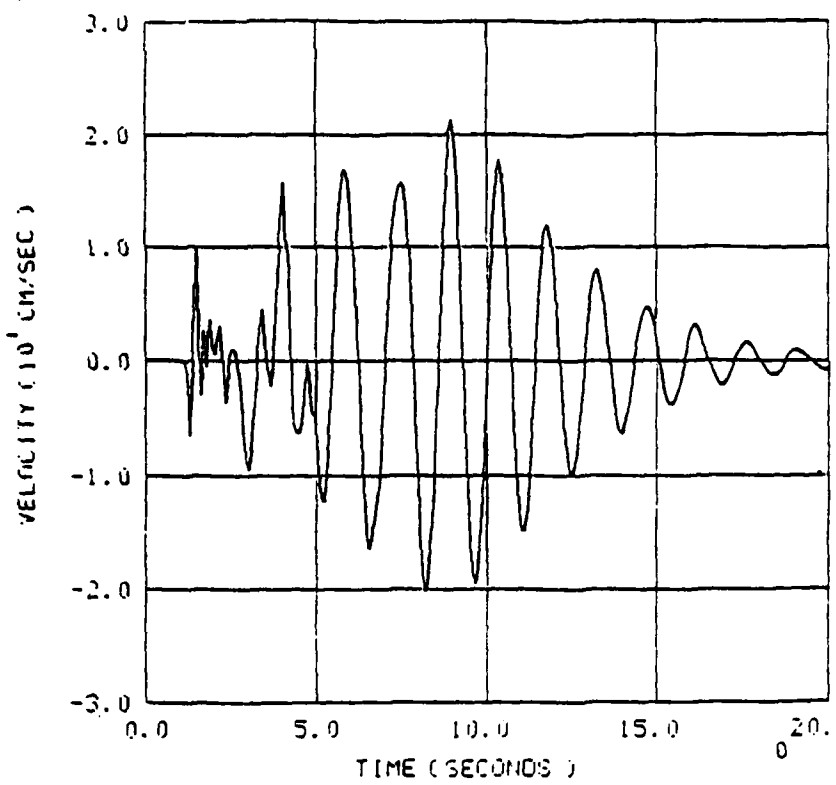


Figure 54. Comparison of free surface vertical velocity computed without (top) and with (bottom) a valley boundary,  $r = 2.96$  km.

absence of the valley boundary. However, at that same location for the valley simulation (i.e., the lower traces in these figures) the amplitude of the lower frequency ( $\sim 0.6$  Hz) surface wave motion 20 seconds after detonation time, when the calculation stopped, was still comparable to that of the direct-arriving surface wave energy. This indicates that a substantial amount of energy is being reflected back from this vertical discontinuity in physical properties. In general, the effect of the valley boundaries on the peak velocity values were seen to be much less pronounced than the effect on duration. However, an exception to this occurred for the vertical velocity at the station very close to the boundary (i.e.,  $r = 2.96$  km). Here, as can be seen from Figure 54, the peak velocity for the problem with the valley boundary was actually about a factor of two smaller than that which was observed in the absence of the valley boundary. This effect was found to be due to destructive interference between the incident and reflected Rayleigh waves and has been used by Cherry, *et al.* (1978) to infer a Rayleigh wave reflection coefficient of about 0.5 for this geologic model.

### 3.3 MISERS BLUFF II REVERBERATION STUDIES

#### 3.3.1 Data Analyses

As noted above, the Misers Bluff II (MBII) explosions were a series of two HE tests designed to simulate the blast ground motion environment in an MX valley. One element of the MBII study was specifically designed to test the effects on ground motion of reverberation of seismic waves in the "miniature MX valley" at Planet Ranch in Arizona. Instrumentation for this element of the study consisted of the seismic stations shown in Figure 55. The stations for the MBII-1 explosion are shown as solid circles and the stations for the MBII-2 explosion are shown as open circles; the station at the southern edge of the valley was in place for both

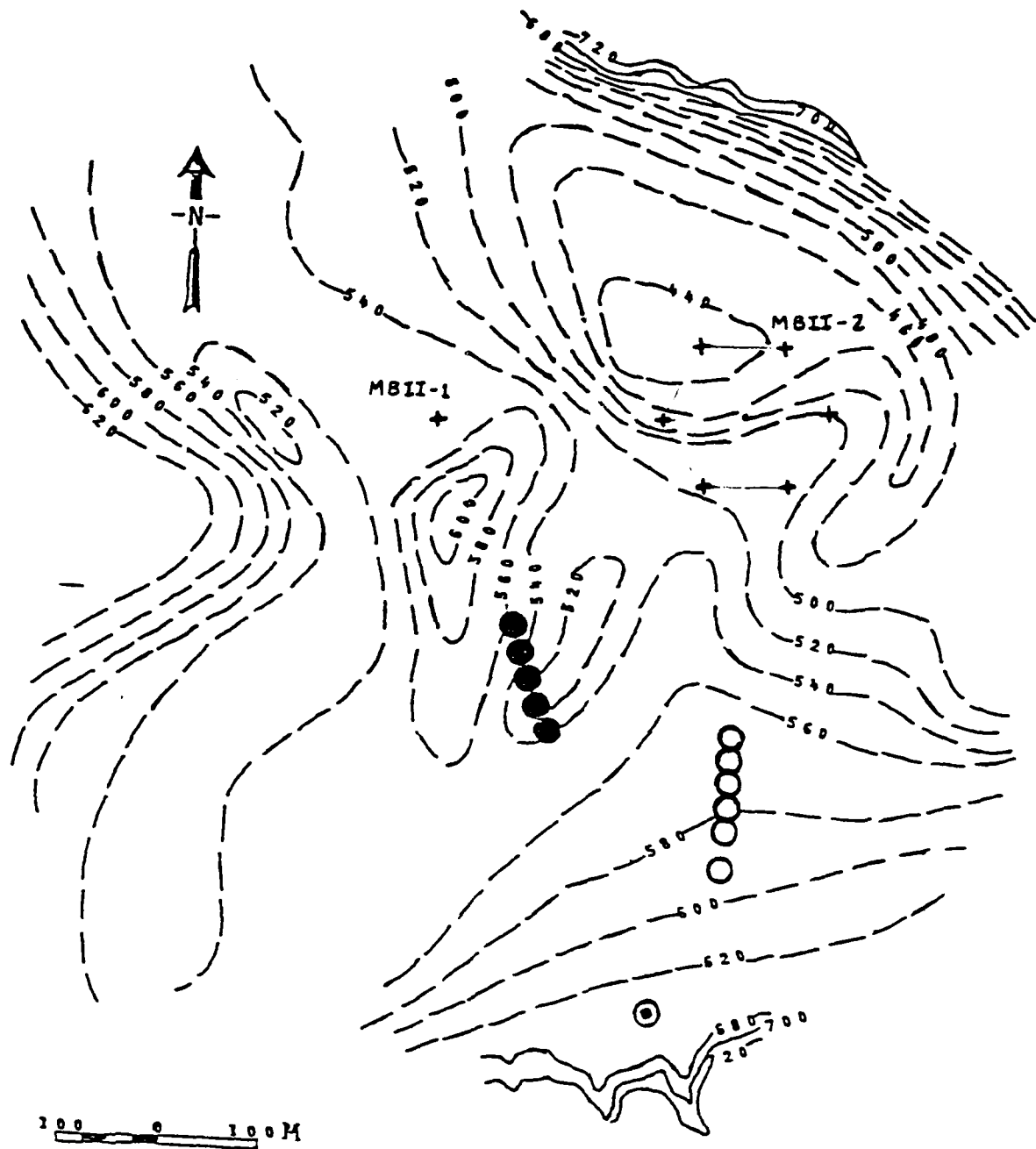


Figure 55. Bedrock contour map for Misers Bluff II site with locations for individual explosions (+) and recording stations (●) for the MBII-1 single burst event and (○) for the MBII-2 multiple burst event. Contour lines give bedrock elevations in feet; local average surface elevation is 670 feet.

explosions. Each station included two horizontal instruments designed to respond to radial (i.e., along the shot/station line) and transverse (i.e., perpendicular to the shot/station line) motions. In addition, four stations for each explosion were equipped with vertical instruments. The station near the southern edge of the valley also included three-component down-hole instrumentation. Velocity records from the broad-band instruments were integrated to obtain displacement time histories which were used in our analysis.

Also shown in Figure 55 are bedrock contours of the valley. The contours on this figure show the bedrock elevation in feet; the average surface elevation at the site is about 670 feet. It can be seen that even in the center of the valley the alluvium thickness varies between 20 and 70 meters. In particular, note that there is a local high in the bedrock topography located between the source and the station array. As might be expected, this local anomaly, which was mapped after the design of the reverberation array had been finalized, further complicates the interpretation of an already complex data set.

Figure 56 shows a comparison of ground motion records measured at a range of about 300 m from two different 100 ton HE experiments. The lower trace was measured from the Pre-Mine Throw IV (PMT IV) test conducted at the Nevada Test Site and has an effective duration of only about one second. By contrast, the upper trace recorded at about the same range from the MBII-1 test in the Planet Ranch valley shows an effective duration of at least ten seconds. Thus, there is clear evidence of reverberation of seismic energy within the valley structure. Another observation that can be made from this recording is that the characteristic frequency associated with the secondary arrivals is significantly lower than that of the initial, direct arrivals. This is illustrated

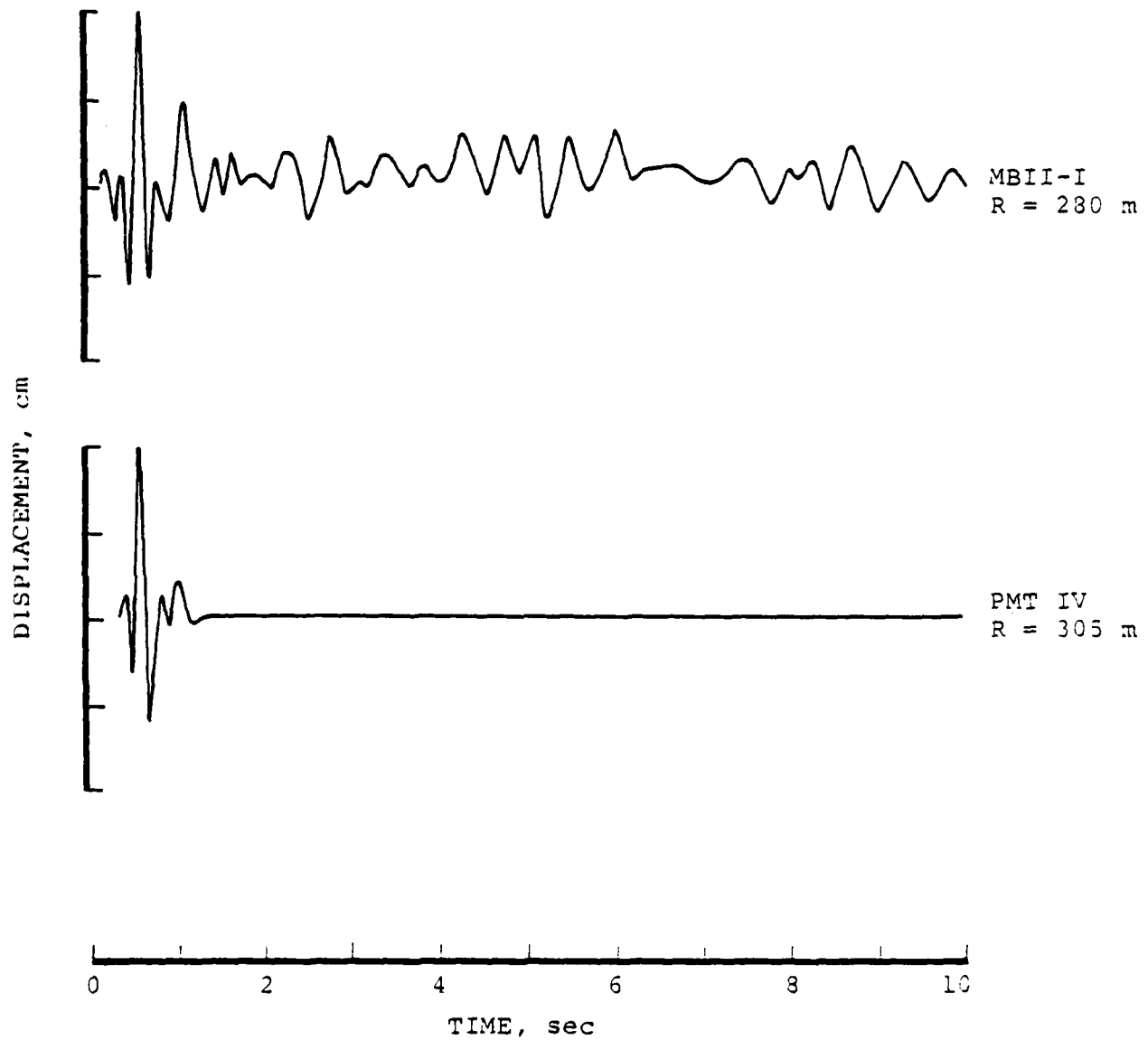


Figure 56. Comparison of ground motion time histories recorded at comparable ranges from the 100 ton HE events Misers Bluff II-1 (MBII-I) and Pre-Mine Throw IV (PMT IV).

more clearly in Figure 57 which shows the result of passing one of the recorded MBII-1 displacement time histories through eighth-order bandpass filters centered at 4.0 and 2.0 Hz. It can be seen that most of the 4.0 Hz energy is concentrated near the beginning of the signal, while the 2.0 Hz component of the motion maintains a relatively continuous level over the entire 10 seconds of recording. It seems likely that this difference in characteristic frequency reflects differences in average properties of the associated propagation paths. This is illustrated in Figure 58 which shows the fundamental Rayleigh wave site response functions for the Planet Ranch site. Now, the direct arrivals travel along a path for which the average thickness of alluvium is around 40 m, giving a characteristic Rayleigh wave frequency of 4.0 Hz. The late-time reverberation signals, on the other hand, may traverse portions of the valley where the alluvial thickness is 70 m or more, leading to a characteristic Rayleigh wave frequency closer to 2.0 Hz.

We processed the MBII array data using a procedure of frequency filtering and beam-steering like that used in the analysis of the Las Vegas array data described above. A schematic describing the beam-steering process, as used here, is shown in Figure 59. Stations in the recording array, represented by the black circles, are uniformly separated by a distance,  $d$ . The wave motion recorded on the array is assumed to consist of plane waves which travel at a velocity,  $c$ , and propagate at an azimuth angle  $\theta$  relative to the line of stations. Assuming that there is no change in waveform across the array and the motion at station 1 is represented by  $F(t)$ , then the motions at other stations in the array are simply delayed in time by an amount equal to the time for the wavefront to travel from the position intersecting station 1 to a position intersecting the other stations. Then, the wave motion at stations in the array can be represented as:

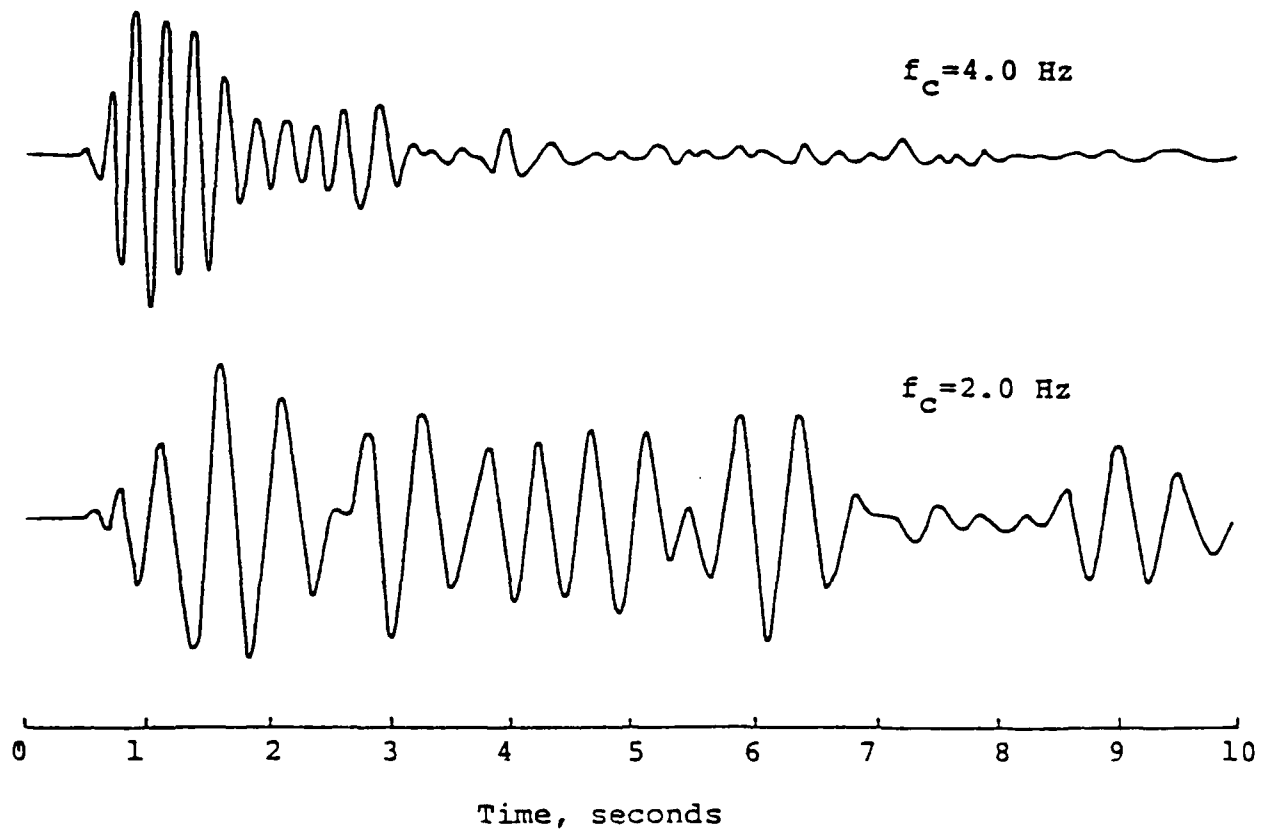


Figure 57. Comparison of eighth order bandpass filtered displacements at 4.0 and 2.0 Hz; MBII-1,  $r = 305 \text{ m}$ .

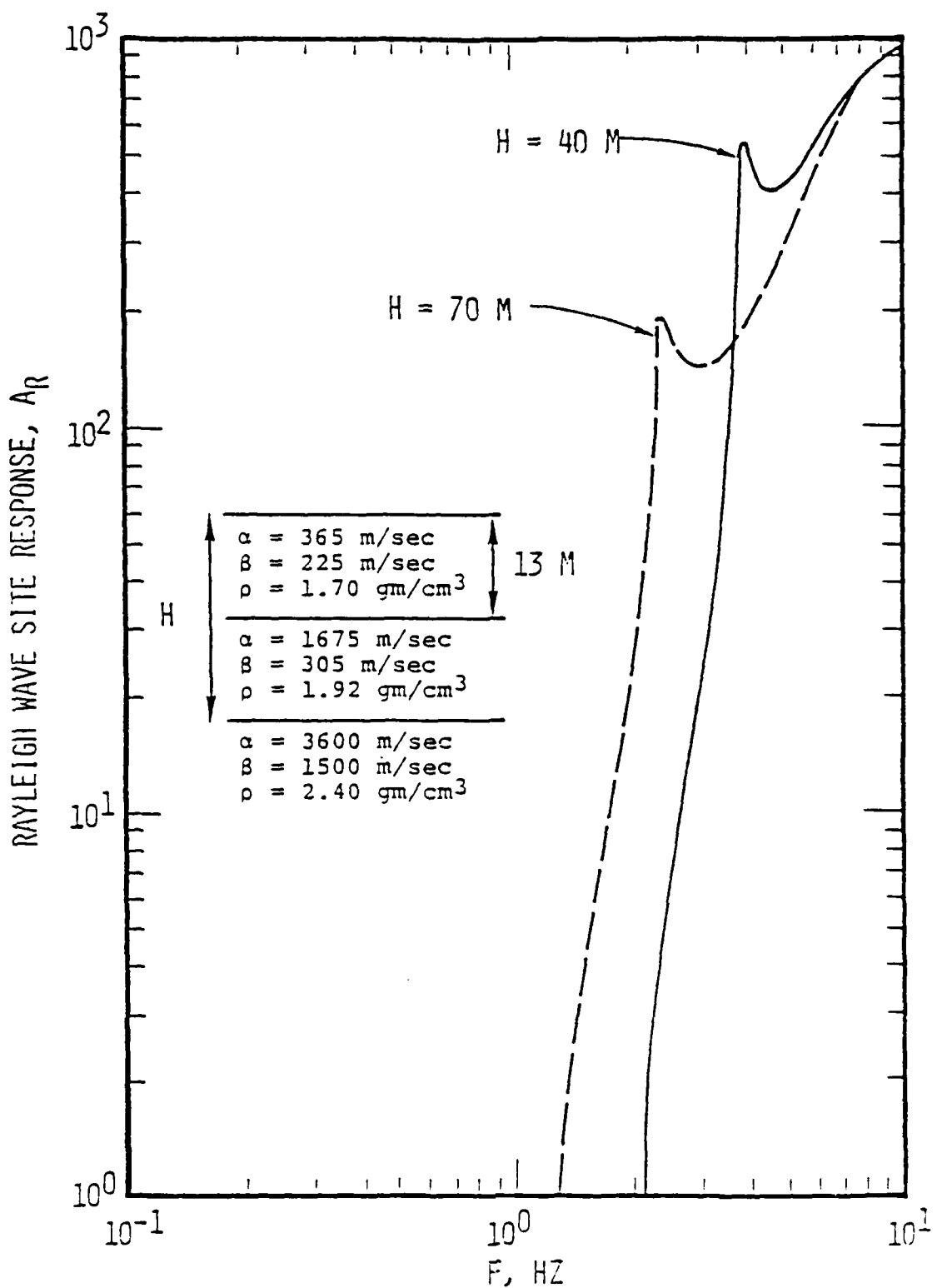


Figure 58. Fundamental mode Rayleigh wave site response functions for Misers Bluff II site.

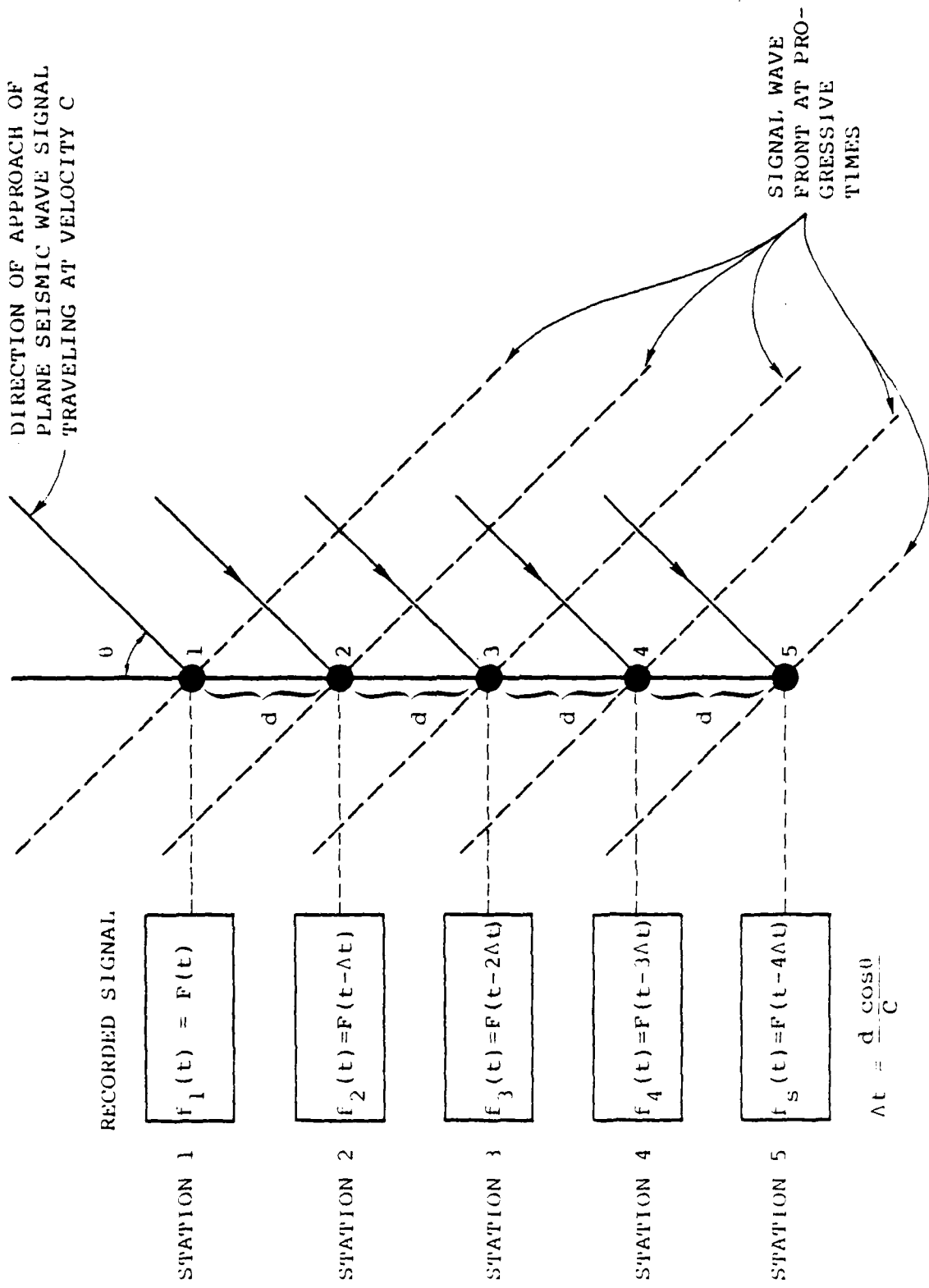


Figure 59. Schematic describing the behavior of a linear, uniformly-spaced array receiving plane seismic wave signals.

$$f_1(t) = F(t), f_2(t) = F(t-\Delta t), \dots, \\ f_n(t) = F(t - [n-1]\Delta t) \quad (3-2)$$

where  $\Delta t = d \cos\theta/c$ .

In the beam-forming process, recorded time histories from individual stations in the array are summed; however, prior to summing time delays or advances may be introduced to "steer" the array. Thus, for the array shown in Figure 59, advancing the time history recorded at station  $n$  by an amount  $(n-1)d \cos\theta/c$  and then summing causes the signals to be added in phase and thus "steers" the beam in the direction  $\theta$  from which the signal arrives. In general, a time advance  $\tau_n = (n-1)d \cos\theta_0/c$  for the linear array can be thought of as steering the beam in the direction  $\theta_0$  for signals of velocity,  $c$ .

A better understanding of how the process works can be obtained by considering the response of the array to harmonic wave motion arriving from direction  $\theta$ . We will assume a time advance given by  $\tau_n = (n-1)\Delta\tau$ , where  $\Delta\tau = d \cos\theta_0/c$ , is introduced at station  $n$  before the beam sum is formed. Taking the amplitude of the harmonic wave as  $A$ , the beam sum is:

$$\phi = Ae^{i\omega t} + Ae^{i\{\omega(t+\Delta\tau)-\omega\Delta t\}} + \dots \\ + Ae^{i\{\omega(t+[N-1]\Delta\tau)-\omega[N-1]\Delta t\}} \\ = Ae^{i\omega t} \sum_{n=0}^{N-1} e^{i n(\alpha-\beta)} \quad (3-3)$$

where  $N$  is the total number of stations in the array over which the summation is performed,  $\alpha \equiv \omega\Delta\tau = \omega d \cos\theta_0/c$  and  $\beta \equiv \omega\Delta t = \omega d \cos\theta/c$ . This sum can be rewritten so that:

$$\phi = A \left\{ \frac{\sin[N(\alpha-\beta)/2]}{\sin[(\alpha-\beta)/2]}\right\} e^{i(N-1)[(\alpha-\beta)/2]} e^{i\omega t}. \quad (3-4)$$

The term in braces,  $\frac{\sin[N(\alpha-\beta)/2]}{\sin[(\alpha-\beta)/2]}$ , corresponds to the ratio of the amplitude of the beam sum to the signal amplitude at a single station while the term  $e^{i(N-1)[(\alpha-\beta)/2]}$  corresponds to the change in phase of the beam sum relative to the signal at the first detector.

In the case of the MBII array, some additional complexity is introduced into the problem by the fact that we are dealing with horizontal components of motion. The problem is simplified by considering signals for which the wave particle motion is in the plane of propagation separate from signals for which the particle motion is perpendicular to the plane of propagation. For particle motion in the plane of propagation (which is of prime interest in the current study), the along-the-beam response for an array steered in the direction  $\theta_0$  can be written as:

$$\phi_L = A_L(\theta_0) \frac{\sin[N(\alpha-\beta)/2]}{\sin[(\alpha-\beta)/2]} e^{i(N-1)[(\alpha-\beta)/2]} e^{i\omega t} \quad (3-5)$$

where

$$A_L(\theta_0) = A_R \cos\theta_0 - A_T \sin\theta_0 \quad (3-6)$$

where  $A_R$  and  $A_T$  are the radial and transverse components of the recorded ground motion. (The term  $A_L(\theta_0)$  is present in the amplitude expression at each station and has been factored out of the sum to obtain Equation (3-5).) The radial component of motion,  $A_R$ , is along the line of stations and the transverse component,  $A_T$ , is perpendicular to that line, so that

$$\begin{aligned} A_R &= A_H \cos\theta \\ A_T &= -A_H \sin\theta \end{aligned} \quad (3-7)$$

where  $A_H$  is the amplitude of the horizontal component in the plane of propagation for wave motion propagating in direction  $\theta$  - i.e.,  $A_H$  is the resultant of  $A_R$  and  $A_T$ . Substituting in

Equation (3-6),

$$\begin{aligned} A_L(\theta_0) &= A_H \cos \theta \cos \theta_0 + A_H \sin \theta \sin \theta_0 \\ &= A_H \cos(\theta - \theta_0) \end{aligned} \quad (3-8)$$

So:

$$\phi_L = A_H \cos(\theta - \theta_0) \left| \frac{\sin[N(\alpha-\beta)/2]}{\sin[(\alpha-\beta)/2]} \right| e^{i(N-1)[(\alpha-\beta)/2]} e^{i\omega t}. \quad (3-9)$$

Then the ratio of the amplitude of the beam sum to the amplitude of the horizontal component at a single station for motion in the plane of propagation is just the product of the original directivity function for the array (the term in braces) and a factor which projects the motion into the direction in which the beam is steered. Similar expressions can be derived for the perpendicular response of the beam sum to signals with particle motion in the plane of propagation and for the responses of the beam sum to signals having transverse particle motion.

Figure 60 shows the predicted response of the MBII-1 array to harmonic motion with a frequency of 4 Hz and a velocity of 600 m/sec for particle motion polarized in the direction of propagation of a signal from  $\theta = 0^\circ$ . The response is shown as a function of the direction in which the beam is steered,  $\theta_0$ . The response is seen to consist of a broad main lobe and some lesser side lobes. In this case, the response is symmetric about the line of stations; for signals propagating in other directions the symmetry normally associated with the directivity of a linear array is lost because of the factor projecting the motion onto the steering direction, as will be seen below.

In applying the beam-steering process to the MBII-1 array, the recorded signals were not harmonic but consisted of transients of, at most, a few cycles. Applying an eighth-order narrow band-pass filter to the motion makes the time

histories appear more nearly harmonic and, thus, should make the observed response of the MBII-1 array more closely match the theoretical response shown in Figure 60. Similar procedures were used in studying the reverberations of seismic waves in Las Vegas Valley as noted above.

For MBII-1 filter center frequencies of 4 Hz and 2 Hz were selected. The phase velocities used to compute delay times between stations were varied over a range from about 0.2 km/sec to 1.4 km/sec which includes the range of phase velocities consistent with dispersion curves calculated for the theoretical model of the MBII area shown above in Figure 26. Figures 61 and 62 show the results of applying this process to the MBII-1 data for a frequency of 4 Hz and a phase velocity of 600 m/sec (the velocity which maximized the beam amplitude). The time histories shown represent motions along the direction in which the beam is steered; 1.5 seconds of "dead time" has been introduced at the start and finish of each time history to permit the required shifting of time histories in the beam-forming process. It can be seen that the combined effect of the velocity and frequency filters effectively suppresses the late-time reverberations and isolates the direct arriving 4 Hz component of the motion. It is interesting to note, however, that the maximum array response occurs at an azimuth (measured clockwise from the source azimuth) of between 20 and 40 degrees. This can also be seen in Figure 60 where we compare the observed response pattern of the MBII-1 array with its theoretical response to harmonic motion arriving from  $\theta = 0^\circ$ . The observed data points correspond to amplitudes of the peak motion on each record which have been normalized by dividing by the maximum array response. Clearly, the observed peak motion does not appear to be arriving along the shot/station line. Figure 63 shows a similar comparison for harmonic motion arriving from  $\theta = 30^\circ$ . The observed pattern in peak amplitudes

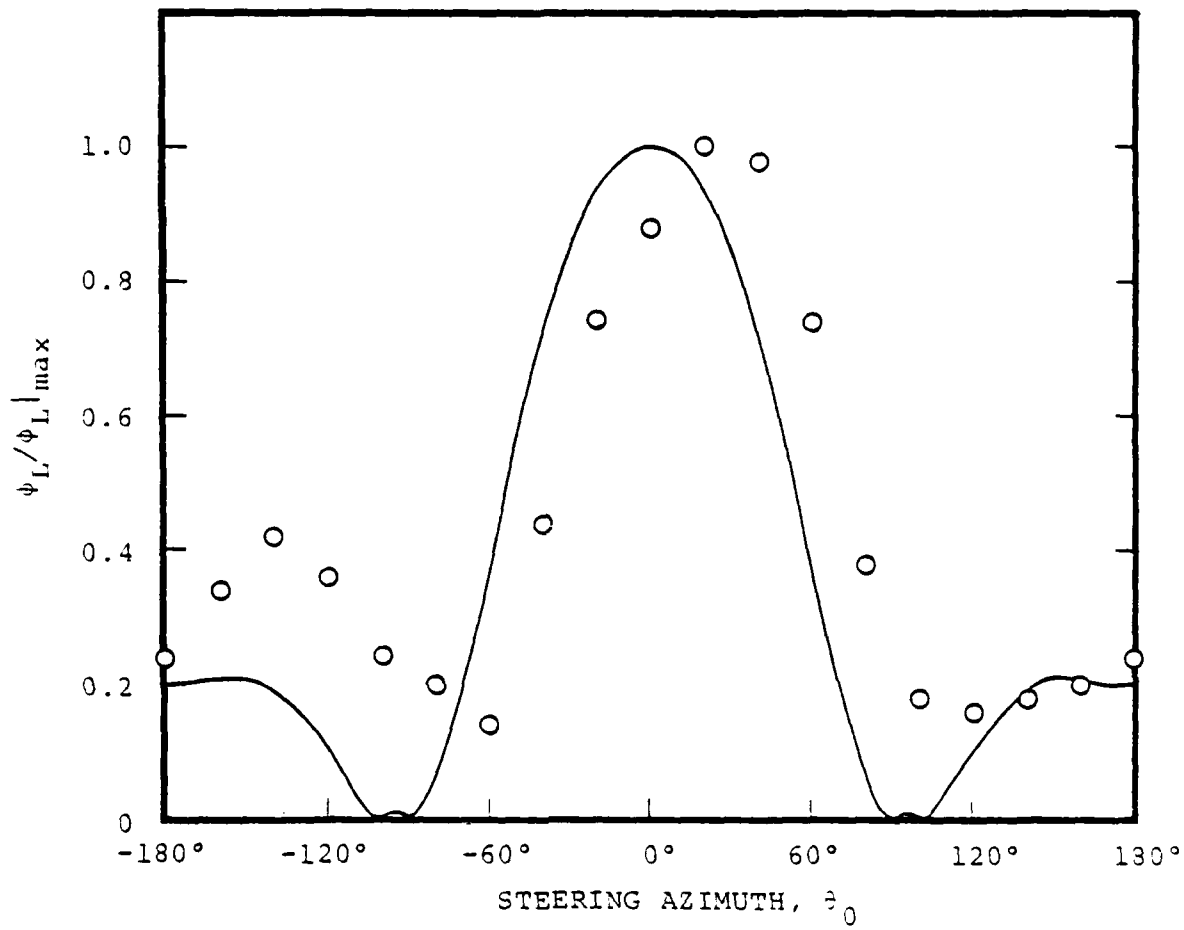


Figure 60. Response of the MBII-1 array to 4 Hz signals with phase velocity  $c = 600$  m/sec. Solid line shows theoretical response to harmonic waves arriving from  $\theta = 0^\circ$ . Circles indicate observed response to the filter, beam-steering process with observations normalized to the maximum predicted response.

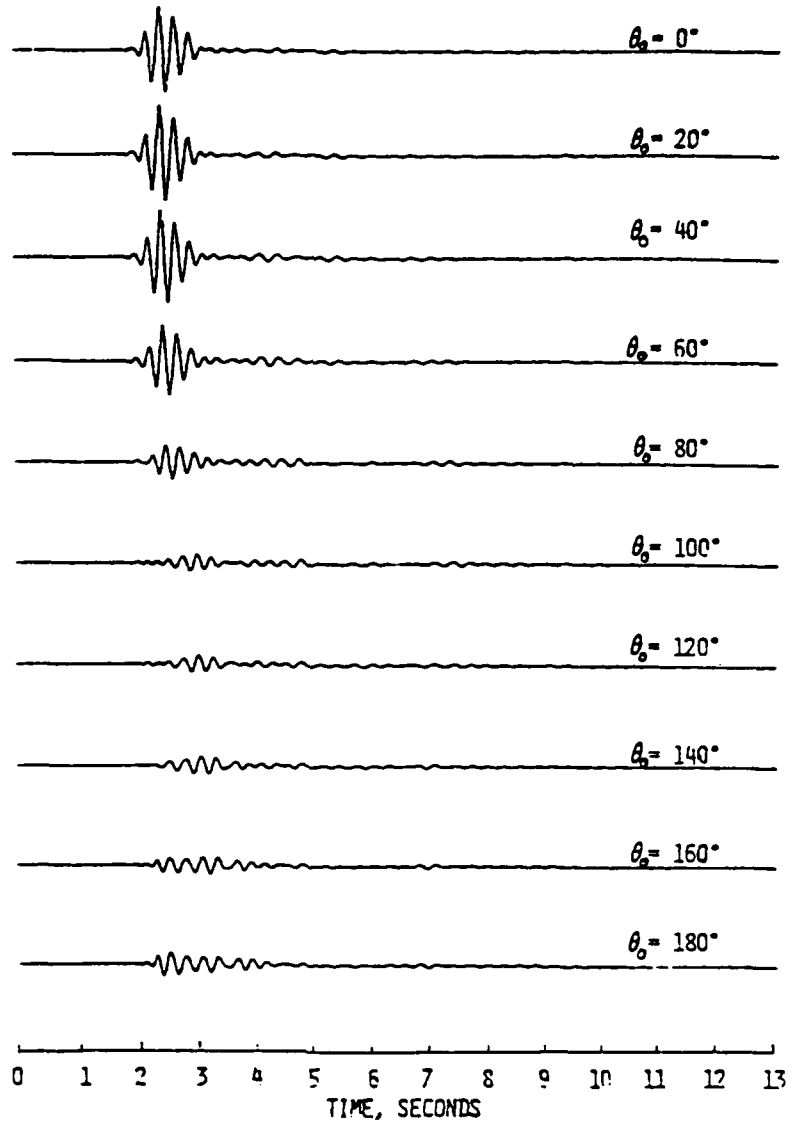


Figure 61. MBII-1 filtered beam  $c = 600$  m/sec,  $f_c = 4.0$  Hz.

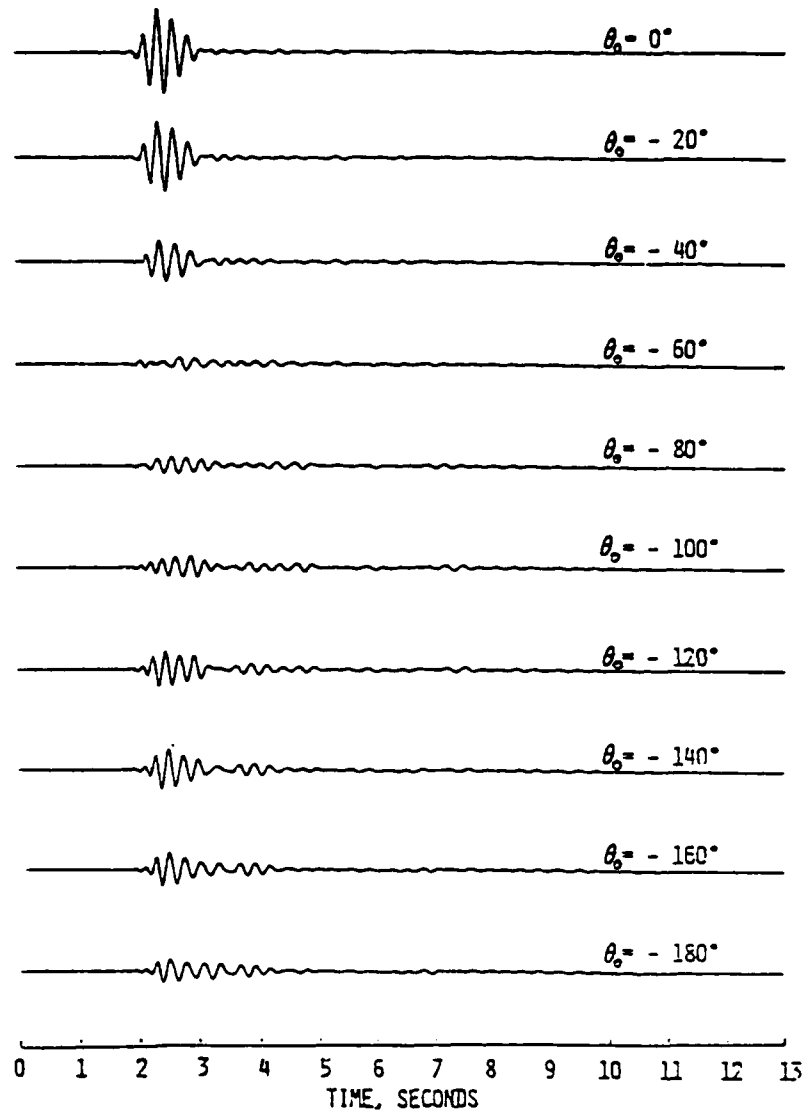


Figure 62. MBII-1 filtered beam,  $c = 600$  m/sec,  $\xi_c = 4.0$  Hz.

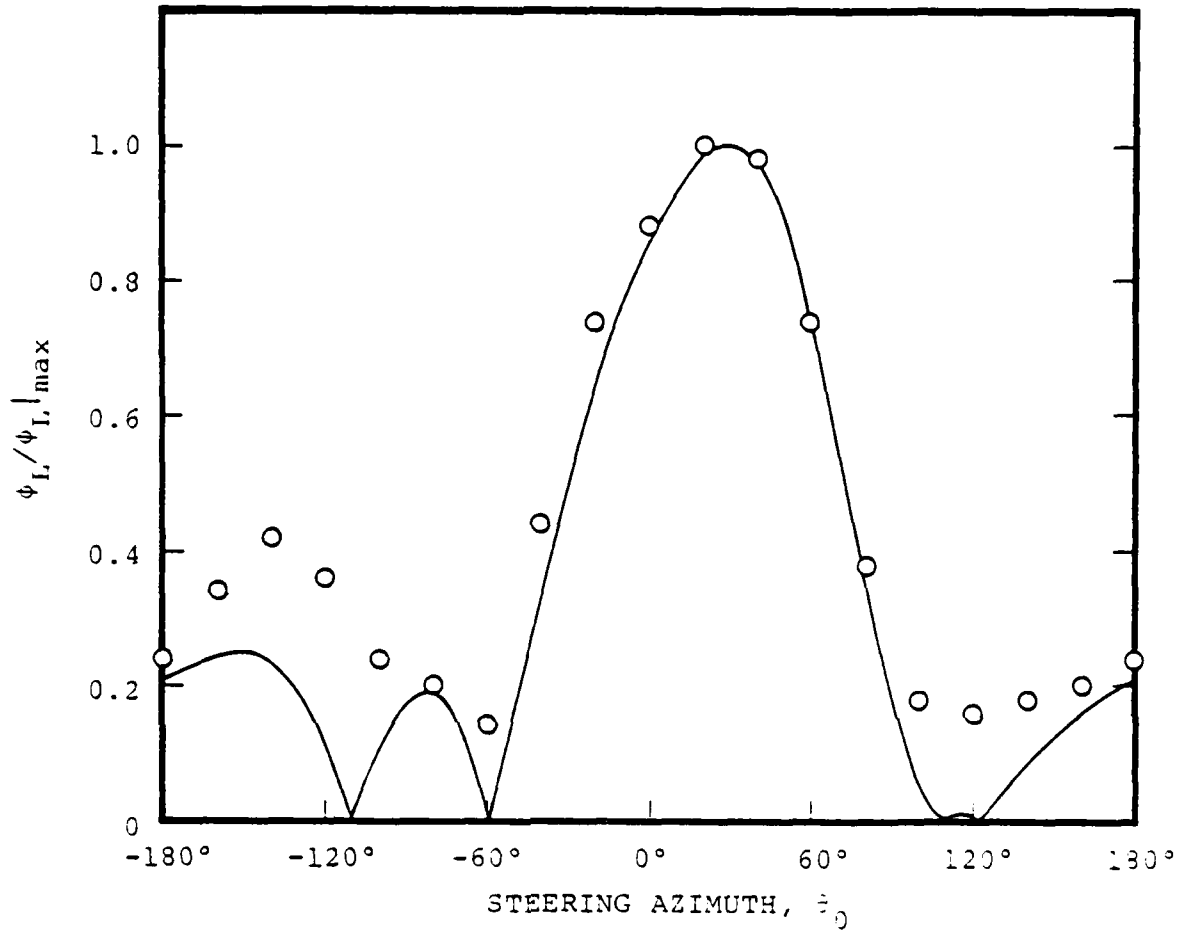


Figure 63. Response of the MBII-1 array to 4 Hz signals with phase velocity  $c = 600$  m/sec. Solid line shows theoretical response to harmonic waves arriving from  $\theta = 30^\circ$ . Circles indicate observed response to the filter, beam-steering process with observations normalized to the maximum predicted response.

of the steered MBII-1 array data is found to match the theoretical pattern much more closely in the latter case.

Two possible explanations for this puzzling observation have been considered. The first is that the primary surface wave energy has been ducted around the previously referenced high point in the bedrock topography (c.f., Figure 55) and is, in fact, approaching from well off the source azimuth. The other possibility is that the effect is an artifact of the data processing resulting from the fact that the observed transverse component of motion is not zero, as assumed in the formulation of the simple model. That is, it has been shown (Murphy and Bennett, 1979) that adding an in-phase transverse component of motion to the direct arriving Rayleigh wave signal can lead to a directional response very similar to that observed in Figures 61 and 62. It is not clear at the present time which of these interpretations is correct. We have conducted some preliminary particle motion studies in an attempt to better discern the nature of this motion. Figure 64 shows particle motion diagrams for one second of time of the signal causing the peak motion as recorded at station 280 filtered through a 4 Hz band-pass filter. The motions are shown for a horizontal (R-T) plane and for a vertical (R-Z) plane. The orientation of the R-Z plane was varied between an azimuth of  $-20^\circ$  and  $+60^\circ$  (relative to the shot/station line) in  $20^\circ$  steps to produce the diagrams. We see from the diagrams in the R-T plane that the transverse component of the overall motion is minimized (though it is still fairly large) when the R-Z plane is at an azimuth between  $20^\circ$  and  $40^\circ$ . The particle motion in the R-Z plane at this azimuth is seen to consist of prograde and retrograde elliptical motion probably associated with Rayleigh waves. The corresponding particle motion in the R-Z plane for an azimuth of  $0^\circ$  appears more complex and is less easily identifiable as Rayleigh type motion. This tends to favor the first

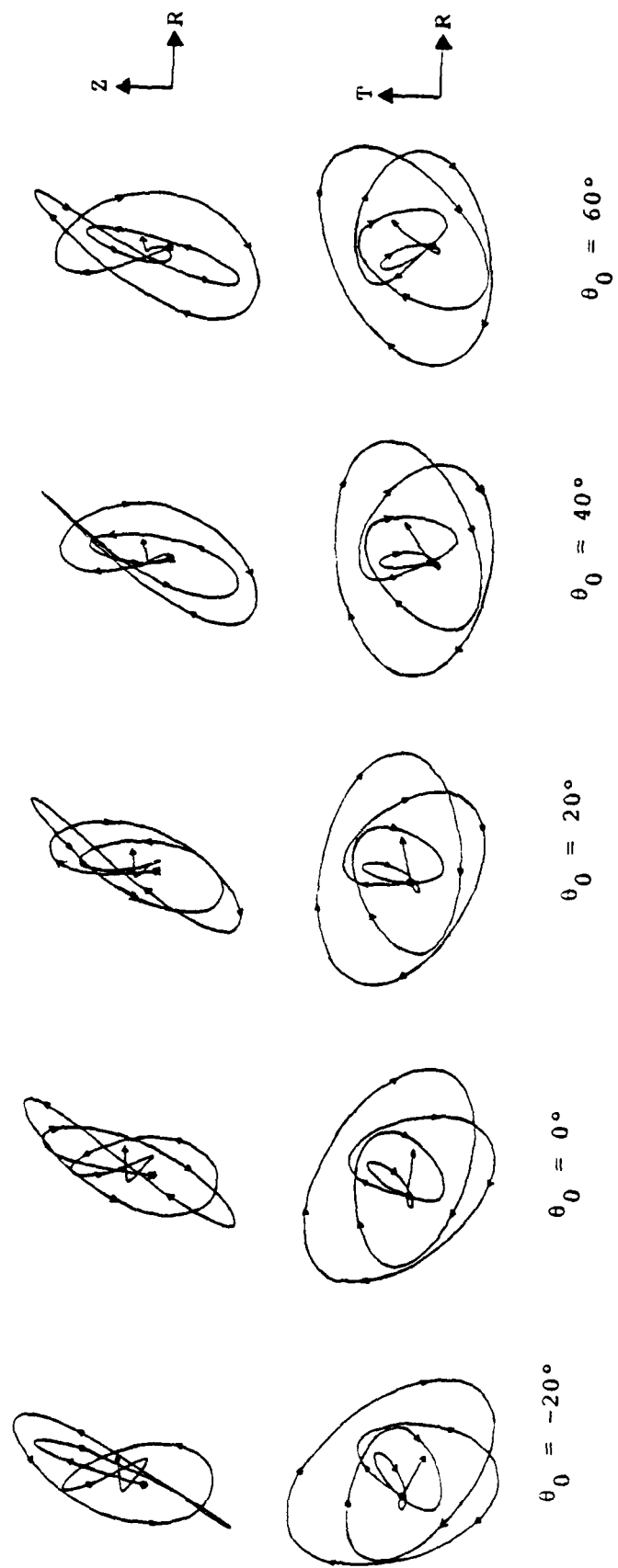


Figure 64.

Ground motion hodograph for a frequency of 4 Hz during the one second time window surrounding the peak displacement; MBII-1,  $R = 280$  m. Motion in R-Z plane, at top, and in R-T plane, at bottom, for different orientations,  $\theta_0$ , of the R-Z plane.

explanation for the observed behavior (i.e., the "direct" signal is arriving from well off the source azimuth). We performed similar analyses on several later time segments from individual records and also beam-summed time histories and found elliptical particle motions typical of Rayleigh waves.

Given that the direct arrival has been isolated, it remains to demonstrate that it is a Rayleigh wave. For this purpose, the MBII-1 event has been simulated by computing the Rayleigh wave component of the ground motion induced by the airblast acting on the surface outside the region of strong nonlinear response (i.e., the crater) (Murphy, 1979). For this purpose, the subsurface geologic model shown in Figure 58 was used with  $H = 40$  m.

Figure 65 shows a comparison of the MBII-1 observed filtered beam output with the theoretical, radial component, fundamental mode Rayleigh wave displacement at a range of 300 m. The agreement between the computed and observed motion is excellent, confirming that the observed motion is predominantly an airblast-induced, fundamental mode Rayleigh wave.

Due to the fact that this array was designed primarily for 4 Hz, 600 m/sec phase velocity signals, it is not well suited for separating out the late-arriving, lower frequency signals. For this reason, the higher velocity (1000 m/sec), lower frequency (2 Hz) beam was less successful in decomposing the recorded motion. This is illustrated in Figure 66 which shows the filter outputs over the azimuth range from 0 to 180 degrees. Several secondary bursts of energy are evident, but they are spread out over such a wide range in azimuth that a definitive identification of their origin is not possible. This lack of resolution is primarily due to the fact that the array aperture is too small with respect to the characteristic wavelengths of the secondary signal, as shown by Murphy and Bennett (1979) using synthetic seismograms.

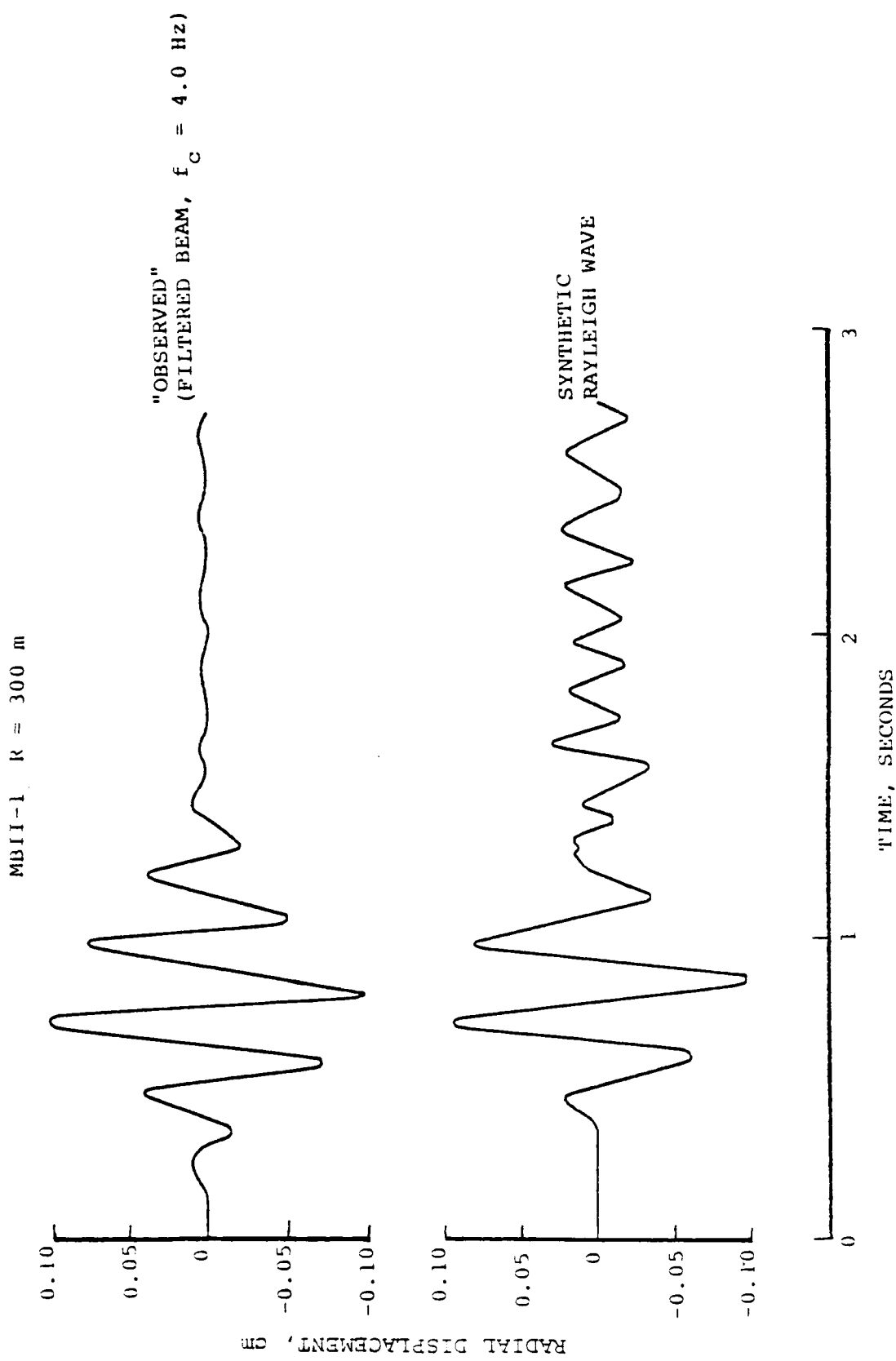


Figure 65. Comparison of theoretical and observed displacements; MBII-1,  $R = 300$  m.

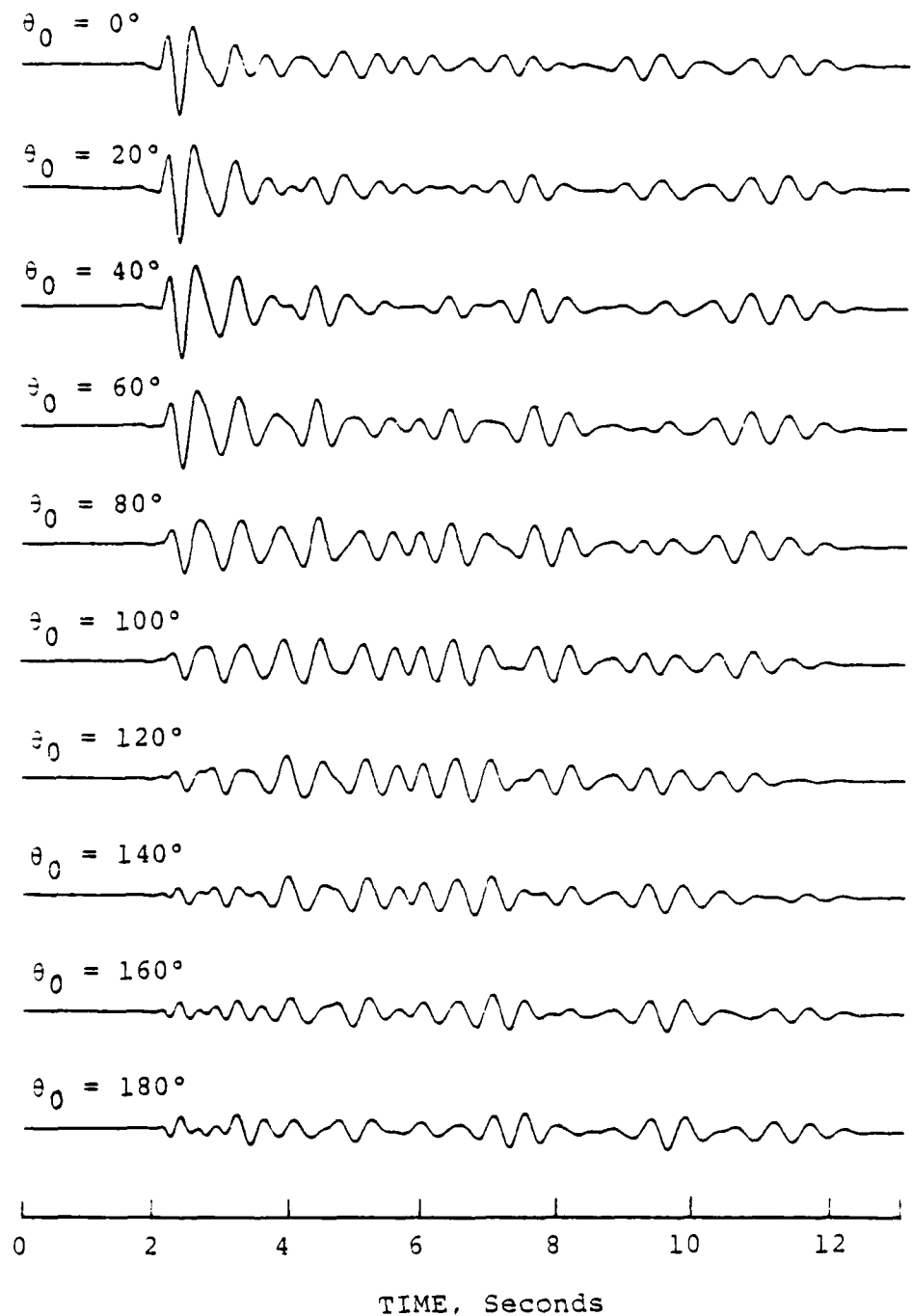


Figure 66. MBII-1 filtered beam,  $c = 1000$  m/sec,  $f_c = 2$  Hz.

Considering this cause for the lack of resolution of the lower-frequency, higher-velocity seismic waves found in the MBII-1 data, somewhat better results could be anticipated for the MBII-2 explosion because of the larger array aperture (150 m versus 100 m for MBII-1). To test the frequency content of the signals from the MBII-2 explosion, we processed the ground motion recorded at a range of 420 m using a series of eighth-order, narrow band-pass filters. The center frequencies were varied between 1 Hz and 5 Hz. The results are shown in Figures 67 through 69. Although some lower-frequency energy can be seen on the records, the signal is generally concentrated in a fairly narrow frequency band surrounding 3 Hz. Furthermore, any signals occurring after about the first 4 to 5 seconds of record appear to be significantly lower in amplitude. The only exception seems to be a 2-3 Hz signal which shows up mainly on the tangential record about 7 seconds after shot time; and even this is a factor of 6 lower in amplitude than the direct motion. This clustering of signals near the start of the record and in a rather narrow range of frequencies is somewhat different from similar computations for MBII-1 (c.f., Figure 57) and makes signal resolution particularly difficult.

We applied the same beam-steering, frequency-filtering procedure to the MBII-2 array data as that used for MBII-1. Center frequencies were again set at 2 Hz and 4 Hz and the velocities used to compute delay times were varied over a range appropriate to the velocity structure of the MBII site. Figures 70 and 71 show the results of applying the beam-steering process for a filter frequency of 4 Hz and a phase velocity of 600 m/sec; the records show the along-the-beam component of motion. In these figures one second of "dead time" has been added at the start and finish of each time

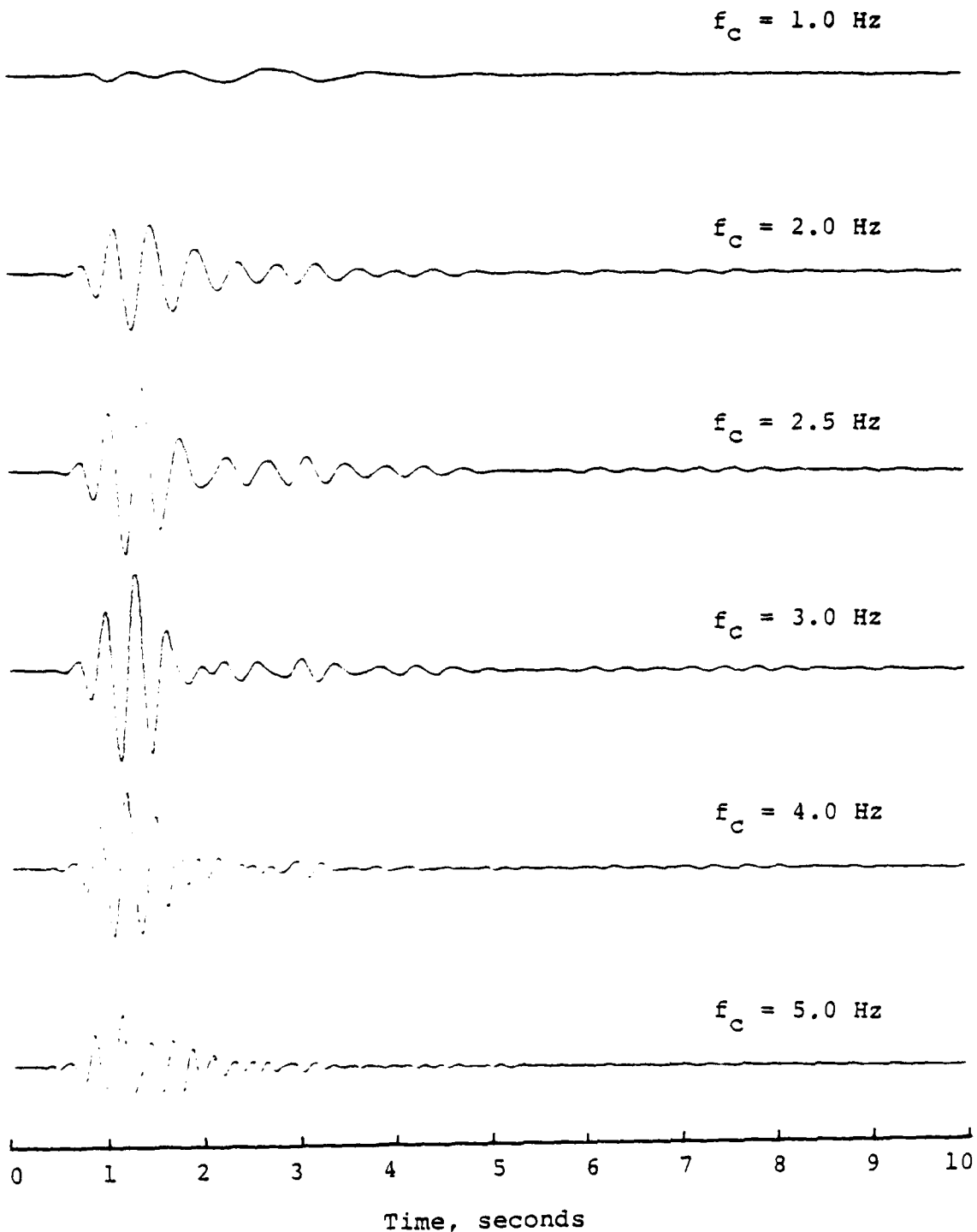


Figure 67. Comparison of eighth-order bandpass filtered radial displacements at center frequencies,  $f_c$ , of 1.0, 2.0, 2.5, 3.0, 4.0 and 5.0 Hz; MBII-2,  $R = 420 \text{ m}$ .

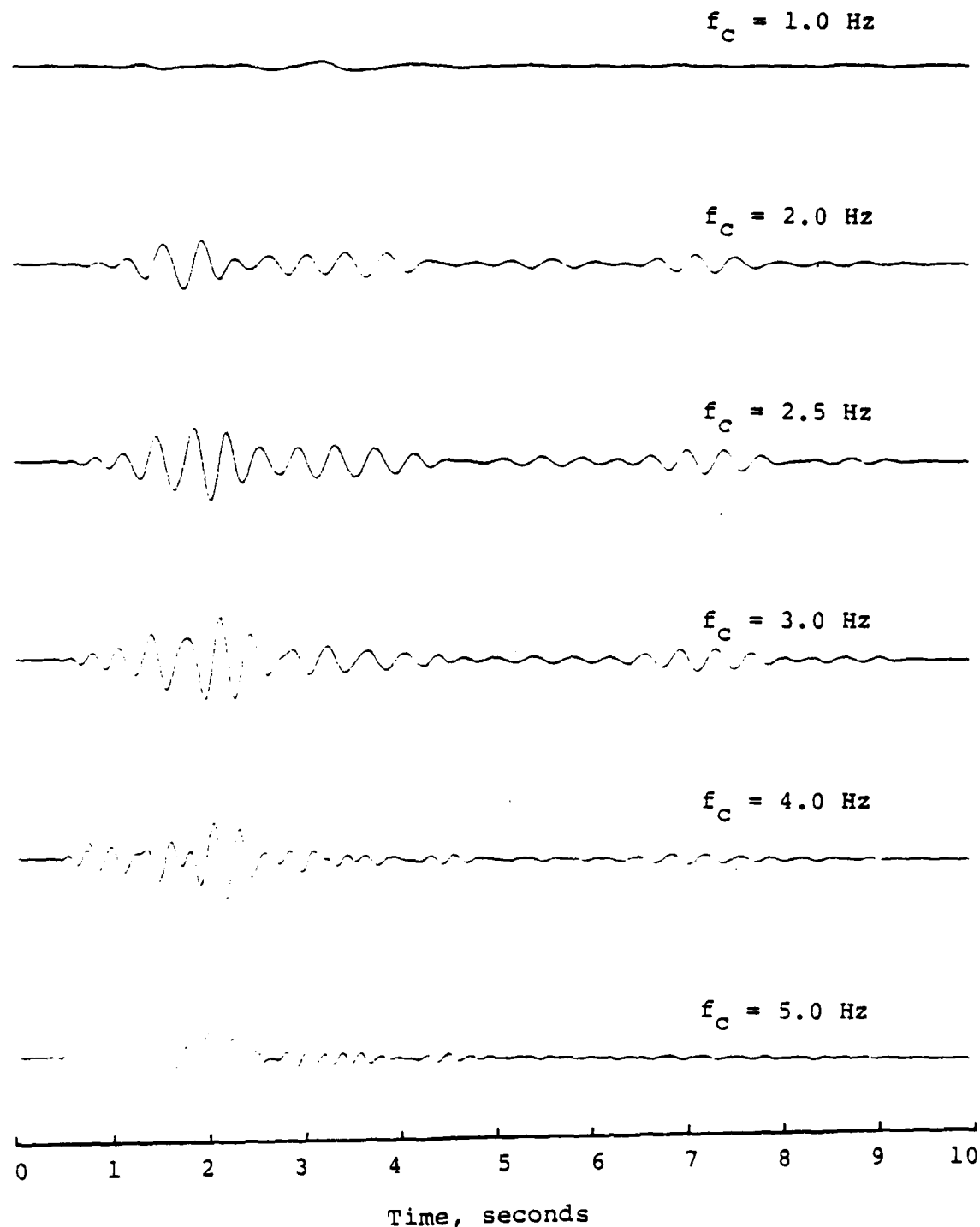


Figure 68. Comparison of eighth-order bandpass filtered tangential displacements at center frequencies,  $f_c$ , of 1.0, 2.0, 2.5, 3.0, 4.0 and 5.0 Hz; MBII-2,  $R = 420 \text{ m.}$

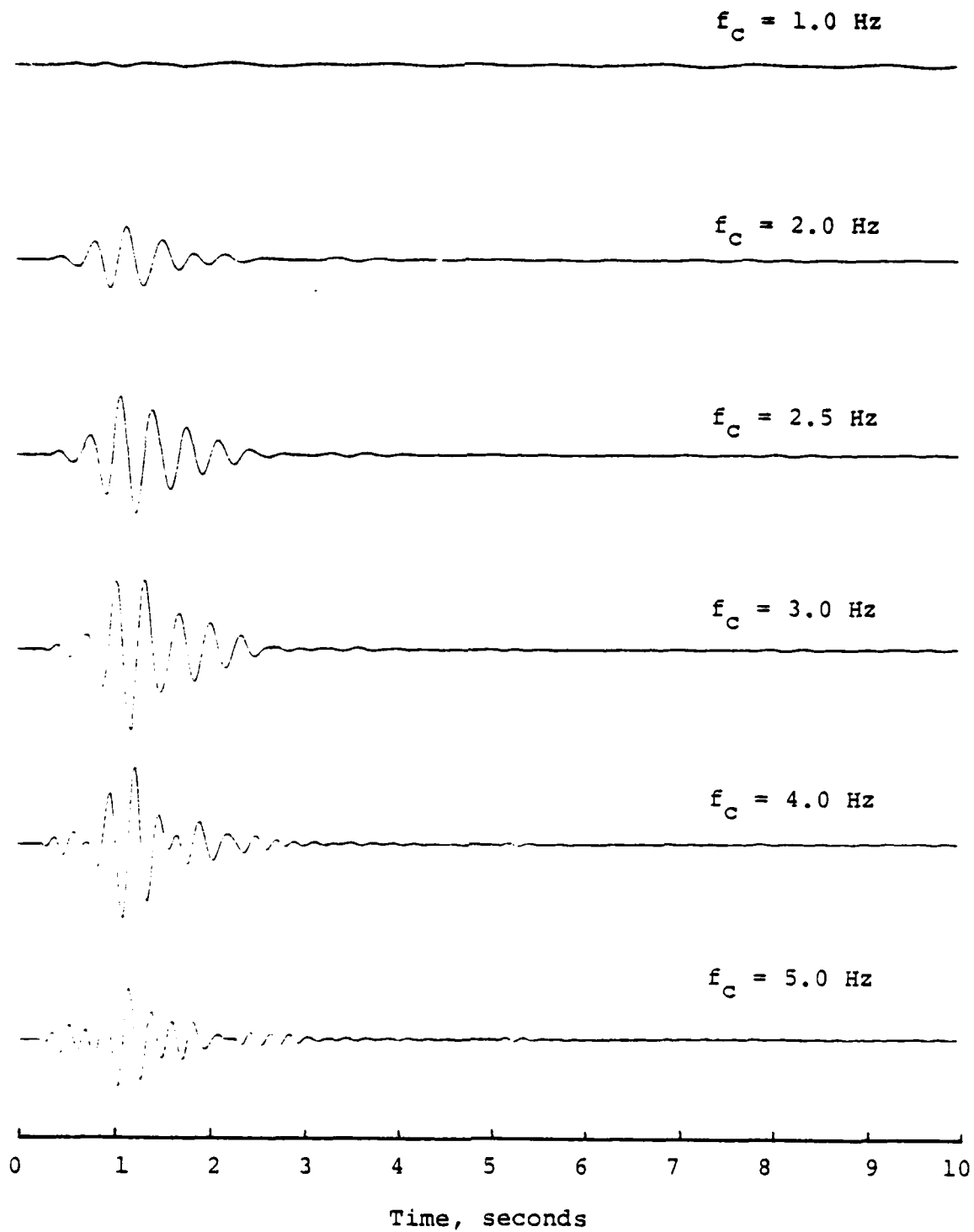


Figure 69. Comparison of eighth-order bandpass filtered vertical displacements at center frequencies,  $f_c$ , of 1.0, 2.0, 2.5, 3.0, 4.0 and 5.0 Hz; MBII-2,  $R = 420 \text{ m}$ .

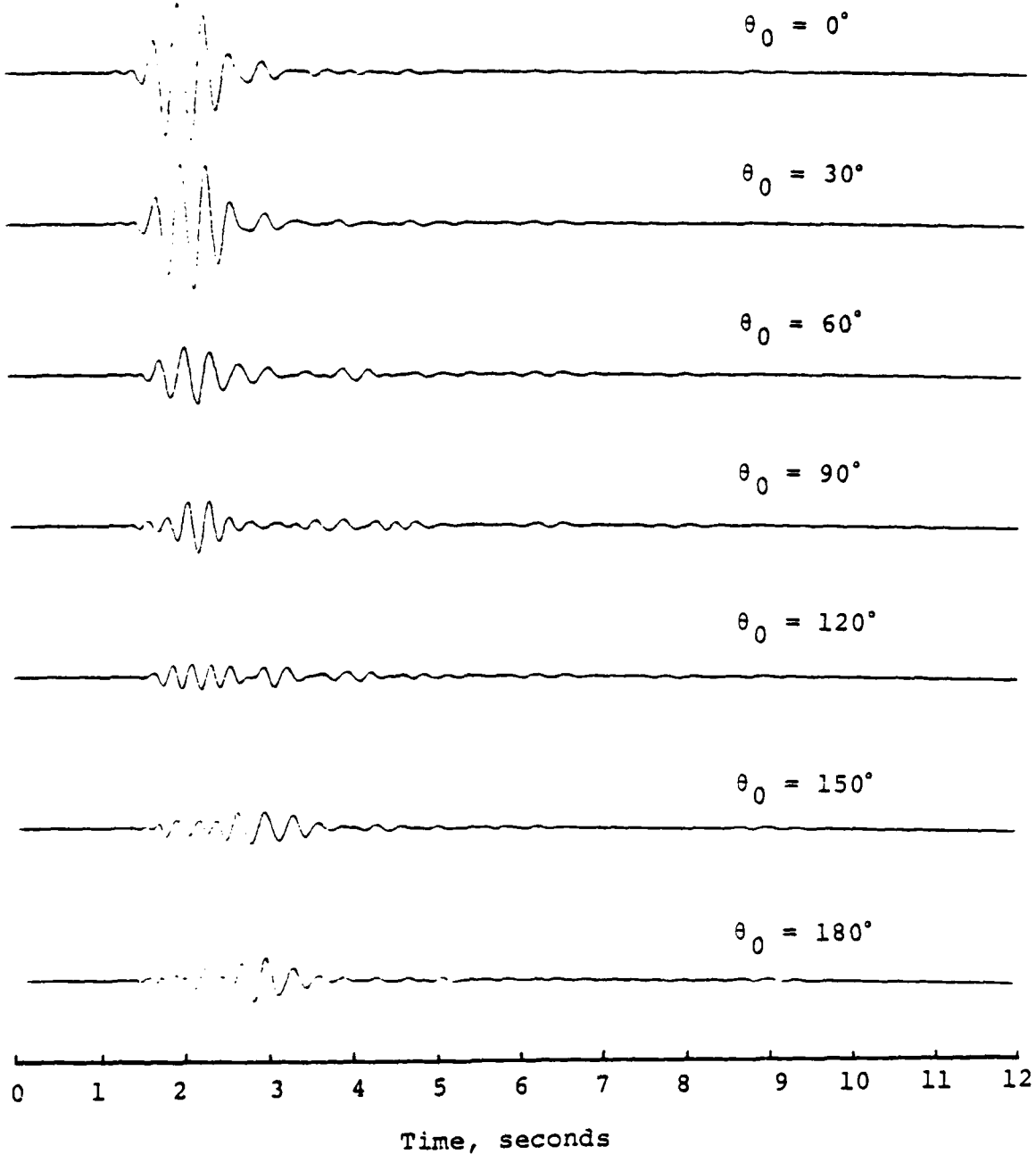


Figure 70. MBII-2 filtered beam,  $c = 600$  m/sec,  $f_c = 4$  Hz.

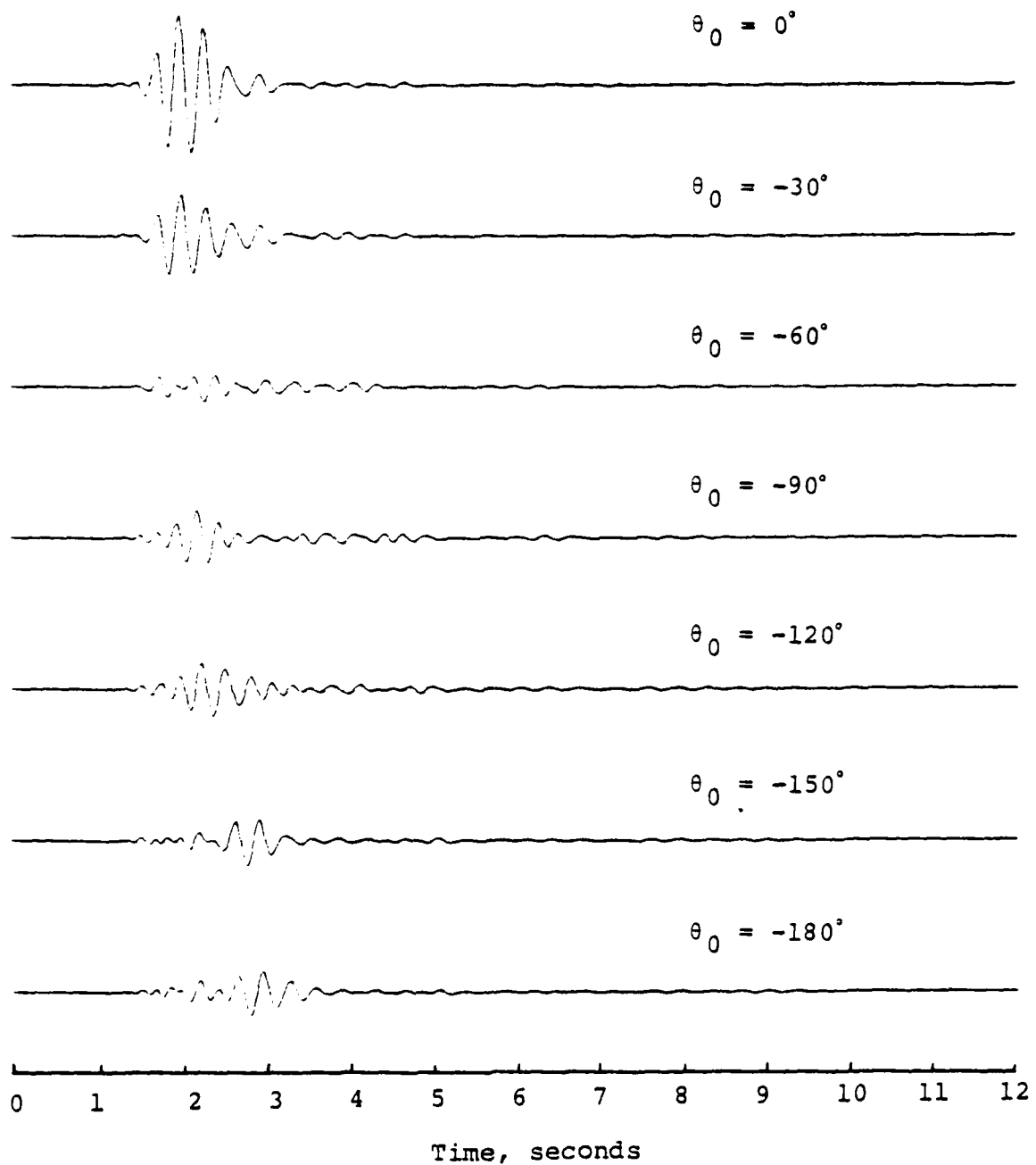


Figure 71. MBII-2 filtered beam,  $c = 600$  m/sec,  $f_c = 4$  Hz.

history to allow for the shifting involved in the process. As expected, prominent signals cluster in the first half of the record; nevertheless, a few distinct phases seem to be identifiable. The dominant signal along the shot/station azimuth, which corresponds to the direct Rayleigh wave, is again maximized at a velocity near 600 m/sec. In addition, a rather prominent phase (delayed about 1 second relative to the direct Rayleigh wave) appears to be traversing the array from an azimuth of 180°. This is also apparent in the response pattern of the array shown in Figure 72. Comparing the observed peak response of the MBII-2 array (approximated in this case as a six element, equally-spaced array) for 4 Hz waves arriving from  $\theta = 0^\circ$ , we see a close match out to  $\theta_0 = 70^\circ$  beyond which waves traveling back up the array cause divergence from the predicted pattern. The travel time of this phase, about 1.4 seconds relative to shot detonation (after removing a delay introduced by the filter), coupled with a propagation velocity near 600 m/sec indicate a total travel path length of about 800-900 m. This path length closely matches that for the direct Rayleigh wave reflected at the southern boundary of the valley back to the array.

Figures 73 and 74 show the results of beam-steering and filtering the MBII-2 data for a filter center frequency of 2 Hz. The figures show the along-the-beam array response for azimuths from 0° to 180° and phase velocities of 600 m/sec and 1000 m/sec. In this case, we note the presence of a relatively prolonged phase shortly after the direct Rayleigh wave which appears to be maximized near an azimuth of 60°. This phase was not apparent for the 4 Hz filtered data shown previously (c.f., Figure 70) and, considering its travel time and direction of approach, appears to be associated with Rayleigh waves reflected at the northeastern and eastern boundaries of the valley.

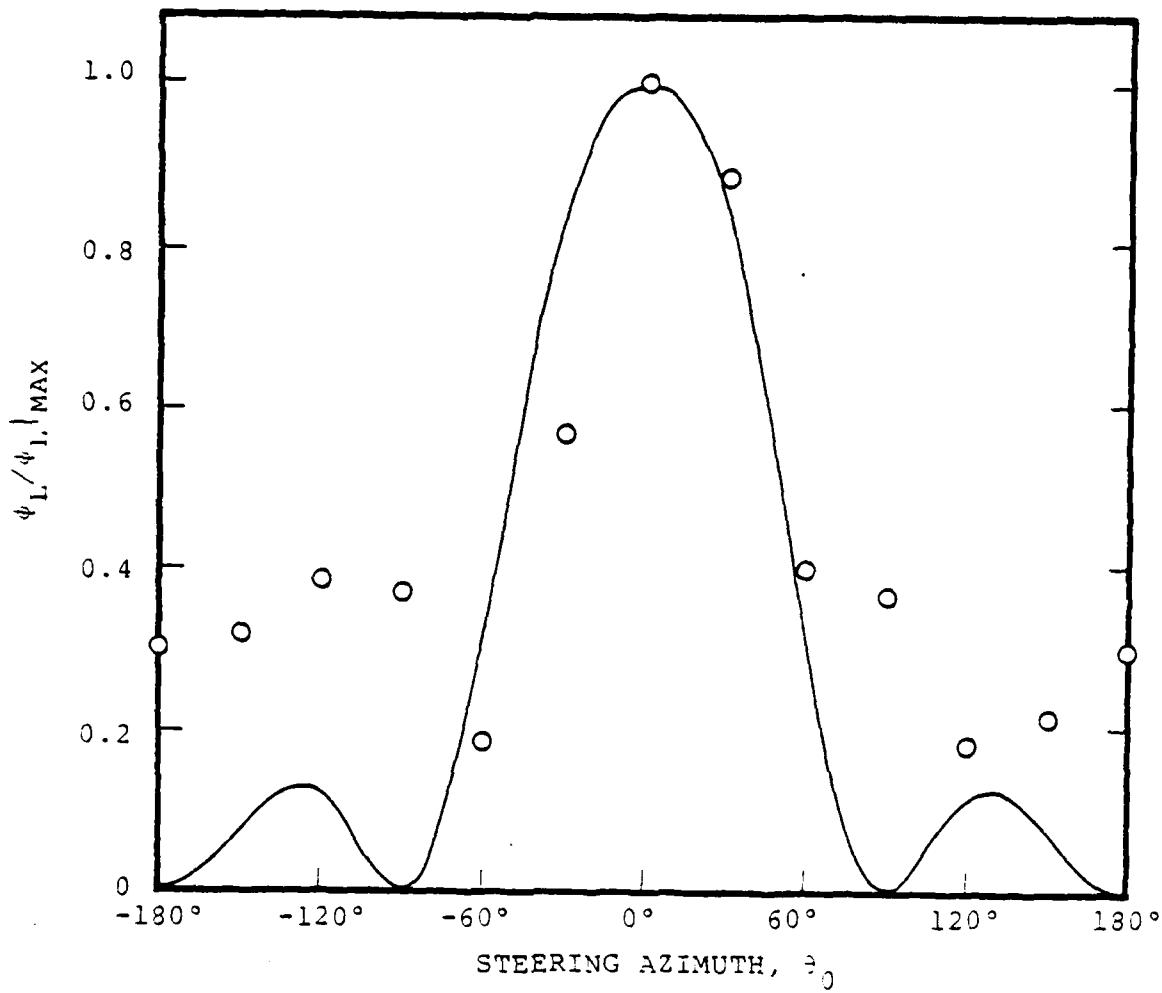


Figure 72. Response of the MBII-2 array to 4 Hz signals with phase velocity  $c = 600$  m/sec. Solid line shows theoretical response to harmonic waves arriving from  $\theta = 0^\circ$ . Circles indicate observed response to the filter, beam-steered process with observations normalized to the maximum predicted response.

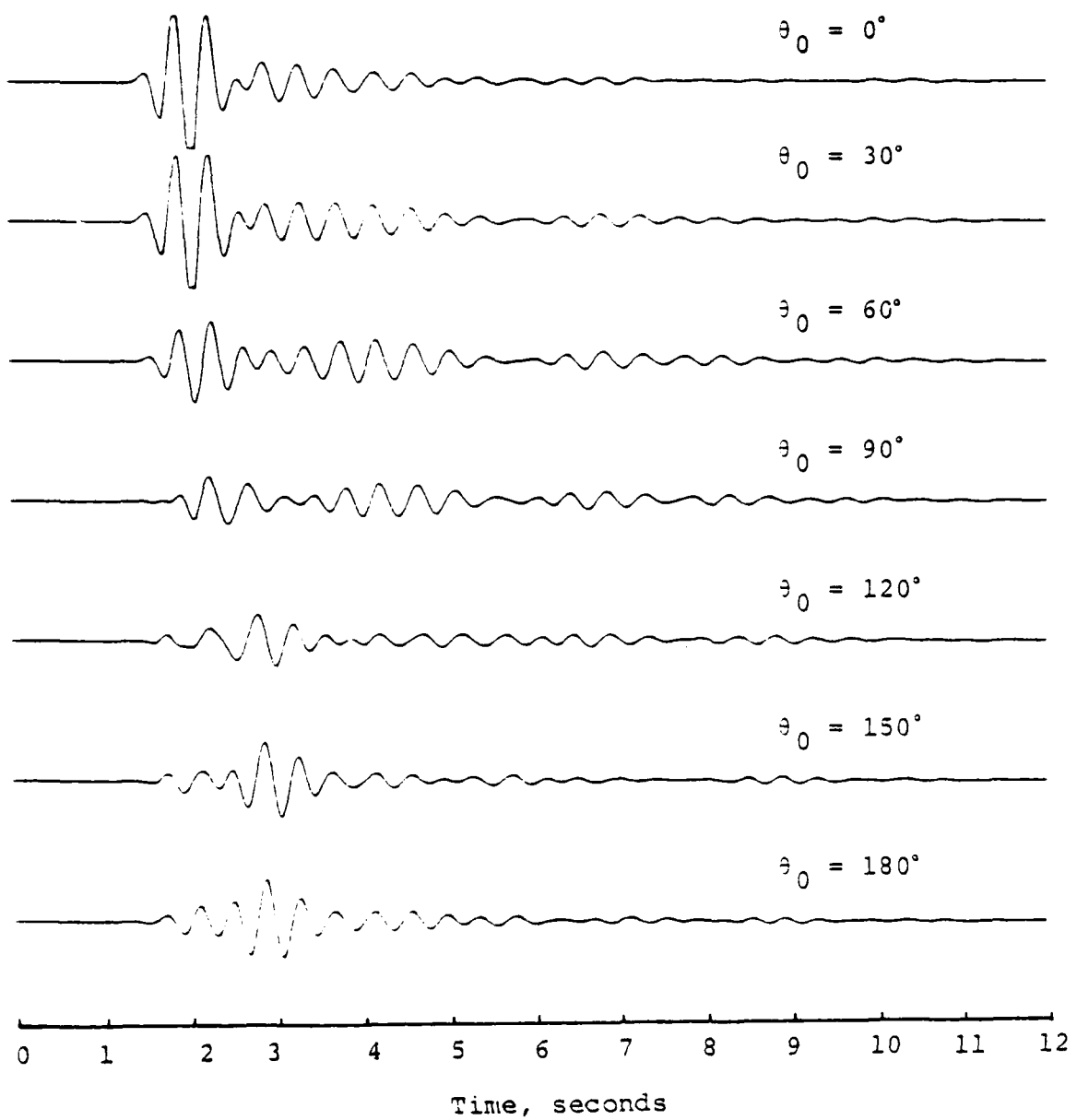


Figure 73. MBII-2 filtered beam,  $c = 600$  m/sec,  $f_c = 2$  Hz.

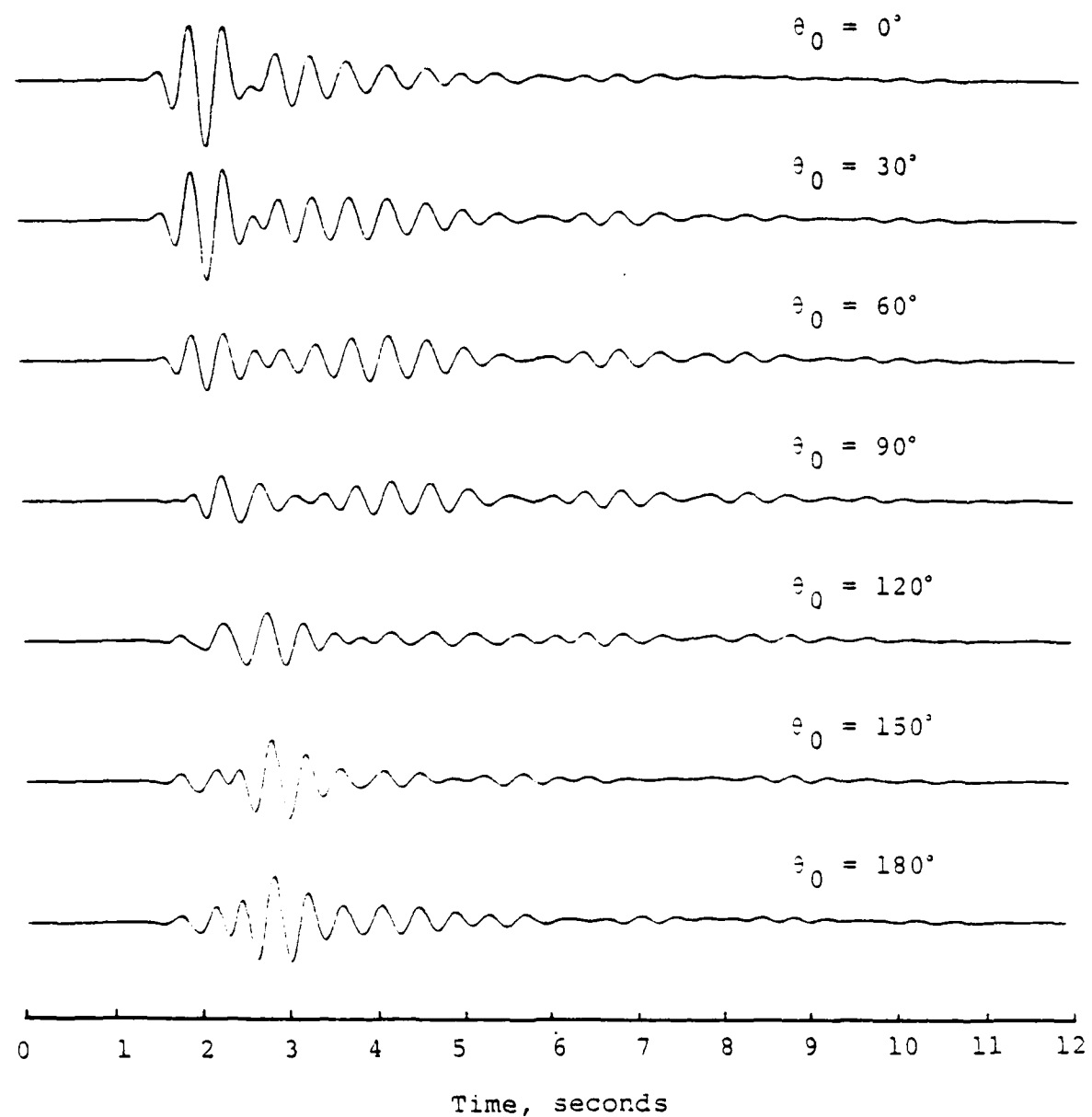
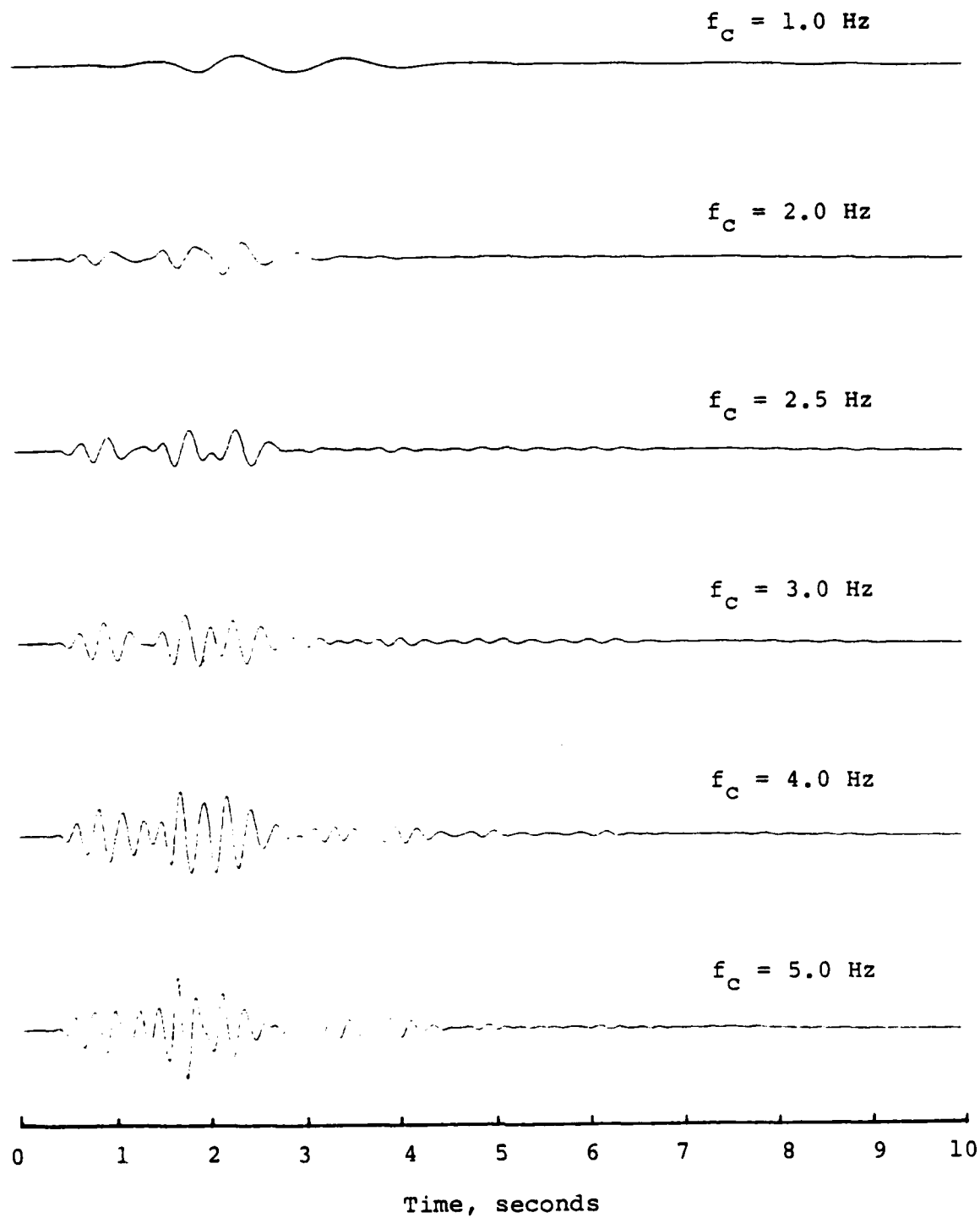


Figure 74. MBII-2 filtered beam,  $c = 1000$  m/sec,  $\xi_c = 2$  Hz.

For the MBII-2 data we again had difficulty resolving the direction of approach for many of the phases apparent on the records. The phases are generally seen to be spread over a fairly large range in azimuth. The larger aperture of the MBII-2 array appears to only marginally increase this resolution. This can be seen by comparing the theoretical harmonic responses for the MBII-1 and MBII-2 arrays in Figures 60 and 72. While the peak response for the MBII-2 array is somewhat higher and its side lobes are somewhat smaller, nulls occur in nearly the same positions and the main lobe is still fairly broad.

As a final element in processing the MBII-2 data, we considered the signals recorded at the station near the southern edge of the valley. Figures 75 and 76 show the results of passing the records from the uphole instruments through a series of band-pass filters centered at frequencies between 1 and 5 Hz. By comparing these figures to similar figures for the array station at a range of 420 m (c.f., Figures 67 through 69) several interesting features can be noted. The most obvious difference between the two sets of records is the change in frequency content; the records from the station near the valley edge show little sign of the 2-3 Hz energy so prominent in the array records. This may be associated with changes in the Rayleigh wave response of the instrument sites or possibly interference between direct and reflected Rayleigh waves occurring at the valley-edge station. One other feature of the records in Figures 75 and 76 is the presence of significant ground motion prior to the arrival of the direct Rayleigh wave. The mechanism for the generation of this wave motion is unclear but appears to have a source at the valley boundary. Though the amplitude of this motion is somewhat less at all frequencies than that of the direct Rayleigh wave, it may still be significant because of the increased duration of ground motion which it apparently produces.



**Figure 75.** Comparison of eighth-order bandpass filtered radial displacements at center frequencies,  $f_c$ , of 1.0, 2.0, 2.5, 3.0, 4.0 and 5.0 Hz; MBII-2,  $R = 650 \text{ m.}$

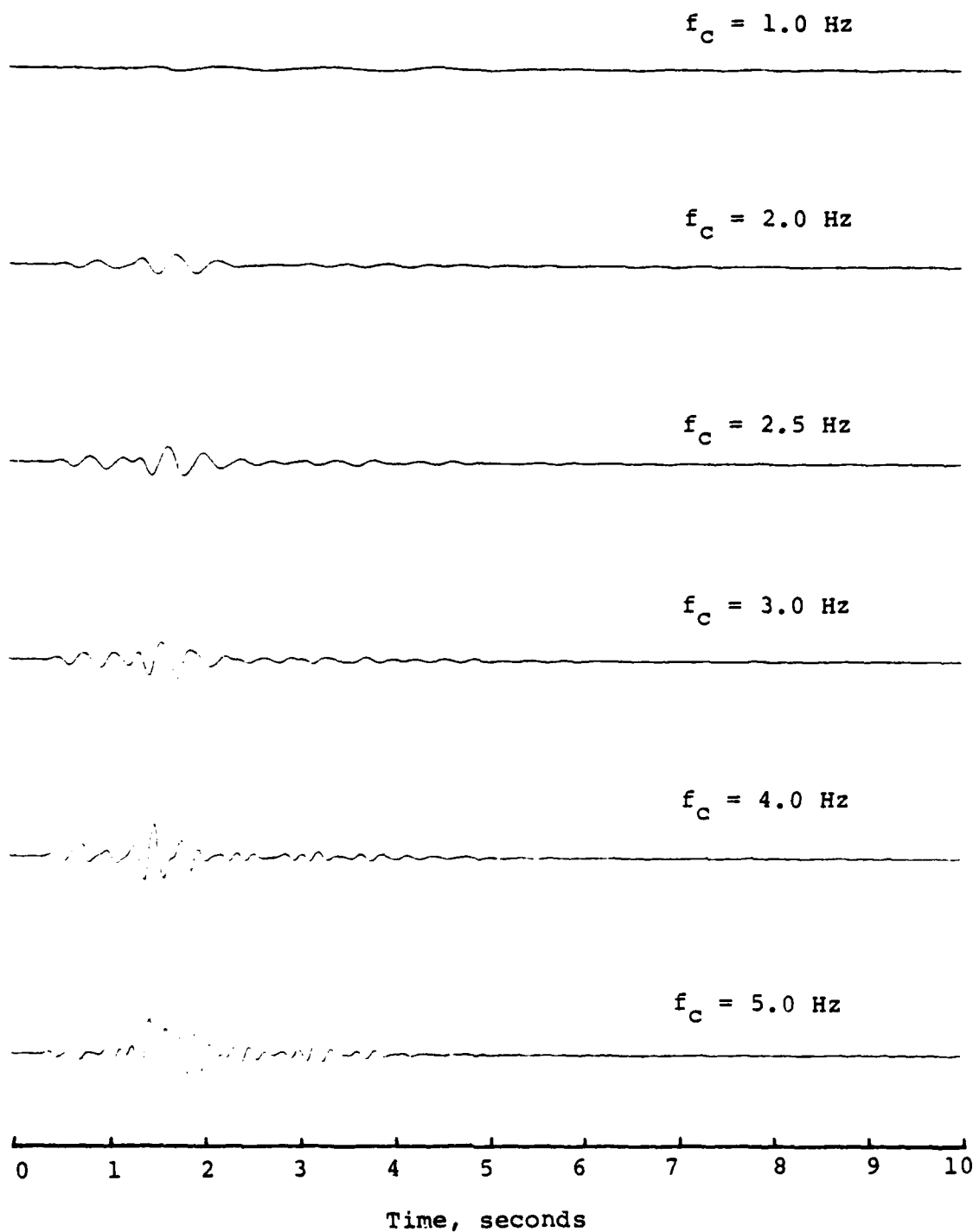


Figure 76. Comparison of eighth-order bandpass filtered vertical displacements at center frequencies,  $f_c$ , of 1.0, 2.0, 2.5, 3.0, 4.0 and 5.0 Hz; MBII-2,  $R = 650 \text{ m.}$

### 3.3.2 Discussion of Results

Of the results presented here for the Misers Bluff II valley reverberation experiment, one which appears most significant to MX siting considerations is the prolonged duration of ground motion observed at some stations for limited frequency ranges. The most obvious example of this is the 2 Hz filtered ground motion time history for the MBII-1 explosion shown in Figure 57. The amplitude of the 2 Hz motion on this record at a time 10 seconds after detonation is still almost half as large as the maximum motion on the record. Such prolonged duration is also apparent on the beam-steered data from the MBII-1 experiment shown in Figure 66 for a 2 Hz filter frequency and phase velocity of 1000 m/sec. In this case we again see that motion 10 seconds after the shot detonation are more than one-third as large as the peak motion.

Although some difficulty was encountered in trying to resolve late-arriving signals because of the relatively broad array response and the numerous phases which appear to be arriving, some commentary on the nature of these late arrivals and their propagation paths does seem warranted. First, particle motion diagrams prepared for the time windows associated with several of the prominent, late-time phases in Figure 66 indicate elliptical particle motion in the R-Z plane. Thus, we can conclude that many of these late arrivals are probably associated with Rayleigh waves. Secondly, the relatively late time of these phases (~10 seconds) and their associated propagation velocities (near 1000 m/sec) indicate a propagation path length which could be as great as 10,000 m. This is much greater than the dimensions of the valley itself and indicates either reflection from boundaries outside the valley structure or, more likely, multiple reflections within the valley structure. Assuming multiple reflections are responsible for the motion, reflections at

as many as 10 boundaries (or more) may be needed to produce the long path length. This would imply an extremely efficient propagation path with highly reflective boundaries. Furthermore, if multiple reflections within the valley structure are producing the late time (~10 seconds) arrival, many of the earlier phases adding to the complexity of the beamed records in Figure 66 are probably associated with shorter segments of the long multiple reflection path. The nearly constant amplitude level associated with these phases (after the first few seconds of record) is also indicative of propagation with little loss of seismic energy.

Another interesting feature of the ground motion duration, which is not completely understood at this time, is that the amplitude level at late time relative to the amplitude of the direct Rayleigh wave motion is greater for the single burst MBII-1 event than for the multiple explosion, MBII-2. This can be seen most clearly by comparing the 2 Hz filtered, beam-steered data for the two events (i.e., compare Figure 66 with Figures 73 and 74). For the MBII-1 explosion the late time (~10-12 seconds in Figure 66) amplitude level is about one-third as large as the amplitude level of the direct Rayleigh wave motion. In contrast, for the MBII-2 explosions the amplitude levels at times after about the first 5-6 seconds of record in Figures 73 and 74 are only about one-eighth the amplitude of the direct Rayleigh wave motion. In fact, the filtered, beam-steered traces from the MBII-2 explosions generally appear less complex than those for the MBII-1 explosion. This is really quite surprising considering that the multiple explosion would intuitively seem to be a more complex source. For whatever reason, the multiple source (MBII-2) has apparently not excited the highly efficient wave guide to the same degree as the single source (MBII-1). The most obvious cause for such differences would appear to be the difference in the locations of the

events with respect to the complex geologic structure of the valley.

Finally, one other observation described above could have significant bearing on the problem of ground motion duration in an MX valley. For the station near the valley edge, we noted excitation of fairly large amplitudes prior to the arrival of the direct Rayleigh wave (c.f., Figures 75 and 76). The source of these motions appears to be at the valley boundary and may result from conversion of body-wave to surface-wave energy, or similar phenomena, occurring there. The implications of this observation with regard to sites near valley boundaries appears to be that the generation of such motion may prolong the duration of significant levels of surface motion through the body-wave time window and into the time where the direct surface waves and subsequent arrivals begin to dominate the motion. The conversion of seismic wave energy at such boundaries, which appears to be the source of the motion, may also have implications with regard to the reciprocal problem of ground motion in the valley due to sources acting in close proximity to its boundaries. Such conversions might be expected to enhance the surface wave ground motions.

#### IV. SUMMARY AND CONCLUSIONS

##### 4.1 SUMMARY

The investigations summarized in this report have centered on an attempt to develop an improved, quantitative understanding of the late-time, low-frequency ground motion environment for the MX system. This effort has encompassed studies of site and yield scaling laws applicable to this component of the ground motion as well as an assessment of the possibility that the ground motion environment may be significantly modified as a result of siting the system in one or a series of valleys.

A detailed, theoretical analysis of the characteristics of Rayleigh waves produced by near-surface explosions was presented in Section II, where scaling laws were derived which describe the dependence of the airblast-induced, Rayleigh wave motion on both the yield of the explosion and the site geology. These concepts were then applied to an evaluation of the low-frequency ground motion response characteristics of five specific prototype MX sites and were shown to be in good agreement with the available finite difference calculations. In particular, the scaling laws were used to infer that the predominant Rayleigh wave frequencies at these sites will depend only on the thickness and average shear wave velocity of the surficial soil layer and will be independent of yield for yields greater than a few hundred kilotonnes.

A preliminary analysis of the Misers Bluff II-2 "800 millisecond anomaly" was presented in Section 2.5 where it was noted that both the spatial dependence of the anomaly as well as the inferred axisymmetric nature of its source are inconsistent with linear superposition, suggesting that the

observations may correspond to a true multiburst effect. Furthermore, it was shown that these observations can be matched remarkably well by a theoretical model which considers Rayleigh waves converging on the center of the source array from an axisymmetric, impulsive surface source acting at a radius coincident with that of the charge locations.

The current status of the investigation into the valley reverberation problem was summarized in Section III. This summary included a brief overview of previous experimental and theoretical studies as well as a detailed description of the results of the analysis of the Misers Bluff II data. These latter data were processed using a variety of frequency and direction-sensitive filters in an attempt to isolate the source locations for the observed late-time reverberation arrivals. Although some specific arrivals were identified as a result of this analysis, the interpretation of the data was complicated due to the limited resolving power of the seismic arrays and the complexity of the valley structure. However, the Misers Bluff II data were found to be consistent with other data and calculations in that they indicate that the late-time, low-frequency ground motion environment is modified by the presence of the valley boundaries.

#### 4.2 CONCLUSIONS

The analyses summarized above support the following conclusions concerning the characteristics of the low-frequency ground motions produced by near-surface explosions.

1. The seismic source function for airblast-induced Rayleigh waves approaches a constant value at low frequencies (i.e., the total impulse) and decreases as frequency squared (i.e.,  $\sim \omega^{-2}$ ) in the high-frequency limit.

2. At low frequencies the amplitude of the Rayleigh wave source function is directly proportional to yield ( $W$ ) and independent of the site geology. At high frequencies the spectral amplitude level is proportional to  $W^{\frac{1}{3}}$  and increases as the near-surface shear wave velocity increases.
3. For the prototype MX sites considered here, the characteristic corner frequency of the Rayleigh wave site response function,  $f_c$ , is given approximately by

$$f_c \approx \frac{\bar{S}}{2\bar{H}}$$

where  $\bar{H}$  is the total soil thickness at the site and  $\bar{S}$  is the average shear wave velocity of the soil column.

4. For yields greater than a few hundred kilotonnes at the MX prototype sites, the predominant frequency of the fundamental mode Rayleigh wave motion will be equal to  $f_c$ , independent of yield. Moreover, the amplitude of that component of the motion will scale as  $W^{\frac{1}{3}}$ .
5. The "800 millisecond anomaly" observed in the interior of the MBII-2 source array has been identified as a converging Rayleigh wave produced by a nearly axisymmetric load acting on a small surface ring centered on the charge locations. The available evidence suggests that it is a true multiburst effect.

With regard to valley reverberation effects, results of studies conducted to date lead to the following conclusions.

1. The available data confirm that the presence of the valley boundaries can significantly modify the late-time, low-frequency ground motion environment within the valley. In particular, the duration of this component of the motion at in-valley stations has been observed to be anomalously long by factors of two or more with regard to motion measured under comparable conditions outside the valley.
2. The characteristics of the late-time ground motion data recorded from the MBII-1 and MBII-2 experiments were quite different, despite the fact that they were detonated only a few hundred meters apart in the same valley. This indicates that the valley response can be a complex function of the source and receiver location within the valley structure.
3. Although only a few, highly idealized theoretical valley calculations have been performed to date, they have consistently predicted significant boundary effects on the late-time ground motion environment which are in qualitative agreement with the measured data.

## REFERENCES

Auld, H. E. (1978), "Calculations for MX Site #4," Minutes of the Fifteenth Meeting of the Data Analysis Working Group, La Jolla, California.

Auld, H. E. and J. R. Murphy (1979), "Surface Wave Calculations," Paper presented at the Defense Nuclear Agency Strategic Structures Division Biennial Review Conference, Menlo Park, California.

Bache, T. C., J. F. Masso and B. F. Mason (1977), "Theoretical Body and Surface Wave Magnitudes for Twelve Numerically Simulated Cratering Explosions," Systems, Science and Software Report SSS-R-77-3119, January.

Bache, T. C. (1979), Personal Communication.

Brode, H. L. (1968), "Review of Nuclear Weapons Effects," Annual Review of Nuclear Science, 18, pp. 153-202.

Cherry, J. T., S. M. Day, N. Rimer, W. L. Rodi and H. J. Swanger (1978), "Rayleigh Waves in MX Valleys," Report to SAMSO, Work Order 11084.8-009, October.

Data Analysis Working Group (1978), "Minutes of the Fourteenth Meeting of the Data Analysis Working Group," Albuquerque, New Mexico.

Ewing, W. M., F. Press and W. S. Jardetzky (1957), Elastic Waves in Layered Media, McGraw-Hill, New York.

Harkrider, D. C. (1964), "Surface Waves in Multilayered Elastic Media I. Rayleigh and Love Waves from Buried Sources in Multilayered Elastic Half-Space," BSSA, 54, pp. 627-679.

Harkrider, D. G., C. A. Newton and E. A. Flinn (1974), "Theoretical Effect of Yield and Burst Height of Atmospheric Explosions on Rayleigh Wave Amplitudes," Geophysical Journal of Royal Astronomical Society, 36, pp. 191-225.

Haskell, N. A. (1953), "The Dispersion of Surface Waves in Multilayered Media," BSSA, 43, pp. 17-34.

Mooney, H. M. and B. A. Bolt (1966), "Dispersive Characteristics of the First Three Rayleigh Modes for a Single Surface Layer," BSSA, 56, pp. 43-68.

Murphy, J. R. and R. A. Hewlett (1975), "Analysis of Seismic Response in the City of Las Vegas, Nevada: A Preliminary Microzonation," BSSA, 65, pp. 1575-1597.

Murphy, J. R. and L. J. O'Brien (1978), "An Investigation of the Reflection of Short-Period Surface Waves from Valley Boundaries," Paper presented at the Annual Meeting of the Seismological Society of America, April.

Murphy, J. R. (1978), "An Analysis of the Characteristics of Rayleigh Waves Produced by Surface Explosions," Final Technical Report to the Defense Nuclear Agency on Contract DNA 001-77-C-0272.

Murphy, J. R. and T. J. Bennett (1979), "Multipathing of Short-Period Surface Wave Energy in a Valley Structure," Paper presented at the Annual Meeting of the Seismological Society of America, May.

Murphy, J. R. and T. C. Bache (1979), "Converging Rayleigh Waves from Axisymmetric Surface Loads," Paper presented at the Annual Meeting of the Eastern Section of the Seismological Society of America, October.

Orphal, D. L. and H. H. Hancock (1978), "Preliminary Results of a Calculation of the Surface Ground Motion Response of an Elliptical Valley to a Uniform Nuclear Airblast Loading," Presentation to a meeting of the Data Analysis Working Group, April.

Papoulis, A. (1962), The Fourier Integral and Its Applications, McGraw-Hill, New York.

Sandler, I. (1978), "Outrunning Ground Motion Calculations," Minutes of the Fifteenth Meeting of the Data Analysis Working Group, La Jolla, California.

## DISTRIBUTION LIST

### DEPARTMENT OF DEFENSE

Assistant to the Secretary of Defense  
Atomic Energy  
ATTN: Executive Assistant

Defense Advanced Rsch Proj Agency  
ATTN: T10

Defense Intelligence Agency  
ATTN: RDS-3A

Defense Nuclear Agency  
ATTN: SPSS, J. Galloway  
ATTN: SPSS, E. Sevin  
2 cy ATTN: SPSS, G. Ullrich  
4 cy ATTN: TITL

Defense Technical Info Center  
12 cy ATTN: DD

Field Command  
Defense Nuclear Agency  
ATTN: FCTMD  
ATTN: FCPR

Field Command  
Defense Nuclear Agency  
Livermore Division  
ATTN: FCPRL

Joint Strat Tgt Planning Staff  
ATTN: NRI-STINFO Library  
ATTN: XPFS

Undersecretary of Def for Rsch & Engrg  
Department of Defense  
ATTN: Strategic & Space Systems (OS)

### DEPARTMENT OF THE ARMY

BMD Advanced Technology Center  
Department of the Army  
ATTN: ATC-T

BMD Systems Command  
Department of the Army  
ATTN: BMDSC-HW

Chief of Engineers  
Department of the Army  
ATTN: DAEN-ASI-L  
ATTN: DAEN-RDM  
ATTN: DAEN-MPE-T, D. Reynolds  
ATTN: DAEN-RDL

Harry Diamond Labs  
Department of the Army  
ATTN: DELHD-I-TL  
ATTN: DELHD-N-P

U.S. Army Ballistic Research Labs  
ATTN: DRDAR-TSB-S  
ATTN: DRDAR-BLE, J. Keefer

U.S. Army Cold Region Res Engr Lab  
ATTN: Library

### DEPARTMENT OF THE ARMY (Continued)

U.S. Army Construction Engrg Res Lab  
ATTN: Library

U.S. Army Engineer Center  
ATTN: Technical Library

U.S. Army Engr Waterways Exper Station  
ATTN: WESSA, W. Flathau  
ATTN: WESSD, J. Jackson  
ATTN: J. Zelasko  
ATTN: Library

U.S. Army Material & Mechanics Rsch Ctr  
ATTN: Technical Library

U.S. Army Materiel Dev & Readiness Cmd  
ATTN: DRXAM-TL

U.S. Army Nuclear & Chemical Agency  
ATTN: J. Simms  
ATTN: Library

### DEPARTMENT OF THE NAVY

Naval Construction Battalion Center  
ATTN: Code L51, J. Crawford  
ATTN: Code L08A  
ATTN: Code L53, J. Forrest

Naval Facilities Engineering Command  
ATTN: Code 09M22C

Naval Postgraduate School  
ATTN: Code 0142 Library  
ATTN: G. Lindsay

Naval Research Lab  
ATTN: Code 2627

Naval Surface Weapons Center  
ATTN: Code F31  
ATTN: Code X211

Naval Surface Weapons Center  
ATTN: Tech Library & Info Services Br

Office of Naval Research  
ATTN: Code 715

### DEPARTMENT OF THE AIR FORCE

Air Force Institute of Technology  
ATTN: Library

Headquarters  
Air Force Systems Command  
ATTN: DLWM

Assistant Chief of Staff  
Intelligence  
Department of the Air Force  
ATTN: IN

DEPARTMENT OF THE AIR FORCE (Continued)

Air Force Weapons Laboratory  
Air Force Systems Command  
    ATTN: NTE, M. Plamondon  
    ATTN: SUL  
    ATTN: NT, D. Payton  
    ATTN: NTED-I  
    ATTN: NTED-A  
    ATTN: DEY  
    ATTN: NTES-S  
    ATTN: NTES-G  
    ATTN: NTEO  
  
Research, Development & Logistics  
Department of the Air Force  
    ATTN: SAFALR/Dep for Strat & Space Sys

Ballistic Missile Office  
Air Force Systems Command  
    ATTN: MNXH, D. Gage  
    ATTN: MNXN, W. Crabtree

Research, Development & Acq  
Department of the Air Force  
    ATTN: AFRDQI, N. Alexandrow  
    ATTN: AFRDQA  
    ATTN: AFRDQSM  
    ATTN: AFRDPN

Strategic Air Command  
Department of the Air Force  
    ATTN: NRI-STINFO Library  
    ATTN: XPS

VELA Seismology Center  
Department of the Air Force  
    ATTN: G. Ullrich

DEPARTMENT OF ENERGY CONTRACTORS

Lawrence Livermore National Laboratory  
    ATTN: D. Glenn

Los Alamos National Scientific Lab  
    ATTN: C. Keller  
    ATTN: R. Sanford

Sandia National Laboratories  
    ATTN: A. Chabai  
    ATTN: Org 1250, W. Brown

OTHER GOVERNMENT AGENCIES

Central Intelligence Agency  
    ATTN: OSWR/NED

DEPARTMENT OF DEFENSE CONTRACTORS

Acurex Corp  
    ATTN: J. Stockton  
    ATTN: K. Triebes  
    ATTN: C. Wolf

Aerospace Corp  
    ATTN: H. Mirels  
    ATTN: Technical Info Services

Agbabian Associates  
    ATTN: M. Agbabian

DEPARTMENT OF DEFENSE CONTRACTORS (Continued)

Applied Theory, Inc  
    2 cy ATTN: J. Trulio  
  
Artec Associates, Inc  
    ATTN: S. Gill  
  
Boeing Company  
    ATTN: Aerospace Library  
    ATTN: S. Strack  
  
California Research & Technology, Inc  
    ATTN: M. Rosenblatt  
    ATTN: Library

University of Denver  
Space Science Lab  
    ATTN: J. Wisotski

Eric H. Wang  
Civil Engineering Rsch Fac  
University of New Mexico  
    ATTN: P. Oldde  
    ATTN: J. Lamb  
    ATTN: J. Kovarna

General Electric Company—TEMPO  
    ATTN: DASIAC

H-Tech Labs, Inc  
    ATTN: B. Hartenbaum

Higgins, Auld & Associates  
    ATTN: N. Higgins  
    ATTN: H. Auld  
    ATTN: J. Bratton

IIT Research Institute  
    ATTN: Documents Library

J. H. Wiggins Co, Inc  
    ATTN: J. Collins

Kaman AviDyne  
    ATTN: R. Ruetenik

Merritt CASES, Inc  
    ATTN: Library

Mission Research Corp  
    ATTN: G. McCartor  
    ATTN: C. Longmire

Nathan M. Newmark Consult Eng Svcs  
    ATTN: N. Newmark  
    ATTN: W. Hall

Pacific-Sierra Research Corp  
    ATTN: H. Brode

Pacifica Technology  
    ATTN: Tech Library

Physics International Co  
    ATTN: F. Sauer  
    ATTN: Technical Library  
    ATTN: J. Thomsen

DEPARTMENT OF DEFENSE CONTRACTORS (Continued)

R & D Associates

ATTN: Technical Info Center  
ATTN: J. Carpenter  
ATTN: J. Lewis  
ATTN: C. MacDonald  
ATTN: A. Kuhl  
ATTN: R. Port  
ATTN: P. Haas

Science Applications, Inc

ATTN: H. Wilson  
ATTN: Technical Library  
ATTN: R. Schlaug

Science Applications, Inc

ATTN: D. Hove

Science Applications, Inc

ATTN: B. Chambers 111

SRI International

ATTN: G. Abrahamson  
ATTN: D. Johnson  
ATTN: J. Colton  
ATTN: Library

Systems, Science & Software Inc

ATTN: C. Needham

Systems, Science & Software Inc

ATTN: K. Pyatt  
ATTN: J. Barthel  
ATTN: Library

DEPARTMENT OF DEFENSE CONTRACTORS (Continued)

Systems, Science & Software Inc

ATTN: J. Murphy

Systems, Science & Software Inc

ATTN: C. Hastings

Terra Tek, Inc

ATTN: Library  
ATTN: A. Abou-Sayed

TRW Defense & Space Sys Group

ATTN: Technical Info Center  
ATTN: T. Mazzola  
ATTN: N. Lipner

TRW Defense & Space Sys Group

ATTN: G. Hulcher  
ATTN: E. Wong  
ATTN: P. Dai

Weidlinger Assoc, Consulting Engineers

ATTN: I. Sandler

Weidlinger Assoc, Consulting Engineers

ATTN: J. Isenberg